198
2-23-76

Ω∼-2096

MASTER

Some Experimental Considerations Regarding Ion Beam Simulation of Neutron Irradiation for Mechanical Property Measurements

Battelle
Pacific Northwest Laboratories

BNWL-1961

DISCLAIMER

DISCLAIMER

Portions of this document may be illegible in electronic image products. Images are produced from the best available original document.

ERDA-RL RICHLAND, WA

ERRATA TO BNWL-1961

Acknowledgements

Some Experimental Considerations Regarding Ion Beam
Simulation of Neutron Irradiation For Mechanical Property Measurements[*]

D. L. Styris[†], R. H. Jones[†], O. K. Harling[†]
G. L. Kulcinski[††] and R. P. Marshall[†]

[†]Battelle-Northwest Laboratories
Richland, Washington 99352

[††]University of Wisconsin
Madison, Wisconsin 53706

Table of Contents

List of Tables

List of Figures

List of Figures (Cont'd)

I. INTRODUCTION

Little comment is required to convincingly present the urgent need for material property data for the U.S. fusion reactor program. With the present schedule for the Tokamak Fusion Test Reactor (TFTR), the Fusion Engineering Research Facility (FERF), and the first Experimental Power Reactors (EPR's), it is probably too late to generate the pertinent mechanical property data for the TFTR and FERF while time is short to accomplish this task for the EPR. Mechanical property data should be available in time for materials selection for EPR which must be made prior to 1985. Even though the Demonstration Power Reactor (DPR) is a much longer range objective for DCTR, material studies directed specifically towards the DPR needs should begin now. The rationale for this statement is presented in Fig. 1 where it is assumed that materials for some DPR components are not presently available but must await laboratory development and scale-up to commercial availability. This cycle frequently requires ten years or more. The significance of this time lag is that the initial material development work for the DPR must be done with either the available fission and fusion neutron sources, and ion simulation because the FERF may not be available early enough to allow the full development cycle before major DPR decisions must be made.

Accelerators, which are useful for simulating bulk irradiation by fast neutrons, must be able to provide beams of ions which can produce damage rates equal to and in excess of the damage rates expected from neutron fields in CTR's. The ion ranges in the test samples must be considerably larger than the minimum thicknesses of these samples. This is necessary to avoid chemical contamination of the samples by the ions and to reduce the variations in damage rate across the sample. Other important considerations are cost per unit of data and the time requirements to obtain useful results. The expectation that ion simulation can provide results more rapidly than

1

is possible with neutrons, with better control of most experimental parameters, and at lower cost than with neutrons, is the major justification for such simulation.

Ion beam simulation of neutron damage for mechanical properties is a relatively new and undeveloped research area with the clear exception of void swelling studies. The following report contains reviews of U.S. CTR mechanical property needs and ion simulation for mechanical properties and detailed discussions of key experimental questions.

II. Preliminary Assessment of the Requirements for Mechanical Property Data Related to CTR Materials

A. Introduction

Any attempt to predict what materials property data will be needed for future CTRs is, at best, like trying to forecast what offense to use for the 1987 Superbowl. Both predictions obviously depend on what teams (reactor concepts) will be sent to the game, what the rules of the game will be at that time (i.e. what will society be willing to accept for environmentally compatible energy production) and what new stars (new alloys) will be developed between now and that time. Once all of these decisions are made, one is faced with defining the weather (irradiation and thermal environment) on the day of the game and making a judgement about how the team might operate in those conditions. This latter decision would require a large amount of experience (data bank) under similar conditions and if those conditions have not been tested, some rigorous, intense training (simulation) to see how the team might play in the rain, snow, sunshine, artificial turf, etc.

Turning specifically to the question of mechanical property requirements for CTRs we might approach the problem by asking ourselves the following four questions.

1) What is the time frame in which we need the data?

Are we interested in materials for near term break-even devices, the first experimental reactors, the materials test reactors or commercial systems? Obviously, the urgency relaxes as we extend our time requirements but the form of the reactor also becomes more uncertain as well.

2) What type of reactor concept should we consider?

Aside from the obvious divisions of tokamak, mirror, magnetically pulsed device, laser or electron beam system, we must also address the question of whether the reactor will be a driven system (like TCT), a fusion-fission hybrid, a fission product burner or a "conventional" device. Each of the reactors have problems common to all devices

3

but they also have some problems which are very specific to a given concept, i.e. fatigue problems in laser systems, insulator problems for theta pinches, etc.

3) What are the environments in which we will expect materials to operate?

What will be the charged particle, photon and neutron fluxes and fluence? What type of coolant (which will largely determine the operating temperature and pressure) will be used and will there be chemical as well as physical problems to contend with during a components lifetime? We must also be prepared to examine the effect a switch to a D-D cycle might have on neutron flux and fluence values. Finally, will the reactor operation be typically steady state or will there be a large number of temperature and/or pressure excursions to contend with over a long period of time?

4) What materials do we expect to use in a given type of reactor and how long do we expect they must last?

One possible scenario is that society will place a large premium on reduction of thermal pollution thereby dictating the use of high temperature refractory metals and alloys such as Mo, Nb, V or even graphite. Perhaps the emphasis will be on minimum long term activation materials such as Al or V in contrast to Nb or stainless steels. There may be an adversion to liquid metals (because of fire hazard) and "safer" coolants such as helium or H_2O (steam) would be preferred. The latter choice might allow Zr alloys to be used. If there is a trend toward lower tritium inventories in the blanket, we must then ask if we will be allowed to use large amounts of Be which is relatively scarce and expensive. Finally, will there be any special problems with the use of fissionable materials in the blankets?

The above list of questions is indeed formidable and in the limited scope of this report I will only be able to present a summary of what is being proposed now (June 1975). Later, more detailed reports can expand on these ideas, examine new forms of reactors, and explore how one might test materials under conditions truely characteristic of fusion reactors.

The last caveat that must be made is that this report will only address the mechanical properties of the <u>metallic</u> materials in the reactor blanket, and in particular, the first wall. It is certainly recognized that there will be large stresses and strains in magnet structures and even in CTR shields, but these tend to be more "conventional" in that the irradiation plays a minimal role.

Let us now consider each one of the above questions in more detail.

B. <u>Time Frame for Data Requirements</u>

There appears to be at least five different levels of reactor (or device) developments which must be transcended before one would get to a "standard" commerical reactor. These phases are listed below along with the expected dates of operation.

(1975-1982) 1) Near Term Fusion Neutron Source Devices - The object of these devices will be to subject materials to moderate ($\sim 10^{20}$n cm^{-2}yr^{-1}) 14 MeV neutron fluences and to study the difference in damage mechanisms of 14 MeV and fission neutrons. The neutron sources fall into 3 general categories: solid targets [rotating target D-T systems or Be(D,n) B sources][1,2], liquid targets [Li(D,n)Be][3] and gas targets.[4]

(1980-1982) 2) D-T Fusion Feasibility Devices - The purpose of these machines would be to demonstrate some type of positive power balance while burning D&T. This does not necessarily mean that the ignition Lawson criteria will be exceeded. Such machines could be driven machines (i.e. large amounts of power injected to keep the plasma temperature high) in the case of tokamaks.[5-6] There may also be such devices for laser and electron beam inertial confinement schemes, mirror systems or pulsed concepts.

(~1985) 3) Fusion Engineering Research Facility (FERF) - This will be the first type of fusion device specifically aimed at high fluence irradiation studies of potential CTR materials. Such reactors may be in the few hundred megawatt thermal systems but there will probably be no attempt to use this power to make electricity (hence, it will involve low temperature heat) or to breed tritium. The maximum

14 MeV neutron flux will be $\le 10^{14}$ n/cm^2/sec and there will be modest
thermal and mechanical stress requirements. In the past, the mirror
concept[7] appeared to be the best approach for such a facility but
the theta pinch[8] could also contribute here. However, a recent
proposal for a tokamak materials testing facility[9] has great merit.

(1985-1990)   4) Experimental Power Reactor (EPR) Stage - This will be the
first series of reactors where attempts may be made to produce
electricity (as a demonstration of principle, not a commercial venture)
and to breed tritium. Such reactors will encounter some of the problems
of commerical systems (high fluences, temperatures, etc.) but the re-
actor would probably not be incorporated into an electrical grid. This
means that plant factors can be somewhat relaxed (perhaps as low as
10%) and more frequent shutdown and replacement would be allowed.
Power levels are anticipated to be in the 50-200 MWe region.[10-12]

(1990-2000)   5) Demonstration Power Reactor (DPR) Stage - It is at this
stage that fusion reactors will be expected to produce high grade
(high temperature) thermal energy for production of a several hun-
dred MWe.[14-32] There will be attempts to incorporate such reactors
into existing grids so that high plant factors may be required (~70%)
and a premium will be placed on long lived reliable components. Such
reactors will not produce electricity economically but must demonstrate
the capability to do so with all the necessary fusion systems operating
simultaneously (S/C magnets, T_2 systems, injectors, materials, coupled
power systems, lasers, energy storage, environmental factors, etc.)
This is the type of reactor described by most of the conceptual de-
sign efforts in the past few years (i.e. UWMAK series, PPPL, ANL-LASL,
ORNL designs).

(>2000)   6) Commercial Power Reactor (CPR) Stage - It is at this point
that all systems must have demonstrated sufficient reliability such
that utilities will, of their own choice, choose a fusion reactor over
a comparable sized fission or fossil fuel system. Extremely high re-
liability (i.e. plant factor of approximately 80%) will be required
of all components and materials performance will be largely governed
by strict codes which will have been developed in the DPR stage for

the materials of interest. There is currently no work in this area simply because one must be well into the DPR stage before it is apparent what materials and reactor concepts will survive to the CPR stage.

For mechanical properties work there is no strong interest in time regimes 2 and 6. The first is relatively uninteresting because of the low temperature and fluence operation and the low cost penalty involved with frequent changing of the irradiated components. The last is of interest, but there is no way such a regime could be treated at this time.

We are then left with the mechanical property requirements for the FERF, EPR and DPR regimes and how the near term fusion neutron sources can be used to understand the materials behavior at least in the EPR and FERF stage.

C. What Type of Reactor Concept Should be Considered?

Such a question can only be answered with considerable speculation at this time but we can develop a scenario on the basis of our present information.

It appears that the leading contenders for the FERF series are the D-T mirror[7] or tokamak [9] reactors either driven or in an ignited state. There appears to be no reason to use any fission-fusion system for such a reactor. The theta pinch reactor could also function as a FERF to test materials in a pulsed neutron and thermal environment but many physics and technology questions still need to be answered.[8] No proposals for inertial confinement FERF's have been made public.

It is reasonable to expect that the first EPR will be of the type which first successfully passes the feasibility stage. At this time, that means the tokamak. Mirror machines may also be considered in this stage if fission-fusion blankets are allowed. There are presently at least three groups working on the tokamak-EPR, ORNL, G.A., and Argonne National Laboratory.[10-12] LASL has had thoughts about a theta pinch EPR. No known proposals for laser EPR's have been forthcoming.

7

Finally, all of the four reactor types have been considered for the DPR stage. There have been at least 8 laboratories engaged in Tokamak designs, one in mirrors, 2 in the theta pinch and four in laser concepts. These are listed below in Table I. There have been a wide variety of materials, coolants, temperatures and irradiation conditions proposed for DPRs and a large number of materials analysis studies have been made.[13-34] The DPR is also the system that most people think about when they want to start work in the fusion technology field.

D. What are the Anticipated Operating Conditions for CTR Materials?

An attempt has been made in this section to gather together as much of the information available today concerning the anticipated environment for CTRs. This information is summarized in Table II with respect to concept, first wall flux and accumulated fluence (yr^{-1}), major construction material, coolant, operating temperature, coolant pressure, stress (when available) number of cycles per year and special comments pertaining to that system.

Unfortunately, the EPR designs are too preliminary at this time to make any firm estimates of the operation conditions. Current designs envision steel walls operating up to ~600°C at 0.1-0.2 MW/m² and 50% plant factor. These systems should be better developed in the next year and Table II can be updated.

Since the primary purpose of the FERF's are to test materials under high neutron fluences and not to produce power, the reactor coolant (and hence the blanket walls) can be operated at low pressures. The actual materials testing can be done in closed loops which provide the appropriate temperature and environment. Presumably, these loops will be designed such that they can be easily replaced and therefore they need not last the full lifetime of the plant (they will have to last for at least some minimum time such as approximately 6 months or the downtime required for replacement will seriously reduce the plant factor). The potential low temperature operation of the firsr walls of the FERF should be highlighted because, in general, materials

TABLE I

Summary of Laboratories Which Have Presented Complete

or Semi-Complete, Demonstration Power Reactor Designs

Reactor Type	Laboratory	Reference
Tokamak	ORNL	13
	Univ. of Wisc.	14-16
	PPPL	17
	Culham	18, 19
	Tokai	20, 21
	BNL	22, 23
	Ispra (Euratom)	24
	Khurchatov	25
Laser	LASL	26, 27
	LLL	28
	Jülich	29
	ORNL	30
Mirror-Regular -Hybrid	LLL LLL-BNW	31 32
Theta Pinch	LASL-ANL	33
E-Beam	Sandia	34

TABLE II

Summary of Materials Environments for Various D-T Fusion Devices

Type	Responsible Laboratory	Power MWt	First Wall Material	Flux $n/cm^2 \times 10^{13}$(a)	Fluence/yr $n/cm^2 \times 10^{20}$(b)	Max. First Wall Temp.°C	Coolant	Coolant Pressure Psi	First Wall Stress Psi	Cycles Per Year	Ref.
D-T Neutron Source											
Solid Target	LLL-existing	0.003	--	0.2	0.5	~30	H2O	NS	NS	NS	1
	LLL-projected	<0.06	--	1.0	2.5	~30	H2O	NS	NS	NS	2
	ORNL,UW,UCD	<0.001	--	~0.5(c)	~1.2	~30	H2O	NS	NS	NS	3,35
	Be(D,n)-existing										
	BNL Li(D,n)- projected	3.5	NS	~100(c)	~240	NS	NS	NS	NS	NS	3
Gas Target	LASL	0.3	NS	20	50	NS	NS	NS	NS	NS	4,3
Breakeven	PPPL-Westinghouse	~8	316SS	0.5	0.000015(d)	~30	H2O	90	NS	~1000	5
	ORNL	4.5	304SS	0.6	0.000018(d)	NS	NS	NS	NS	~100	6
FERF											
Mirror	LLL	3.4	NS	6.0	9.5(e)	<100	H2O	280	NS	<50	7
Pinch	LASL	195	SAP	5	7.9(e)	NS	H2O	NS	NS	2x10⁷	8
Tokamak	Wisconsin	355	SS	4.4	7.2(e)	<200	(H2O)	NS	NS	1.6x10⁵	9
EPR											
Tokamak	ORNL	100	SS	~0.44	~1	NS	He	NS	NS	NS	10
	GA	600(~180 MWe)	SS	NS	NS	600	He	NS	NS	~3x10⁵	11
	ANL		(ceramic)	NS	NS	1200	radiation	--	NS	~3x10⁵	12
			SS	0.88	1.4	600	He	NS	NS		
DPR											
Tokamak	ORNL	1000	Nb-1Zr	2.0	4.9	1050	Li	NS	NS	1.3x10⁵	13
	UW-UWMAK-I	5000	316SS	5.5	13.9	500	Li	400	13,000	4.7x10³	14
	UWMAK-II	5000	316SS	5.3	13.4	550	He	735	NS	4.7x10³	15
	UWMAK-III	5000	TZM	~11	28	1000	Li	NS	NS	4.7x10³	16
	PPPL	5546	PE16	7.8	19.8	663	He	735	10,800	4.1x10³	17
	Culham-I	5000	Nb	12.8	32.6	470	He	425	15,000	NS	18
	JAERI-I	2000	Incoloy 800	8.9	22.5	630	He	295	17,000	4.2x10³	19
	-II	2000	Mo Alloy	7	17.8	400-700	He	NS	NS	4.2x10³	20
	BNL-I	3125	SAP	4.4	11.2	400	He	295	2,000	NS	21
	Euratom	170	316SS	0.42	1.1	400	He	425	21,300		22,23
	Kurchatov	NS	Mo(?)	NS	NS	NS	Li	NS	NS	~10⁵	24
Laser	LASL-I	3745	Nb	6.8x10⁶-3.1 Ave.	25.6	NS	Li	NS	NS	2.1x10⁷	25
	-II										26
	LLL	28	Nb	4.4x10⁶-4.4 Ave.	11.2	500-1100	Li	NS	>3700	2.5x10⁸	27
	Julich-Saturn	5000	Nb	11.1	28	850 max	Ne	275	NS	2.5x10⁹	28
	ORNL-Blascon	150	Cr Mo-steel	Very low	Very low	482	Li	NS		2.5x10⁶	29
Mirror	LLL	640	Stainless Steel	7.1	18.3	~650	Li	NS	NS	<10	30
	BNW-LLL	2075	Graphite Steel	NS	NS	NS	NS	NS	NS	<10	31
Pulsed	LASL-ANL	2000	Nb	1100 Inst. -8.9 Ave.	22.6	550-850	Li	30	14,000	8.5x10⁶	32

(a) Instantaneous 14 MeV Neutron Flux
(b) Assuming an 80% plant factor, 14 MeV
(c) Spectrum of Energies, ave. 15 MeV
(d) For proposed 1000 shots
NS = Not Stated
(e) for 50% plant factor

properties are degraded with increasing temperature at constant
neutron fluences. The materials choices for the reactor blankets
appear to be limited to perhaps three classes of alloys which are
readily obtainable in fabricated form and acceptable to strict de-
sign codes, inexpensive and compatible with water (or perhaps gaseous)
coolants. These materials are most likely to satisfy the above re-
quirements:

    stainless steels
    aluminum alloys
    zirconium alloys

Compared to the previous devices, the DPR design studies cover
a wide range of power levels (30-12,000 MW_t), materials (Nb, NblZr,
TZM, Mo, 316 stainless steel, Incoloy-800, SAP and graphite), high
14 MeV neutron fluxes ($0.42-12.8 \times 10^{13}$ n/cm^2/sec time averaged and
0.42×10^{13} to 6.8×10^{19} n/cm^2/sec instantaneous), high 14 MeV
neutron fluences (1.1 to 32.6×10^{20} n/cm^2/yr), higher operating tem-
perature (400-1100°C), more diverse coolants (He, Na, Li), higher
coolant pressures (275 to 735 psi), substantial first wall stresses
(2000 to 21,330 psi) and a wide variation in the number of stress
or strain cycles experienced per year (<10 to 2.5×10^9). Such
widely varying parameters are difficult to categorize in this way
so let us examine the mechanical property data in a little different
manner.

E. Who are the Specific Sources of Stresses and Strains in CTR
   Environments?

It is convenient at this point to divide these sources into
four categories.

    1) Steady state sources arising from thermal sources such as
plasma radiation to first walls, temperature gradients in blankets
and shields, differential thermal expansion of dissimilar materials,
etc.

    2) Steady state sources arising from mechanical sources such
as pressure differentials around the plasma chambers, coolant pressures,
component mass, magnetic field pressure, differential void swelling, etc.

    3) Time dependent sources arising from thermal sources such as
start up and shutdown, pulsed plasma radiation and neutron fluxes, etc.

11

4) Time dependent sources arising from mechanical sources such as pulsed magnetic fields, magnetic field-liquid metal "water hammer" effects, blast wave effects from inertial confinement schemes, etc.

These effects have been summarized in Table III and indications have been given as to which reactor system is most susceptible to them and what particular property is most critical. Most all of these sources are present in one form or another in all D-T fusion devices, and it is oversimplification to isolate one or two mechanical properties that are most effected but for the purposes of this assessment, we will have to make such assumptions.

It is evident from Table III that since mirrors are essentially steady state devices, long term creep-rupture properties are most important. It might also be concluded that the same analogy holds for tokamaks, but the relatively short burn time (several 100 to several thousand seconds) means that there will be many cycles per year (up to 10^4). The blanket will suffer either a drop in temperature at constant coolant pressure (flow rate) or a drop in pressure (flow rate) at constant temperature. It is felt that in either case fatigue will be a major problem and therefore it is felt that low cycle fatigue will be the most critical mechanical property in tokamaks.

F. What are the Magnitudes of the Stresses on CTR Materials?

The next step in this assessment is to tabulate the existing data on the various components of stress on CTR materials. Table IV is an outline of how such a table could be formulated for the first wall only, and examples are given, for the UWMAK-I, II and Princeton Designs. In order to complete this table, it would be necessary to review, in detail, all of the systems studies of Table III. Such a study would be worthwhile, but time consuming. It is also possible that other headings may have to be added to Table IV in order to incorporate special situations.

TABLE III

Summary of Thermal and Mechanical Stresses in CTR Systems

Thermal | | | | | | **Mechanical** | | | | |

Source of Stress	T	M	L	P	Principle Mech. Prop. Affected During Irradiation	Source of Stress	T	M	L	P	Principle Mech. Property During Irradiation
Plasma Radiation	X	X			Creep-rupture life yield Strength	Vacuum Retention	X	X		X	Yield Strength
Thermal Gradient in Blanket	X	X	X	X	Creep-rupture life yield Strength	Coolant Pressure	X	X	X	X	Yield Strength, Creep-rupture life
						Component Weight	X	X	X	X	Yield Strength, Creep-rupture life
Differential Thermal Expansion amoung Dissimilar Metals				X	Creep-rupture life, Yield Strength	Differential Void Swelling	X	X	X	X	Ductility
						Magnetic Field Pressure	X	X			Yield Strength
Start up and Shutdown	X				Fatigue,ductility fracture toughness	Magnetic Field Pressure				X	Fatigue, ductility
Plasma and Neutron Radiation			X	X	Fatigue, ductility yield strength	Magnetic Field Liquid Metal Interaction				X	Fatigue, ducitlity Fracture toughness
Differential Thermal Expansion among Dissimilar metals				X	Fatigue, ductility yield strength	Blast wave			X		Fatigue, ducitlity

Right margin labels: Steady State (top section), Time Dependent (lower section)

T = Tokamak   L = Laser
M = mirror   P = Pulsed (Theta Pinch)

Table IV

Magnitude of Mechanical and Thermal Stresses Induced
in the First Walls of Selected CTR Designs

Parameter	Unit	UWMAK-I	UWMAK-II	PPPL
		General		
Material	--	316SS	316SS	PE-16
First Wall Thickness	mm	2.5	10.8	0.8
First Wall Temperature (Max)	°C	500	550	638
		Thermal		
Surface Heat Load	W/cm^2	22.6	3.42	35
Thermal Stress First Wall	psi	8424	960	NS
Thermal Pulse Time [a]	sec	120	30	--
Number of Cycles	yr^{-1}	4100	4100	4310
		Mechanical		
Coolant Pressure	psi	400	735	735
Stress due to Coolant Pressure	psi	4572	7143	NS
Stress due to Vacuum Alone	psi	?	?	?
Stress due to Component Wt.	psi	?	?	?
Stress due to Differential Void Swelling	psi	?	?	?
Stress due to Magnetic Field	psi	?	?	?
Coolant Stress Difference Between Burn Time and Recharge Time	psi	?	?	?

(a) From zero thermal stress to ~90% of equilibrium level.

14

G. General Comments on What Mechanical Properties are Most Critical
for Successful CTR Operation

If pressed to name the most critical mechanical properties
that must be measured for each of the four CTR systems, the fol-
lowing list in Table V might be suggested. Reasonable ductility
is clearly the dominant property required for steady state devices
like the mirror system. Both low strain rate (creep-rupture life)
and higher strain rate (uniform elongation) studies should be per-
formed. The indicated materials may be somewhat controversial,
but the temperature and stress ranges are broad enough to include
most types of reactor operation.

High cycle fatigue life is obviously the most severe problem
in the theta pinch and laser systems, with thermal and low cycle
fatigue most likely to be the dominant problem in Tokamaks. Using
the same materials and temperature as indicated above, cyclic stresses
between -103 and +103 MPa for steel, -28 and +28 MPa for SAP, etc.
should be conducted $\sim 10^7$-10^8 times to understand their behavior for
a year of operation for a theta pinch system and 10^8-10^{10} for a year
in a laser system. The period of the cycle time should approximate
the thermal pulse time in such a reaction, or, ~ 0.1 sec for the theta
pinch and $\sim 10^{-6}$-10^{-3} sec for laser systems.

It is worthwhile to re-emphasize that Tokamaks will face a
serious fatigue problem during the startup and shutdown periods
associated with D-T burn times. The number of cycles could exceed
10,000 in power reactors and 300,000 is probably an upper limit for
EPR's and FERF's. Most systems will probably cool down and heat up
over 10-100 seconds so that the temperature will not drop to ambient
because of the thermal inertia of the system. However, it is worth-
while to see how this large temperature excursion might effect the
fatigue life. The stress values are not very firm at this time and
more work is needed in this area.

Table V

Summary of Critical Mechanical Properties that Must
Be Known for Irradiated Metals

Property	Material	T°C	Approximate Stress Range-Ksi	Comment
Creep-Ductility	Stainless Steel	400-650	10-20	For all reactor concepts, high strain rate (uniform elongation and low strain rate (creep-rupture life)
	SAP	200-400	2-3	
	Mo Alloys	500-1000	10-30	
	V Alloys	500-800	10-20	
Fatigue	Stainless Steel	400-650	+15	Number of cycles should be 10^7-10^8 for theta pinch and 10^8-10^{10} for laser system. Cycle period ~0.1 sec for theta pinch and 10^{-6} to 10^{-3} sec for laser systems.
	SAP	200-400	$\pm$ 4	
	Mo Alloys	500-1000	$\pm$20	
	V Alloys	500-800	$\pm$15	
Fatigue	Stainless Steel	400-650	$\pm$10	For tokamak, number of cycles should be 10,000-150,000. Cycle period 10-100 sec.
	SAP	200-400	$\pm$ 2	
	Mo Alloys	500-1000	$\pm$15	
	V Alloys	500-800	$\pm$10	

16

H. Summary Comments

   Several areas have not been covered in adequate detail in this
limited study. These include:

   1) A complete cataloging of stress calculated by various reactor
design groups. Such a cataloging is presently underway at McDonnell-
Douglas and may be ready by October-November 1975.

   2) A complete listing of the irradiation evnironment (i.e. dpa,
dpa rate, gas production, solid transmutation rates, etc.) has not
been given nor has any discussion been devoted to how this radiation
damage would effect the mechanical properties stated above. This is a
more involved area and one which would require several man months of
effort.

   3) The details of the FERF and EPR systems have not been entirely
accessible. However, recent progress in this area has been rapid and
updating of the information in Table II for these systems could be
done every 3-6 months.

   4) Only metallic materials have been covered, no ceramic materials,
(i.e. Al_2O_3, graphite, SiC)have been considered. The use of carbon in
one form or another has become wide spread in reactor design. For ex-
ample, all three EPR disigns now use some form of carbon on the first
wall. It would be worthwhile to start examining the special mechanical
properties which may be required for these liner materials because
they represent more near term devices.

   5) The question of how to test materials in meaningful irradiation
environments was not addressed. This is the subject of international
conferences in July 1975 at ANL and Gatlinburg, Tcnn. in October 1975.
Careful analysis of the state of the art after those meetings would be
worthwhile.

   An attempt has been made to show where and when mechanical property
data is required for the various devices and reactors proposed by ERDA
and its contractors as well as to list the major studies performed thus
far. The sources of stresses and strains for various reactors have
been enumerated and an outline of the various stress contributions has
been suggested. One cannot go much further without analyzing a reactor
which is actually going to be built. Finally, a preliminary suggestion
of the critical mechanical properties, materials and test parameters

has been made to serve as the basis for future work. This analysis
reveals that low cycle fatigue will be most critical for tokamaks
and high cycle fatigue will be most troublesome for pulsed reactors.
Creep-rupture life at high temperatures plays a dominant role in
mirror machines, and probably a secondary (but important role) in
the pulsed devices including the tokamak reactor.

III. Ion Simulation For Bulk Mechanical Properties: Review

A. U. S. and European Experiments

Ion beam simulation of neutron damage for mechanical properties is a relatively new and undeveloped research area with the clear exception of void swelling studies. We are concerned here with bulk properties such as creep and yield and not exclusively with voids induced in the near surface region. Measurements of these properties implies the use of samples which are thick enough to represent bulk materials and which are thin enough to permit penetration by available accelerator ion beams. The criteria for sample size will be discussed at length elsewhere in this report. However, it is useful to point out at this point that metal samples of thickness greater than about 0.002 cm are expected to provide useful bulk data.

Although ion beam simulation offers possibilities for a wide range of useful experiments, relatively little has been done to date[36-46] to exploit the technique. In situ irradiation induced creep measurements have been made at the Argonne National Laboratory by Harkness, Yagee and Nolfi[39] and at the Massachusetts Institute of Technology by Hendrick, Bement and Harling.[36] Currently ion beam simulation research for bulk mechanical properties is being pursued at various laboratories. In the USA work is in progress at the Pacific Northwest Laboratory of the Battelle Memorial Institute, and that work will be outlined in some detail in another report. Work on in situ irradiation enhanced creep is continuing at the Massachusetts Institute of Technology. A similar effort with more sophisticated instrumentation is now in progress at the Naval Research Laboratories. At AERE-Harwell, Julich, Kernforschungs Zentrum Karlsruhe, Holifield National Laboratory and Hanford Engineering Development Laboratory, in situ creep experiments are being developed. Mechanical property measurements of ion irradiated samples are expected to receive further development at the Kurchatov Institute near Moscow.

B. Comparison of Radiation Sources

The damage effectiveness of a number of available radiation sources is illustrated in Figure 1. As a useful measure of damage effectiveness we have used dpa/particle/cm^2. There is some question that dpa is an adequate basis for comparing the damage from various radiations. Certainly an adequate comparison of the damage from various sources should include the effects of hydrogen and helium production and of transmutations. Helium production varies widely for different neutron sources as expected from consideration of the energy dependence of the (n,α) cross section. The ratio of helium production to dpa is presented in Figure 2. Ion beams can be used to inject appropriate amounts of helium, while displacement damage is simultaneously created by the same beam or by a second bombarding ion beam of a different energy and or species.

Figure 3 combines the damage effectiveness in dpa/particle/cm^2 with the particle fluxes available at various radiation sources. The damage rate in dpa/sec is shown for two US fast reactors, for a fusion reactor with 1Mw/m^2 wall loading, for a (D, T) neutron source of 10^{13}/cm^2-sec and for various current densities of proton and deuteron ion beams. The fast reactors will obviously have a place in the CTR test program, even though reactor irradiations are very expensive and the helium production per dpa is much lower than for the future fusion reactors. In a limited number of cases, where nickel is a major constituent of the test material, it should be possible to approach the correct ratio of helium production to dpa. In such cases a high flux thermal reactor such as HFIR would be used to produce helium by two successive neutron reactions in nickel. The (D, T) source of 10^{13}/cm^2-sec is currently not in existence. The Rotating Target Neutron Source (RTNS) at LLL currently produces a peak flux of about 10^{12}n/cm^2-sec for a sample which would be useful for in situ mechanical property testing. An upgraded RTNS with approximately 10X the presently available flux is proposed and may be available 3-5 years from today. The helium production rate per neutron of a pure (D, T) source will probably exceed that of a fusion reactor. Higher (D, T) neutron fluxes should eventually become available. For example, a supersonic jet nozzle target proposed by LASL is expected to produce
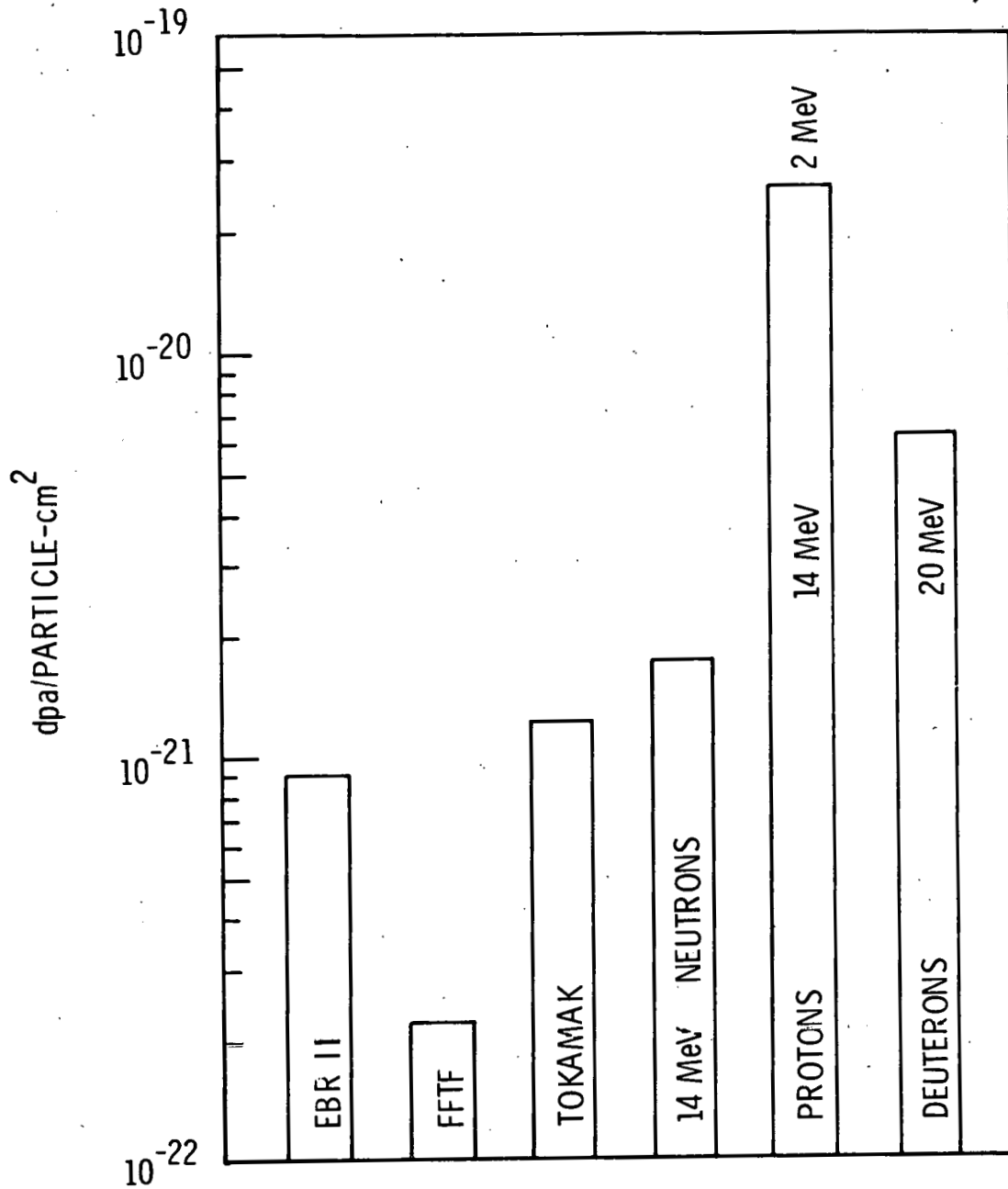
Figure 1. Damage Effectiveness of Some Radiation Sources
Applied to Niobium
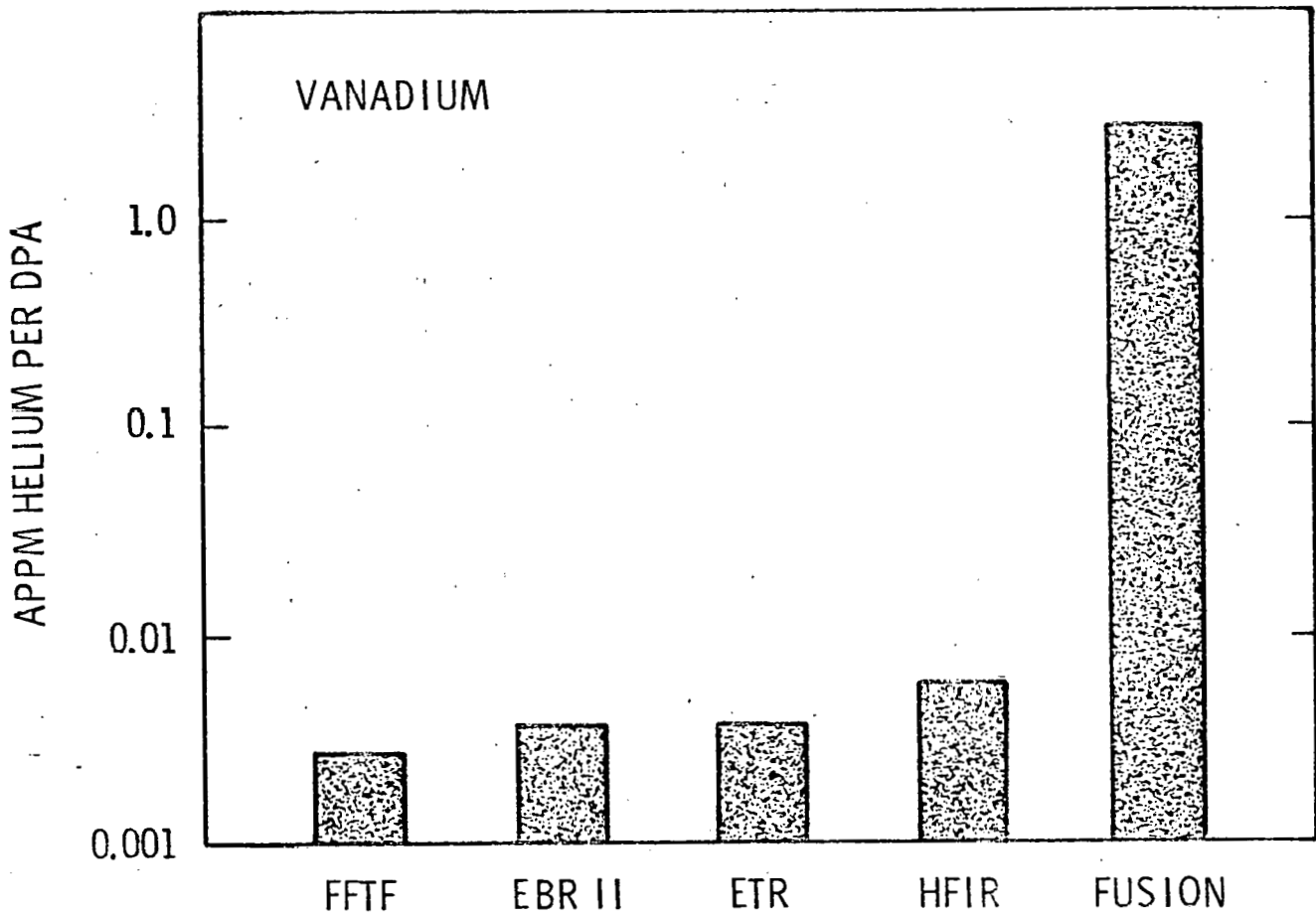
Figure 2. Ratio of the atomic parts per million of helium gas generated per dpa in vanadium for various nuclear facilities.
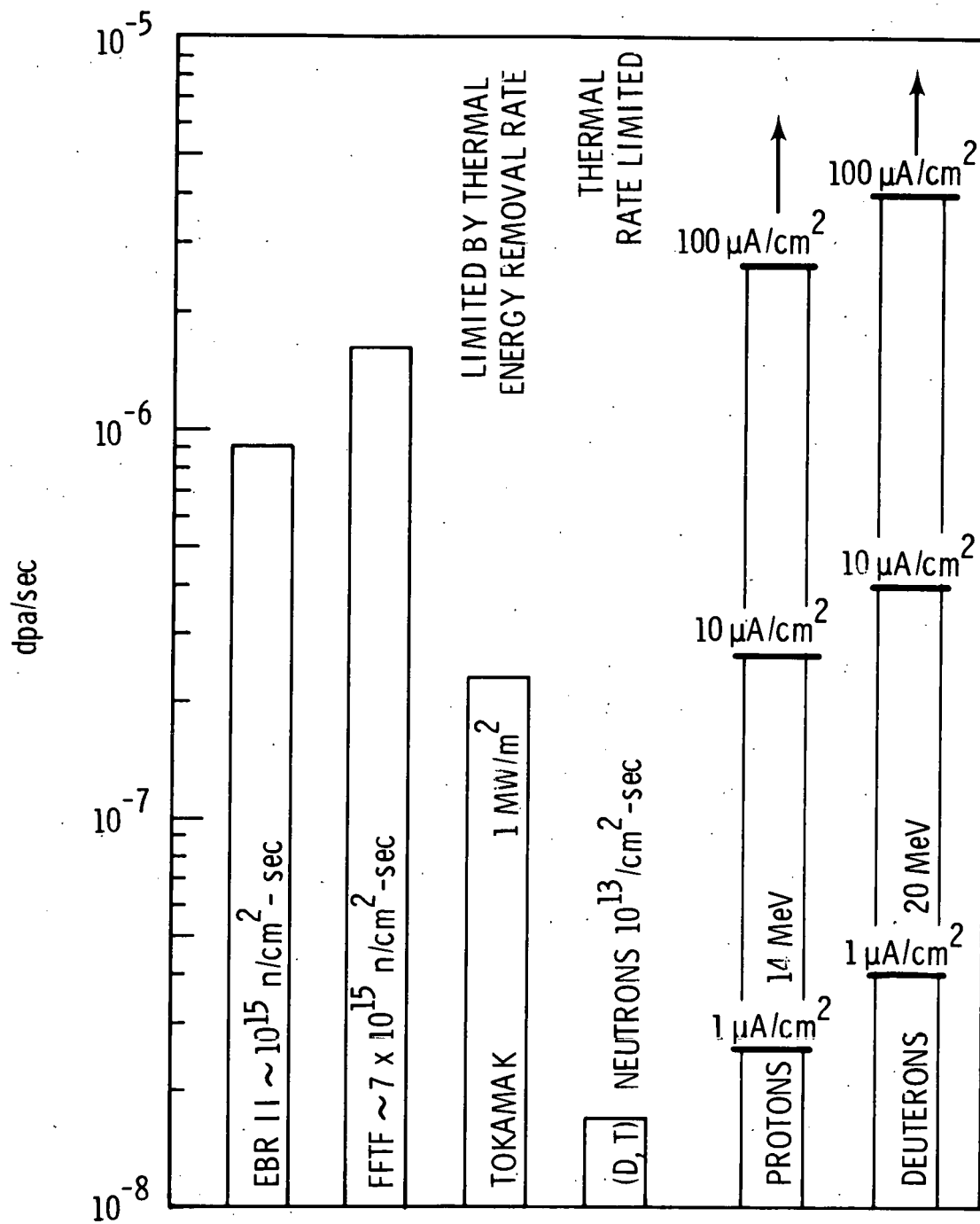
Figure 3. Displacement Rates for Several Particle Sources
Applied to Niobium

fluxes around 10^{14} if the projected 5 year development and con-
struction schedule can be maintained. Another accelerator neutron
source which is of considerable interest to CTR materials tests
is the (D, Be) or (D, Li) source. Currently available (D, Be)
sources produce fluxes up to about 10^{13} n/cm^2-sec in the forward
direction. Upgrading of (D, Be) or (D, Li) sources appears quite
feasible and a proposal[3] exists for a source with a liquid lithium
target which could produce fluxes in the 10^{15} range.

C. Review of Accelerator Sources for Ion Irradiations

Accelerators, which are useful for simulating bulk irradiation
by fast neutrons, must be able to provide beams of ions which can
produce damage rates equal to and in excess of the damage rates
expected from neutron fields in CTR's. The ion ranges in the
test samples must be considerably larger than the minimum thick-
nesses of these samples. This is necessary to avoid chemical con-
tamination of the samples by the ions and to reduce the variations
in damage rate across the sample. Examples of damage profiles for
relevant conditions will be given in another section of this report.
Other important considerations are cost per unit of data and the
time requirements to obtain useful results. The expectation that
ion simulation can provide results more rapidly than is possible
with neutrons, with better control of most experimental parameters,
and at lower cost than with neutrons, is the major justification
for such simulation.

A relatively large number of suitable positive ion accelerators
including cyclotrons, linacs and Van de Graaffs are available in the
USA for neutron simulation in mechanical property measurements. A
good compilation of such facilities is available in reference 48.
Overall the requirements for the ion beams mentioned above can best
be met by use of protons, deuterons or helium ions produced by ex-
isting low energy and medium energy cyclotrons. Accelerators which
would permit self-ion bombardment, of sufficiently large range to
be useful for mechanical properties measurements, could be con-
sidered for simulation work after its utility has been clearly
demonstrated. Such heavy ions would have considerably higher
damage rates than the low mass hydrogen or helium ions. However,

development of such beams would very likely require large new capital investments. Van de Graaffs and linacs are also suitable, but these machines are generally still of major importance for nuclear physics research, while the lower energy cyclotrons capable of producing protons, deuterons and helium ions in the energy range of ~10 - 100 MeV have essentially become obsolete for the research which justified their construction. Suitable ion currents, current densities and particle energies for mass 1, 2 and 4 ions are available from several such accelerators for use in mechanical properties studies. Ion current densities which will produce damage rates in excess of that expected for fusion reactors, see Figs. 1 and 3, are available from these existing accelerators. Initially at least ion simulation experiments will be limited by the ability to remove beam heat from the sample rather than by the capabilities of available accelerators. Control of sample temperatures is particularly critical for in situ irradiation[36] creep measurements.

For Battelle's ion simulation research we expect to make use of the 76-inch isochronous cyclotron at the University of California, Davis and the 60-inch cyclotron at the University of Washington, Seattle. Some use may also be made of the negative and positive ion electrostatic accelerators at PNL. These accelerators could be very useful in developing and testing the irradiation equipment which would be used at the cyclotrons. The electron Van de Graaff at PNL has adequate intensity and energy (2MV) to permit consideration for direct use as simulation source. Table VI shows some of the parameters of the two cyclotrons which are relevant to the present discussion. Both the UCD and UW are convenient to PNL, approximately four hours travel time, and both accelerators have available sufficient beam time to meet the forseeable needs for Battelle's irradiations. A significant additional advantage of using these two cyclotrons, particularly the one at Davis, is the availability of (D, Be) neutron sources. The Davis (D, Be) source is particularly attractive since it produces useful neutron fluxes up to about 10^{13} n/cm^2-sec. This will be discussed further in the next section of this report.

Table VI. Some Characteristics of Accelerators to be Used by Battelle for Ion Simulation Studies.

Accelerator	Proton Energy	Proton Current	Deuteron Energy	Deuteron Current	Helium ion Energy	Helium ion Current	Approx. cost per hr
UCD - 76" Isochronous Cyclotron	7-66MeV	>45μa	15-45MeV	>45μa	30-86MeV	>25μa	$135
UW - 60" Cyclotron	10MeV	>100μa	20MeV	>100μa	42MeV	~50μa	$75

D. Fusion Neutron Facilities

An essential part of Battelle's simulation program will be the use of neutron irradiations to obtain mechanical property data. These measurements are necessary in order to determine the degree of correlation which can be obtained with the use of penetrating ion beams. A great deal of data is already available from the irradiation of fission reactor materials in fast test reactors. Much of this data will be valuable for correlations with the present CTR materials studies, however, additional neutron measurements will be needed. In this section we will briefly review the available neutron facilities which can be used for CTR testing. Details of the neutron data needs will be discussed elsewhere.

Currently there are no neutron sources which have an energy spectrum and intensity comparable to that expected in future CTR's. This, of course, is the major justification for the simulation approach. Accelerator produced neutron sources are available which produce neutrons from the fusion reactions (D, D) and (D,T) and by deuteron striping e.g., (D, Be) and (D, Li). Fast fission reactors such as the FFTF and EBR-II are also of use for CTR testing although the ratio of helium production to dpa is much smaller than for a fusion source, please see Figure 2.

Irradiations with high flux reactors will in all probability be an important part of the Battelle program. High dpa rates are attainable, see Fig. 1 and 3. Gas production, especially helium can be attained in such fission reactor irradiations by use of the tritium trick, helium ion implantation by accelerators or in the case of nickel samples by thermal neutron induced (n,α) reactions. The long irradiations needed to build up adequate fluence and the great difficulty inherent in properly controlled in-reactor mechanical property tests will continue to make this approach a costly and slow one.

Accelerator sources based on the (D, T) or deuteron stripping reactions, currently offer the most promise for CTR testing. However, while these sources will generally produce a useful dpa/He ratio, their intensity is currently much lower than for fusion reactors. End of life fluences are, therefore, impossible to attain and mechanical property data will have to be extrapolated. Other fusion neutron reactions such as (D, D) would produce lower intensities with existing accelerators. The most intense (D, T) source currently available is the rotating target neutron source (RTNS) at LLL. A 400 KeV D^+ ion beam of 20-30 ma produces $\sim$3-5 x 10^{12} (D, T) neutrons per second from a tritiated titanium target. The target is rapidly rotated through the beam and is water cooled to prevent rapid loss of the ^3H from the irradiated zone. At the closest practical point of approach, to the neutron source spot, a flux of $\sim$2 x 10^{12} n/cm^2-sec is obtainable on a metal foil sample about 1 cm in diameter. For in situ mechanical property tests a neutron flux of $\sim$5-10 x 10^{11} is a realistic estimate of the useable flux for a sample with a gauge length of 1 cm. Under these conditions the maximum flux gradient seen by this sample would be $\sim$20%. The RTNS produces (D, T) neutrons with an essentially isotropic spacial dependence and with an energy spread of several hundred KeV. It is unlikely that this energy spread or the variation in mean neutron energy with angle will be of great significance in most CTR bulk property tests. Mean neutron energy in the forward or deuteron direction where most samples are mounted, is 14.8 MeV for the RTNS.

Major upgrading of the RTNS is proposed to increase the
source strength by about a factor of ten while maintaining the
current target life of about 50 hours and the source spot size
of less than 1 cm. Several advanced RTNS type accelerators are
expected to be available in 3-5 years. Multiple accelerators
of this type should greatly expedite the general CTR materials
program. ERDA laboratories such as PNL with heavy committments
to CTR materials testing, would probably be able to accelerate
their materials testing if advanced or upgraded versions of the
RTNS could be placed directly at the individual laboratories.

A more intense (D, T) source than the upgraded RTNS is
planned at LASL. This source will use a gas target for heat
removal and a supersonic shock nozzle to produce a small high
density gas target zone. Source strengths of ~10^{15}n/sec and
useful fluxes of ~10^{14}n/cm^2-sec are expected when this source
becomes available. A development and construction lead time of
~5 years is anticipated once funding is authorized.

An accelerator source which produces fast neutrons in the
range of interest to CTR is the (D, Be) or (D, Li) source. These
sources based on deuteron stripping and with currently available
medium energy or low energy accelerators, are potentially im-
portant for CTR materials tests. The neutron energy spectrum
obtained from deuterium ions on a thick beryllium target is
shown for D$^+$ energies of 16 and 30 MeV in Figs. 4 and 5. The
neutrons are present in a broad distribution from zero energy
to approximately the deuteron energy. The most intensity occurs
at about 0.40 of the deuteron energy. These spectra are cal-
culated for neutrons emitted in the forward or D$^+$ direction. The
intensity distribution of the stripping reactions is highly aniso-
tropic. Most of the neutrons are emitted in the forward direction.
This feature of stripping sources can be used to advantage in CTR
materials tests since the forward direction is also the location
for test samples. The neutron source strength currently available
from such sources is exemplified by the UCD-76 in. and UW-60 inch
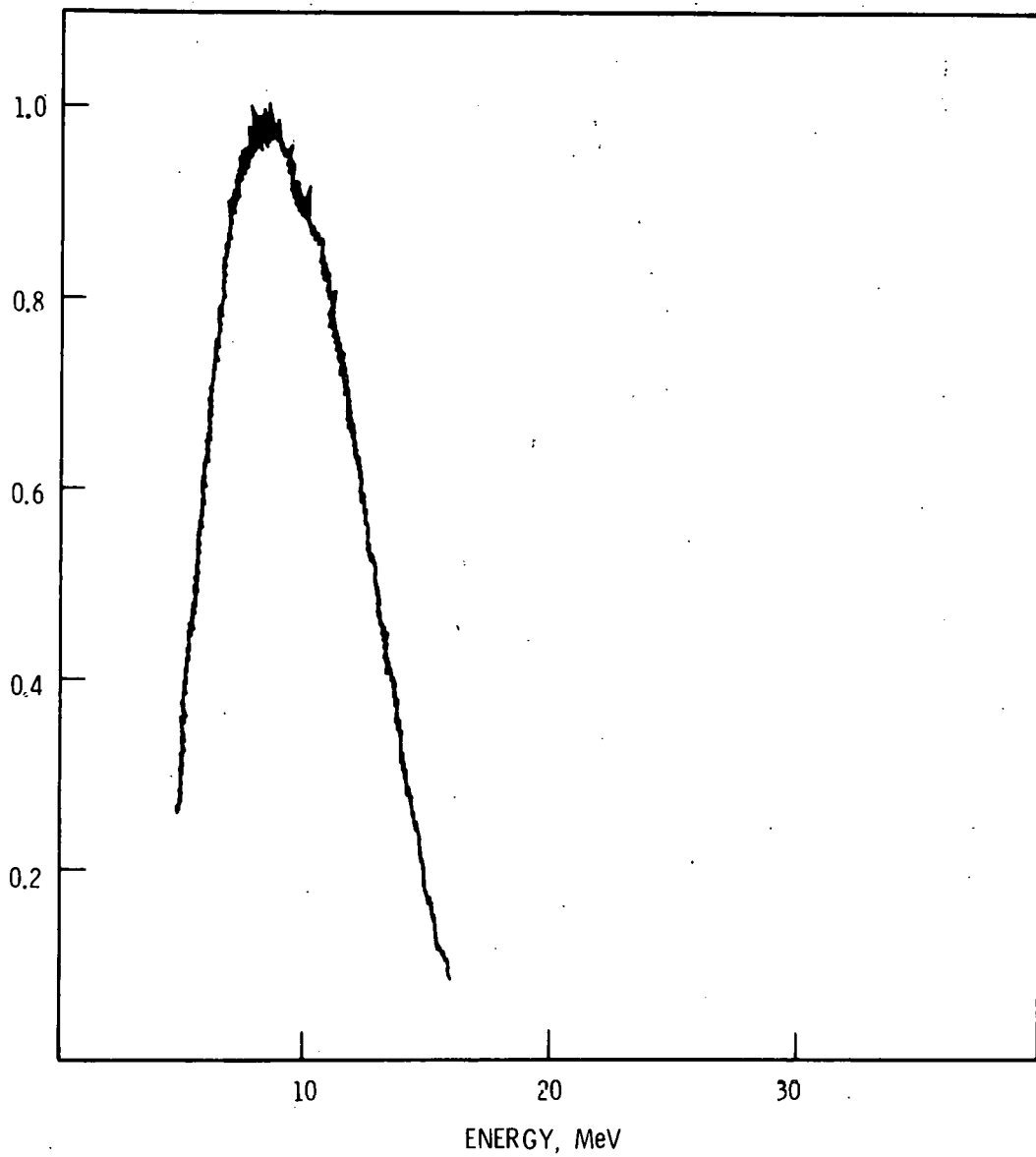
FIGURE 4. (D, Be) Neutron Energy Spectrum 16 MeV D$^+$ on Be
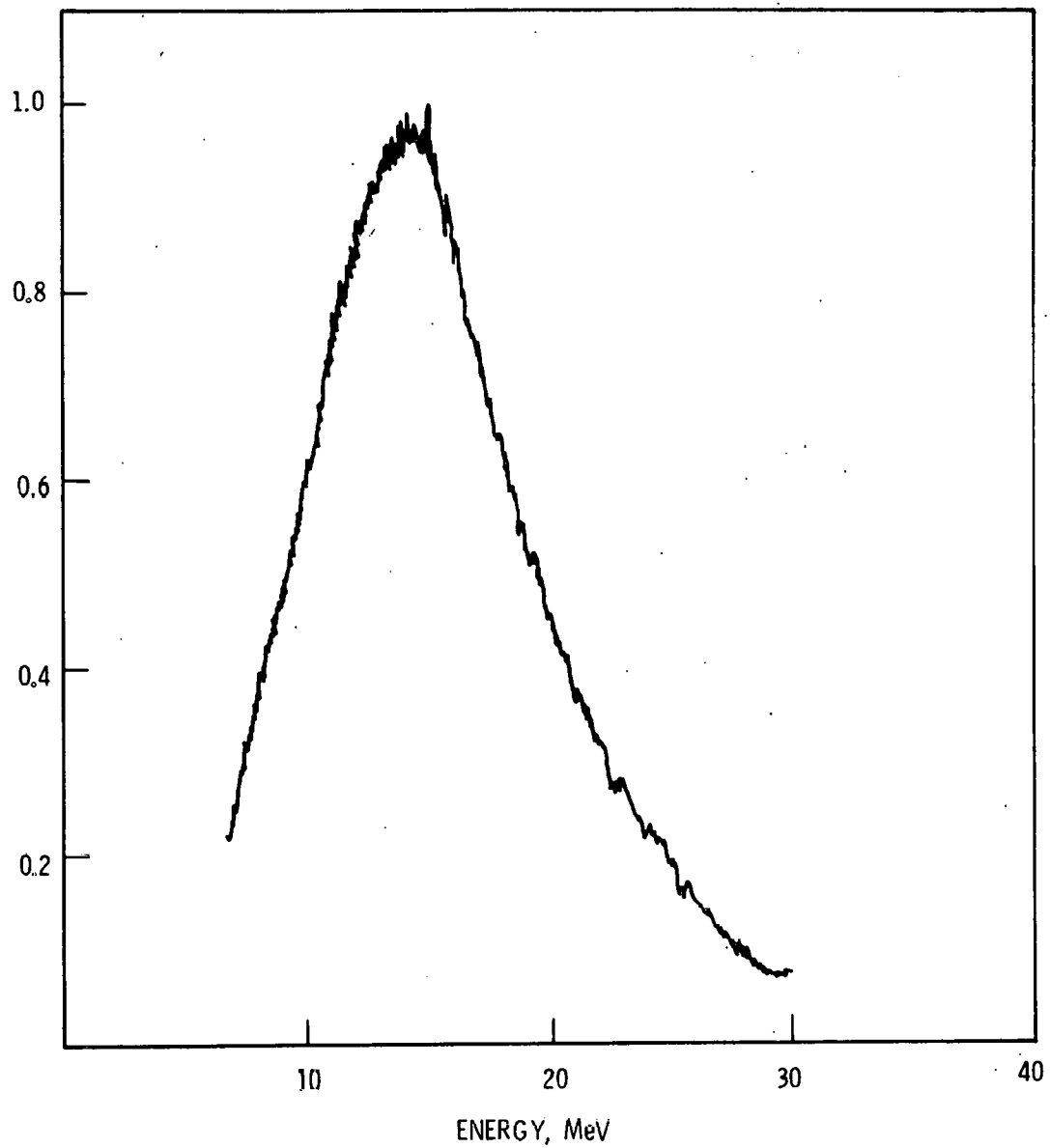
FIGURE 5. (D, Be) Neutron Energy Spectrum 30 MeV D$^+$ on Be

30

cyclotrons which produce about 10^{13} (D, Be) n/sec. Useful fluxes of $\sim 10^{13}$ n/cm^2-sec can be attained on small thin foil samples located in the forward direction near these sources. There are proposals to develop much more intense deuteron stripping sources e.g. a (D, Li) source of 10^{16} n/sec has been proposed.[3] Such a source would have fluxes around 10^{15} n/cm^2-sec. At the present time the available (D, Be) sources will provide a valuable complement to other "CTR" neutron test facilities. Because their intensity is higher than that of current (D, T) sources they may permit some experiments which are not practical with the present RTNS.

Battelle plans to use fast reactors, the LLL, RTNS and the (D, Be) sources at UCD and UW for "CTR" neutron irradiations. None of these sources is ideal for CTR testing but each has significant utility for certain classes of measurements.

IV. Damage Analysis and Calculations For Light Ions

Damage induced in metals exposed to neutron irradiation occurs
when a neutron transfers enough energy to a lattice atom to cause
the atom to be displaced from its lattice site. This displaced
atom is the primary knock-on (PKA) which can (i) "rattle" through
the lattice and stop at an interstitial site or (ii) transfer, by
elastic collisions, sufficient energy to create secondary or higher
order displacements. It should be possible to simulate this type
of damage, i.e. the creation of vacancy-interstitial pairs, using
ions for the bombarding species. With relatively high ion fluxes
the technique might well be used to duplicate large number of dis-
placements per lattice atom (dpa), such as will occur in fusion re-
actor materials.

But neutrons will produce changes in the lattice other than
displacements. Transmutation effects initiated from (n,x) reactions
can also cause various changes in material properties. Phase
stability will be affected in some CTR candidate alloys (Kulcinski,
Loft and Yang[49]) because of significant changes in composition of
the alloy during operation in the fusion environment. This will be
particularly important for Nb-1Zr where Zr might increase to the
point where a second phase begins to appear. Adverse influences
on ductility can be caused by the helium gas from (n,α) reactions.
This can be partially simulated using ions. That is, helium can
be injected to the extent that it matches that quantity produced
by neutrons. It is more difficult to simulate the composition
changes due to variation of metal atom species. Alloy composition
might be varied prior to ion irradiation to match composition of long
term neutron irradiated material. Which of these will be the most
dominant in a given mechanical property test remains to be determined.
Displacements per atom, rate of displacement production, gaseous and
solid transmutation rates, phase instabilities, temperature and strain
rate will all influence mechanical properties of irradiated materials.
Simulating all these effects with ion beam irradiations is not simple;

however, with the exception of solid transmutations, a close approximation to the fusion environment should be possible. It should be pointed out that ion beam irradiations allow one to study these effects independently while also being able to study their combined effects. The effect of chemistry changes resulting from solid transmutations on phase stability in an irradiation environment might be simulated by irradiating a series of alloys of varying composition. Calculated solid transmutation rates would be sufficiently accurate to determine the composition/reactor time relationship.

DPA and Displacement Cross-Section

The displacement cross-section represents the susceptibility of a particular material to displacements by a given bombarding species. Recommended procedures for calculating this cross-section have been described by Doran, Beeler, Dudey and Auss[50] and Keefer[51]. The following gives a brief description of the general procedures. Results are discussed for neutron, proton, deuteron and alpha particle irradiation of Ni and Nb. These results include analyses of dpa profiles, deviations from dpa homogeneity, and dpa rate limits in He gas cooled samples.

Ions

The cross-section $\sigma(E)$ for an ion of energy E is

$$\sigma(E) = \int_{E_d}^{T_m} d\sigma(T) \cdot n_d(T) \tag{1}$$

where $d\sigma(T)$ is the Rutherford scattering x-section for a transfer of energy T, and $n_d(T)$ is a term which accounts for secondary and higher order displacements. E_d is the threshold energy and T_m is the maximum energy which can be transferred.

The term $n_d(T)$ gives the number of displacements due to the collision cascades started by PKA's. From the Robinson[52] formulation of LSS[53] partition energy theory

$$n_d(T) = \frac{\beta T_{dam}}{2E_d}; \quad 2E_d < T \leq T_m$$

$$= 0 \quad ; \quad 0 < T < E_d$$

$$= 1 \quad ; \quad E_d \leq T < 2E_d \tag{2}$$

where T_{dam} is the total elastic energy available for production of displacements and β is somewhat arbitrary, but near unity; Doran et al[51] use 0.8 for Fe. Robinson's[54] treatment of the LSS theory gives

$$T_{dam} = T [1 + \zeta g(\epsilon)]^{-1}$$

where

$$\zeta = 0.1337 \ Z^{2/3}/A^{1/2}$$

$$g(\epsilon) = \epsilon + 0.4024 \ \epsilon^{3/4} + 3.401\epsilon^{1/6}$$

$$\epsilon = T/0.08693Z^{7/3}$$

for a metal of atomic weight A and atomic number Z, and where transfer energy T is in kilovolts.

Numerical integration of equation (1), using protons, deuterons and alphas as bombarding species on Ni and Nb, gives the displacement cross-sections shown in figures 6 and 7. It should be kept in mind that these cross-sections become more uncertain as energy increases. This is due to the increasing influence the uncertainties in T_{dam} and E_d values have on the secondary and higher order displacements. That is to say, the higher the energy of the primary, the greater the energy transfer, and hence the greater the probability of secondary displacement, which is dependent on T_{dam} and E_d.

It is important to note that inelastic scattering cross-sections are not included in these calculations. But Logan[55] has included inelastic collisions to determine PKA spectra for proton irradiation of niobium; a simple comparison can be made to estimate the magnitude of the effect of the inelastic collisions. This has been done using Logan's chosen value (36eV) for the threshold energy in niobium.
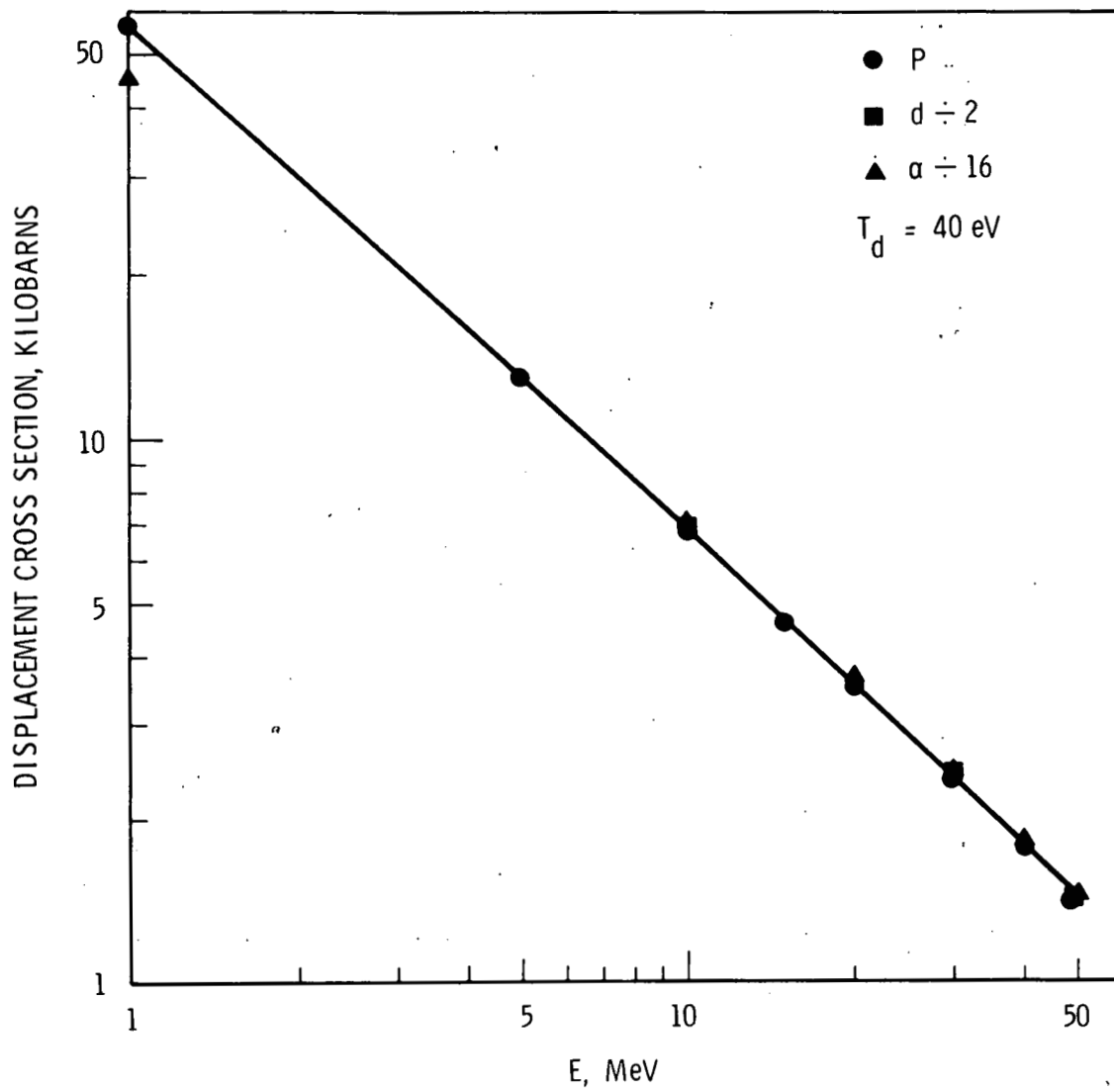
FIGURE 6. Total Displacement Cross Sections for Ni (Coulomb Scattering Only)
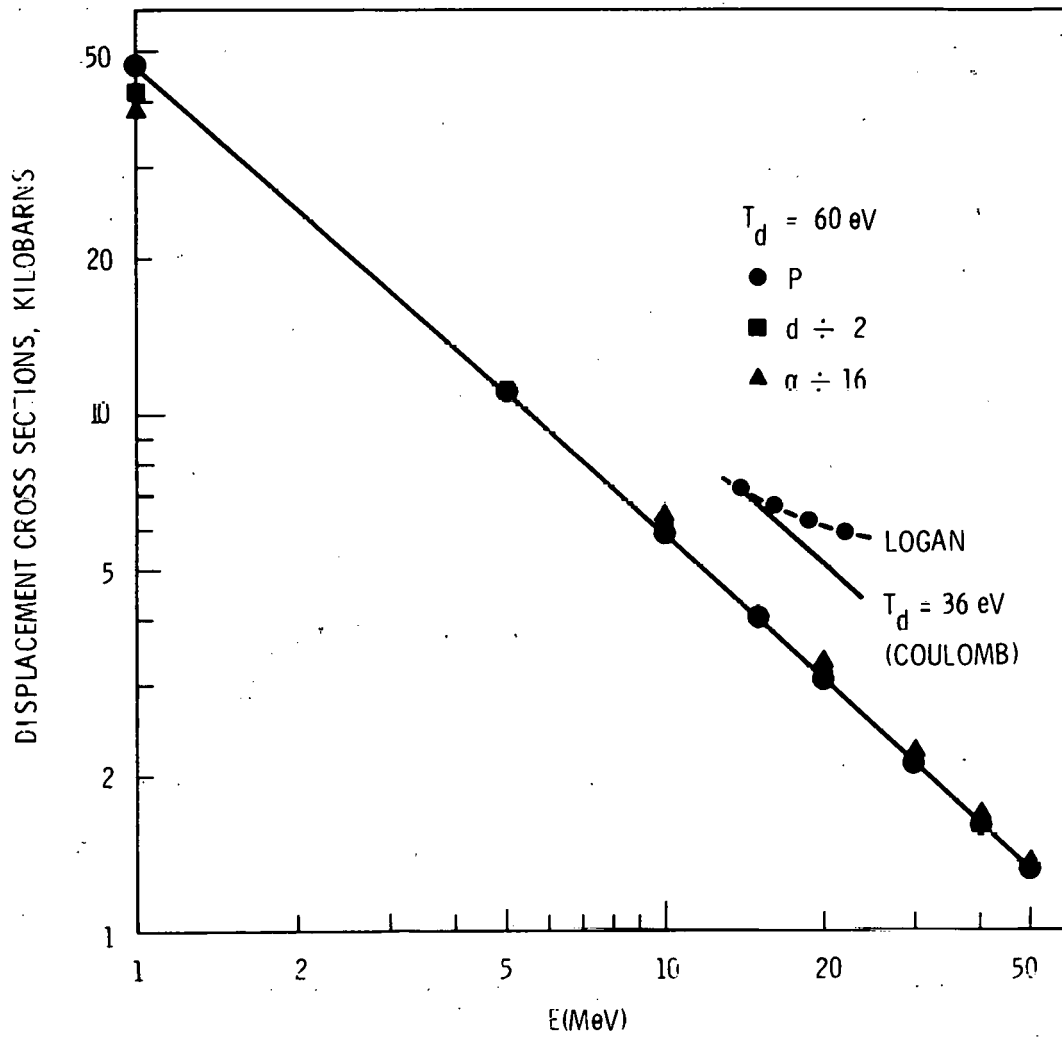
Figure 7. Total Displacement Cross Sections for Nb(Coulomb Scattering Only)

For 16.4 MeV protons the displacement cross-section from coulomb
scattering alone is about 2 percent smaller (see fig. 7) than the
cross-section obtained from the data of Logan, et al.[55] This dis-
crepancy decreases rapidly with decreasing energy over several MeV.
There is agreement around 14 MeV; no comparison was made at lower
energies.

Neutrons

Generally, theoretical estimates for neutron displacement cross-
sections should include inelastic scattering cross-sections. Errors
introduced by neglecting these cross-sections show large differences
between different materials. For example, their inclusion is not
as important for vanadium, chromium or iron exposed to 14 MeV neutrons,
as it is to the estimates for nickel irradiated by these neutrons.
Doran[50] has shown that nonelastic processes introduce a 11, 12 and 4
percent correction respectively for vanadium, iron and chromium.
This correction increases to about 75 percent for nickel.

Neutron displacement cross-sections and damage energies, ac-
counting for (n, n') and (n, 2n) reactions, have been estimated by
Doran,[56, 57] Kulcinski, Doran and Abdou[58] and by Robinson[52] respectively.
The inelastic contributions were found from numerical evaluations of

$$F(E) = \Sigma\ R_i(E)\ q_i(E)$$

where $R_i(E)$ is either the mean number of displacements per PKA, or
the mean energy going into a displacement per PKA, $F(E)$ is either
the displacement cross-section or the damage energy, respectively,
and $q_i(E)$ is the probability of exciting a given nuclear state.
The ENDF/B scattering parameters were used by these investigators;
14 MeV neutron displacement cross-sections resulting from these data
are listed in Table VII. Values of threshold displacement energies
which were used to determine the cross-sections from the displacement
functions, given by Kulcinski, et al.,[58] are listed also. The cross-
sections will shift in inverse proportion to fractional changes in
this threshold energy.

37

TABLE VII

Estimated Displacement Cross-Sections for 14 MeV Neutrons

Material	Displacement cross-section (kilobarns)	Effective Displacement Energy E_d(eV) x 1.67	Reference
Stainless Steel 18/10	1.91	55	57
Stainless Steel 316	2.22	40	58
Nickel	1.48*	55	57
Molybdenum	1.77	61	58
Vanadium	2.13	43	58
Niobium	1.72	60	58
Aluminum	1.90	27	58

*   Value quoted by Doran[57] multiplied by o.66 to make cross-sections consistent with values recommended by IAEA.[56]

The dpa rates due to 14 MeV neutrons from various fusion reactor designs were calculated using the cross-sections in Table VII. Table VIII shows resulting dpa rates for different wall materials in several of these reactor designs.

Cross-Section Profiles

Estimates of damage produced by ions must necessarily account for the number of atoms that are displaced (neglecting transport and interactions of defects). This number can then be used to compare relative damages for that given material irradiated with that particular species for which the calculation is made. Since displacement cross-sections shown in figures 6 and 7 increase rapidly with decreasing energy, the relative damage must increase in a similar manner. Species which have lost most of their energy (e.g. those near the end of their penetration depth) will produce relatively large numbers of displacements. The irradiated sample will therefore contain a disporportionate number of displaced atoms in that region of penetration which is equal to the range. This can be prevented by adjusting the sample thickness and energy of the ion so that the thickness is well below the range of the ion. The thickness and energy chosen can be determined from the cross-section profiles.

Cross-section profiles $\sigma(x)$ for protons, deuterons and alpha particles were determined from stopping power data $E(x)$ of Williamson, Boujot and Picard,[60] figures 8, 9 and 10. The resulting cross-sections $\sigma(x)$ for various values of E are shown in figures 11, 12 and 13. It is seen that if the ion energy is sufficiently large the cross-section increase is initially linear with energy and eventually becomes~hyperbolic. This implies that atomic displacements will not generally be distributed with equal concentration throughout the volume of the sample. It is conceivable, of course, that the dpa could be made more uniform by properly varying the sample orientation during irradiation. For example, the sample might be rotated in the ion beam.

TABLE VIII

DPA Rates Due to 14 MeV Neutrons
From Several D-T Fusion Facilities

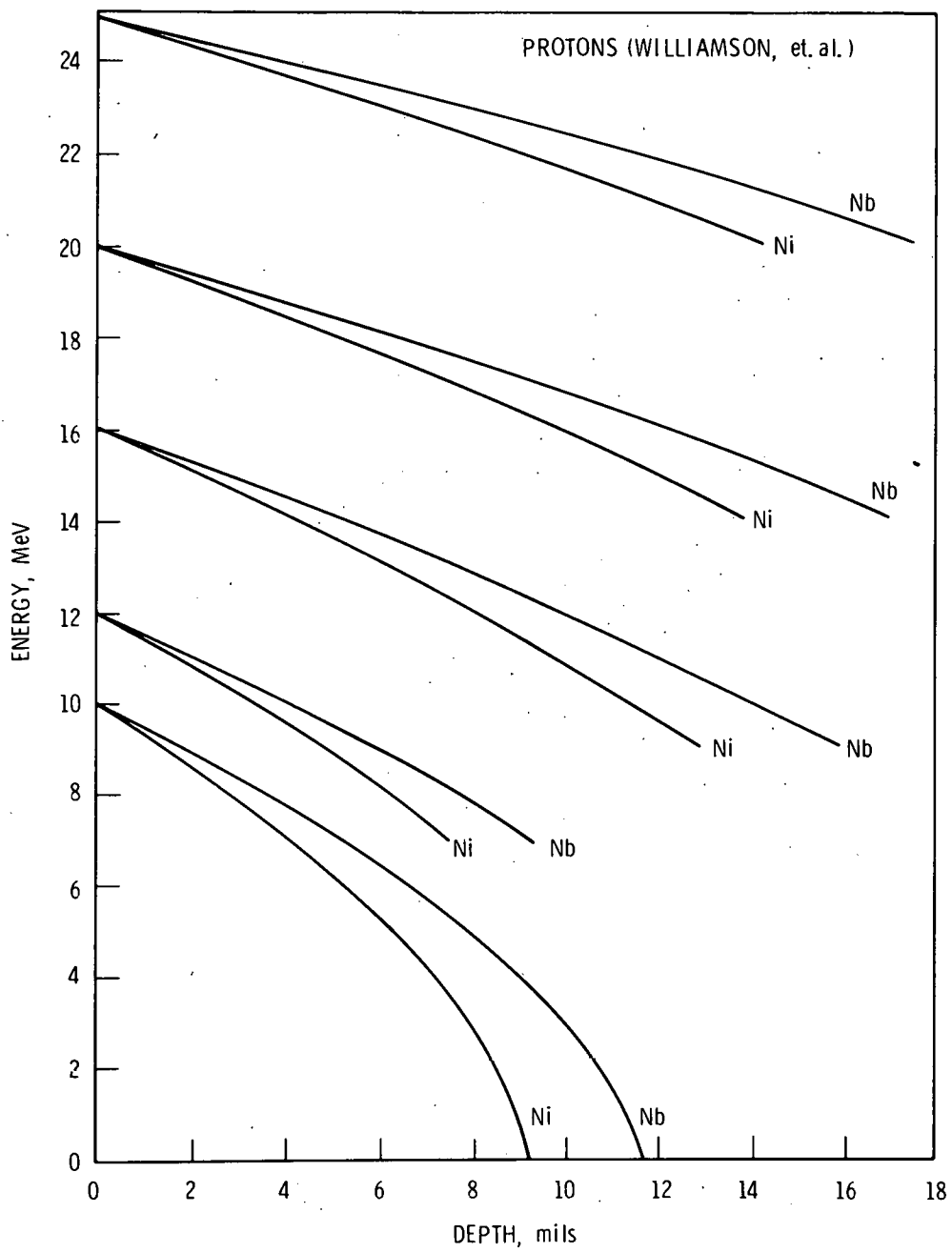| Facility	Flux $(10^{13}cm^{-2}sec^{-1})$	DPA $(10^{-7}sec^{-1})$						
		SS_{304}	SS_{316}	Ni	Mo	V	Nb	Al
UWMAK-II	5.3	1.01	1.2	0.8	0.9	1.1	0.9	1.0
PPPL	7.8	1.6	1.7	1.2	1.4	1.7	1.3	1.5
ORNL	2.0	0.4	0.4	0.3	0.3	0.4	0.3	0.4
FERF (Mirror)	6.0	1.1	1.3	0.8	1.0	1.3	1.0	1.2
RTNS	0.2	0.04	0.04	0.03	0.03	0.04	0.03	0.04

FIGURE 8. Energy-Depth Relations for Ni and Nb
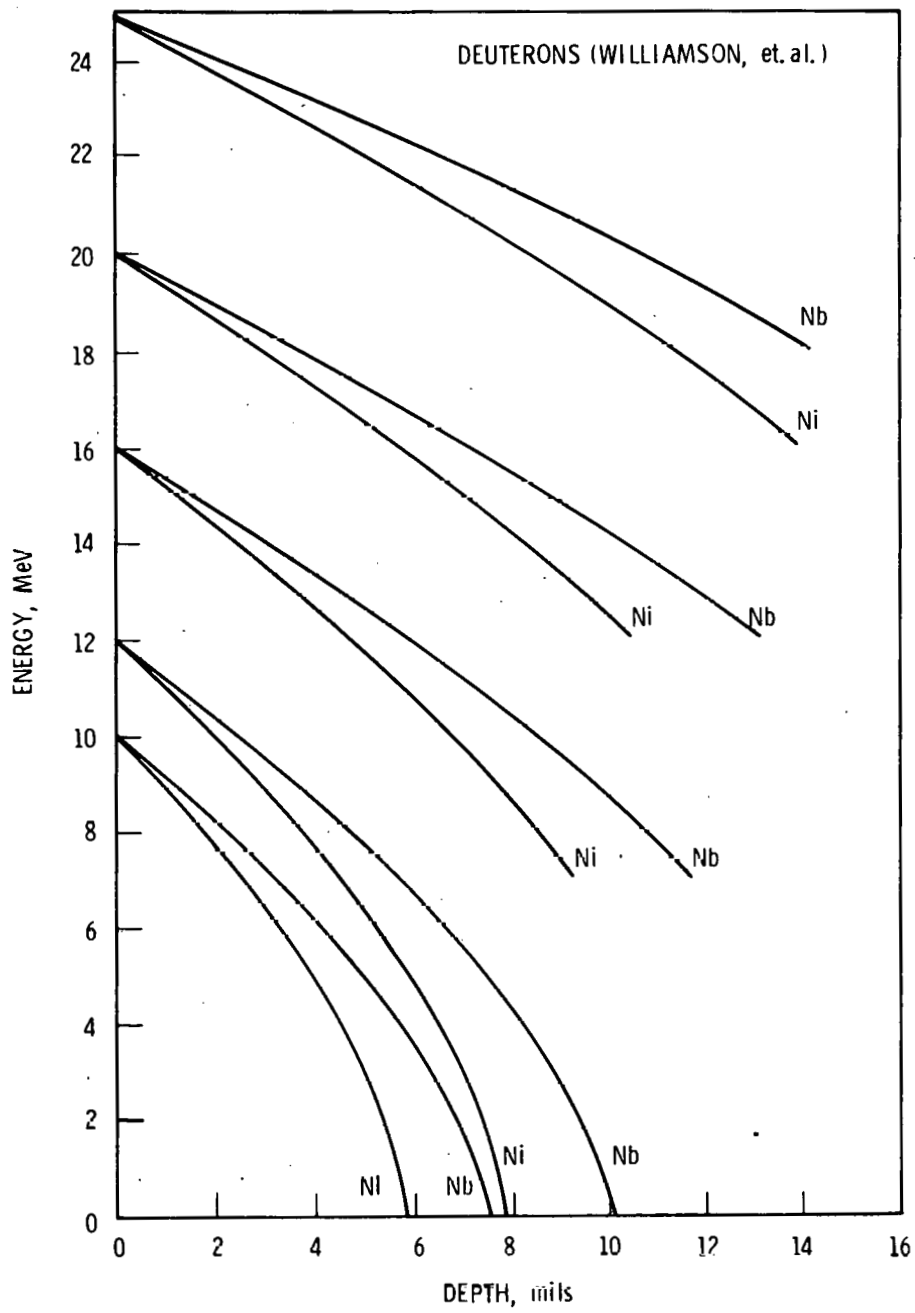
FIGURE 9. Energy Depth Relations for Ni and Nb
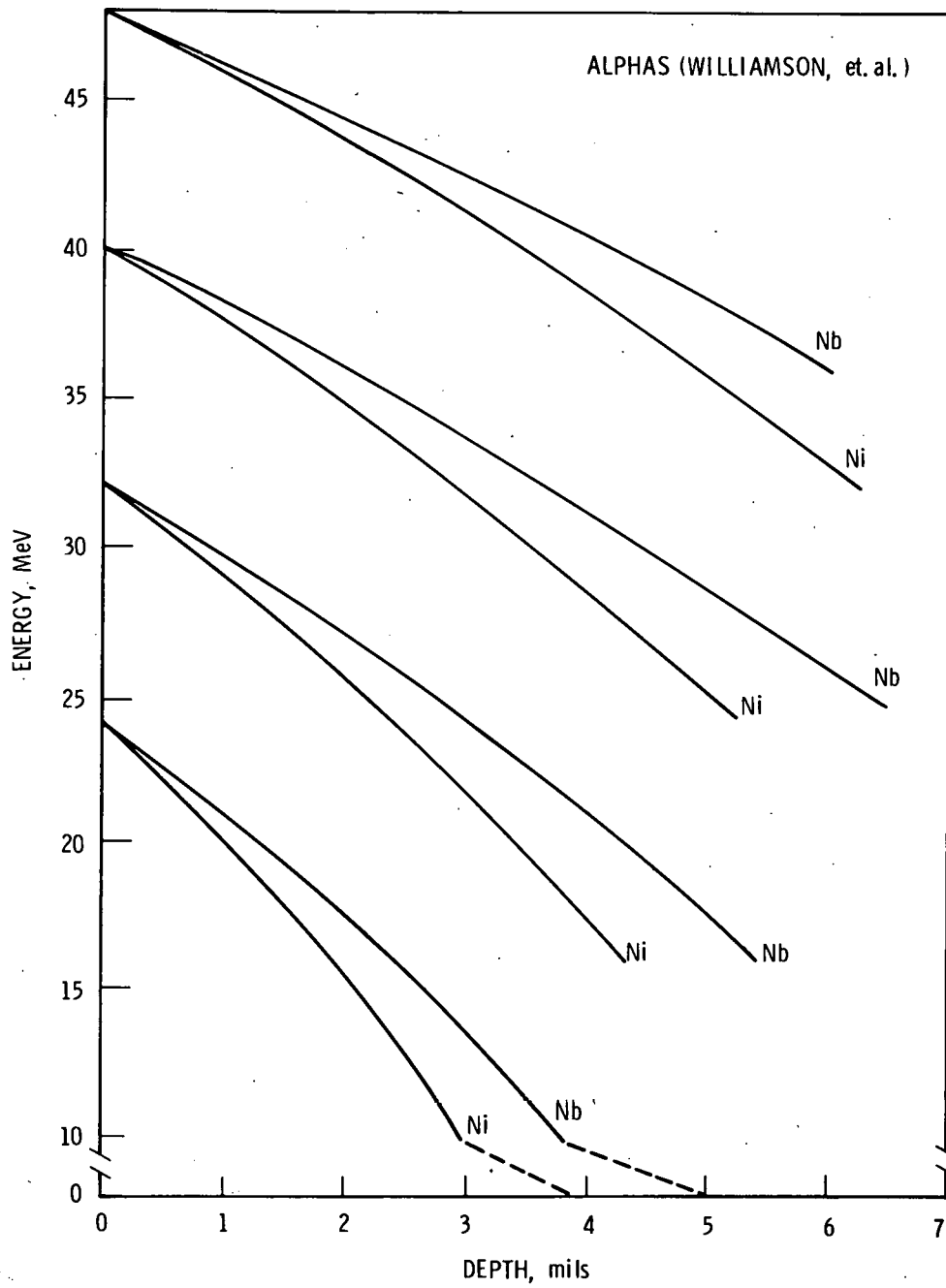
FIGURE 10. Alpha Energy Depth Releations for Ni and Nb
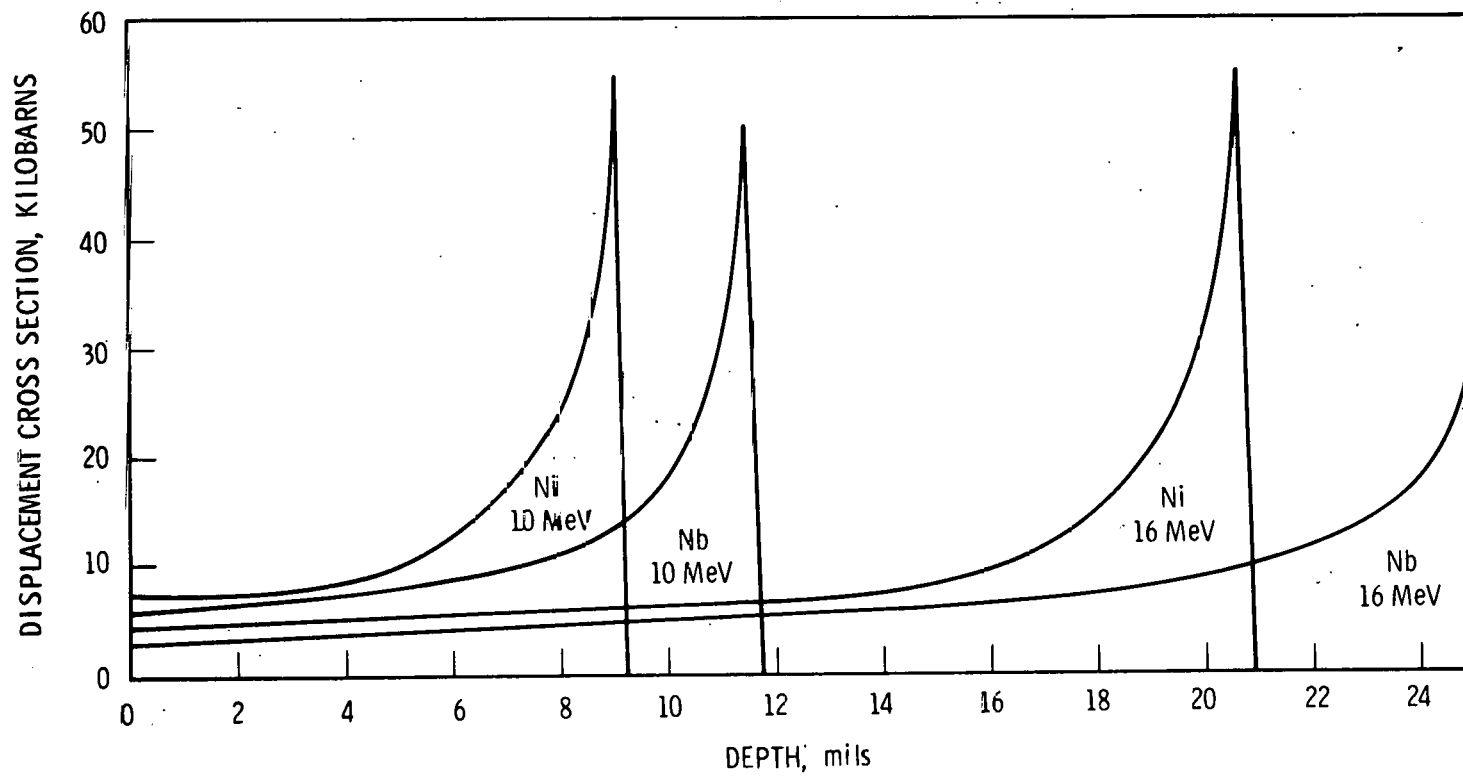
FIGURE 11. Displacement Cross Section Depth Profiles for Protons Incident on Ni and Nb

44
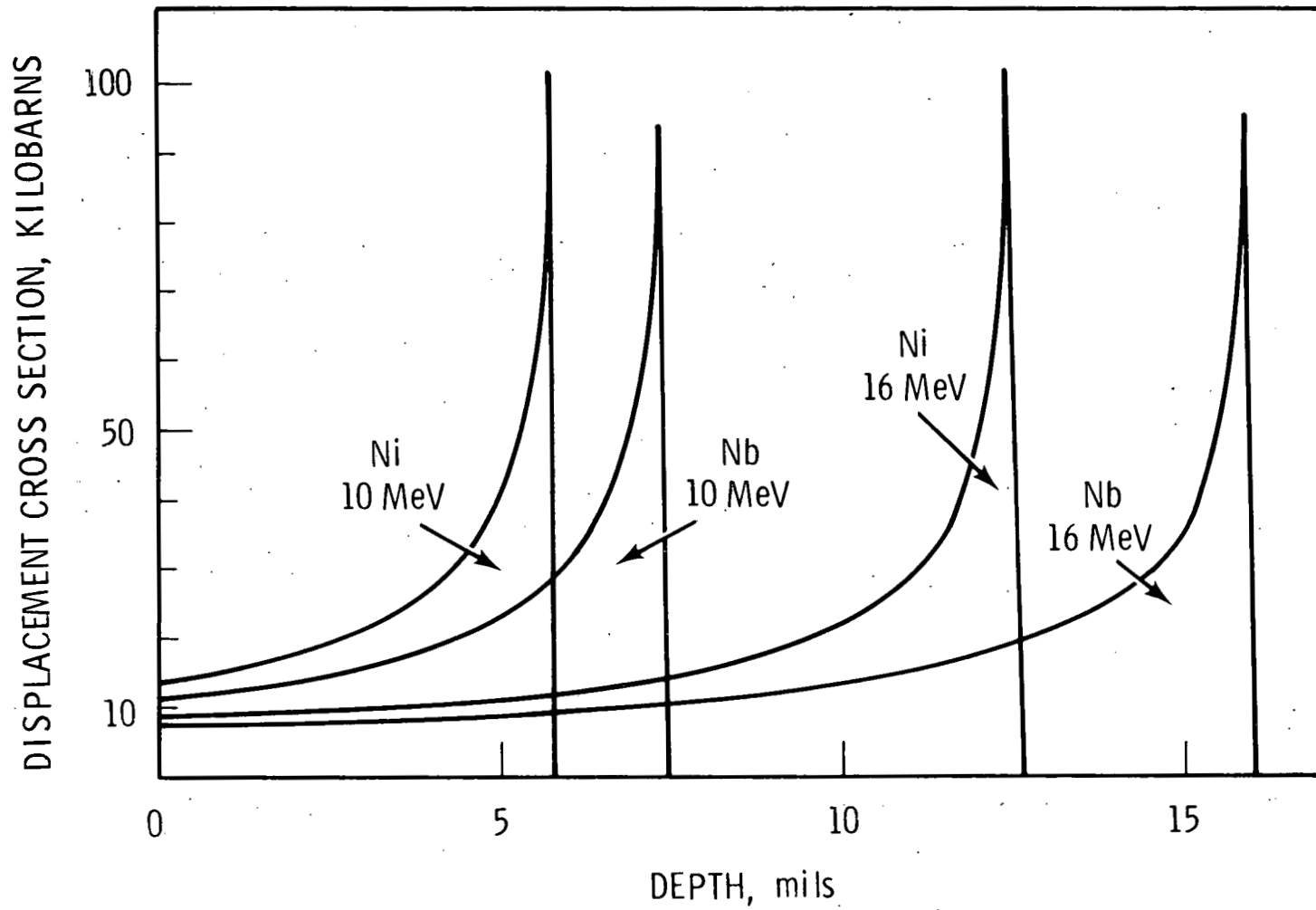
FIGURE 12. Displacement Cross-Section Profiles for Deuterons Incident on Ni and Nb
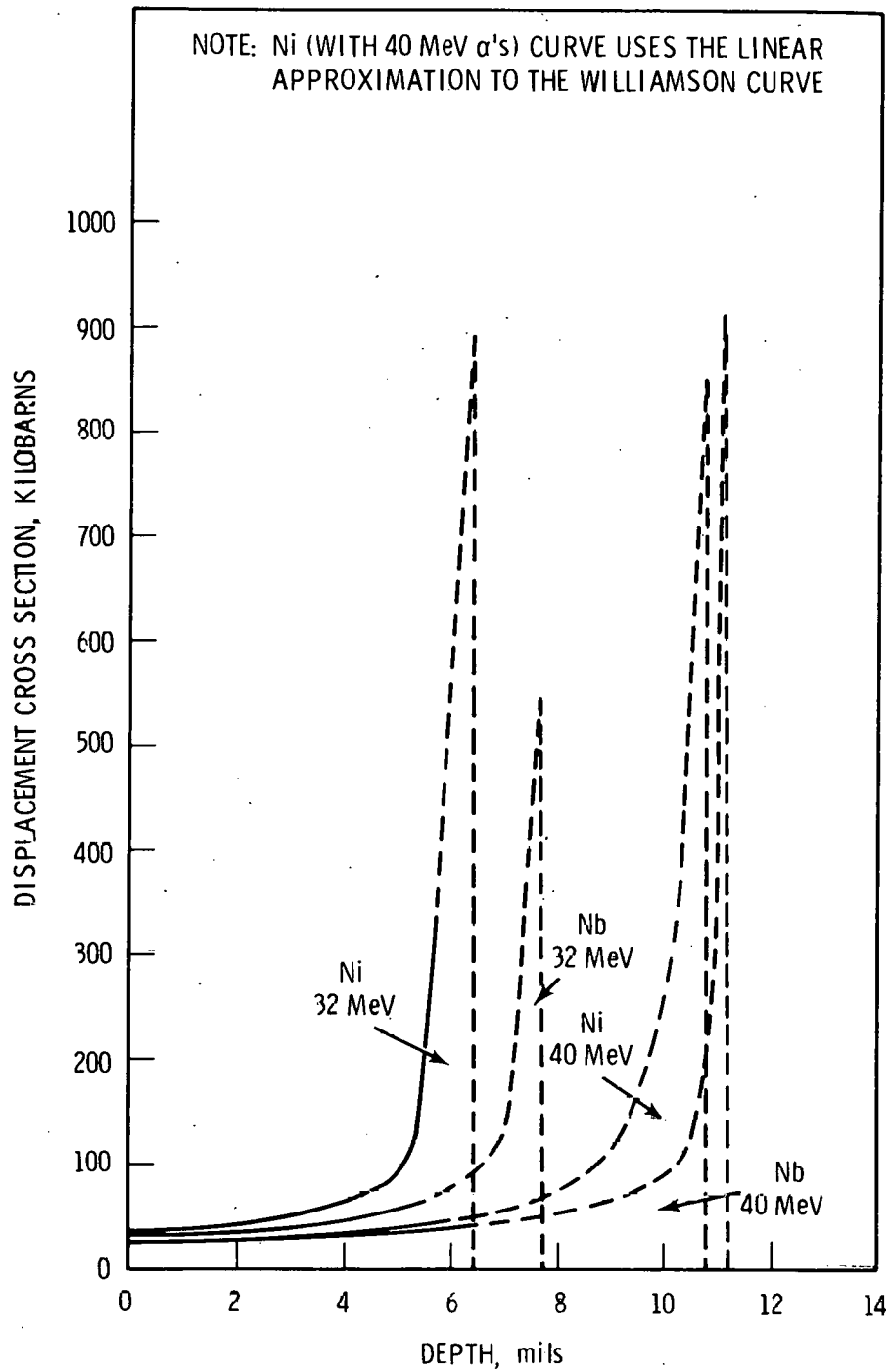
FIGURE 13. Displacement Profiles for Alphas Incident on Ni and Nb

It is important to know how this damage might be distributed. We assume a cylindrical sample rotating about its axis of symmetry and irradiated by ions from a single direction perpendicular to the sample axis (figure 14-a). Focussing our attention on a point on the perimeter we note that when the point is on the far side of the beam the displacement cross-section depends on the position so that

$$\sigma(x) = \sigma(r,\Theta) \quad ; \quad {}^{3\pi/2} <\Theta< {}^{\pi/2}$$

where r is the radial distance and Θ is the angle the radius vector makes with the beam. When the point of interest is on the near side of the beam (i.e. $\pi/2 \leq \Theta \leq 3\pi/2$) the displacement cross-section is constant. The time variation of the displacement cross-section will then look similar to that of figure 14-b. The exact shape will depend on the fraction of the displacement profile which is sampled by the point in question.

Magnitude of the dpa is given as a multiple of ω, by multiplying the ion flux by the area under the curve of figure 14-b. This can be compared with damage on the cylinder axis which experiences a constant displacement cross-section $\sigma(0)$ such as that shown by the dashed line in 14-b. We determine the fractional difference, $\sigma(r)/\sigma(0)$ -1, for two cases: 1) $\sigma(r)$ is a linear function of depth and 2) $\sigma(r)$ is hyperbolic with depth. The dpa created at position x is given by:

$$(dpa)_r = \int_0^\tau F \, \sigma(r,\Theta) \; dt$$

where F is the fluence and τ is the period of revolution. For case 1 we assume $\sigma = a + 2br \cos\Theta$ for $3\pi/2 <\Theta< \pi/2$ and $\sigma = a$ for $\pi/2 \leq \Theta \leq 3\pi/2$. For case 2, $\sigma = A\exp[2r \cos\Theta]$ for $3\pi/2 <\Theta< \pi/2$ and $\sigma = A$ for $\pi/2 \leq \Theta \leq 3\pi/2$. Constants a, b and A are determinable from the cross-section profiles.

Integration for case 1 yields:

$$(dpa)_r^{(1)} = \frac{2F\pi}{\omega} \left[a + \frac{2br}{\pi} \right]$$

(a)

(b)
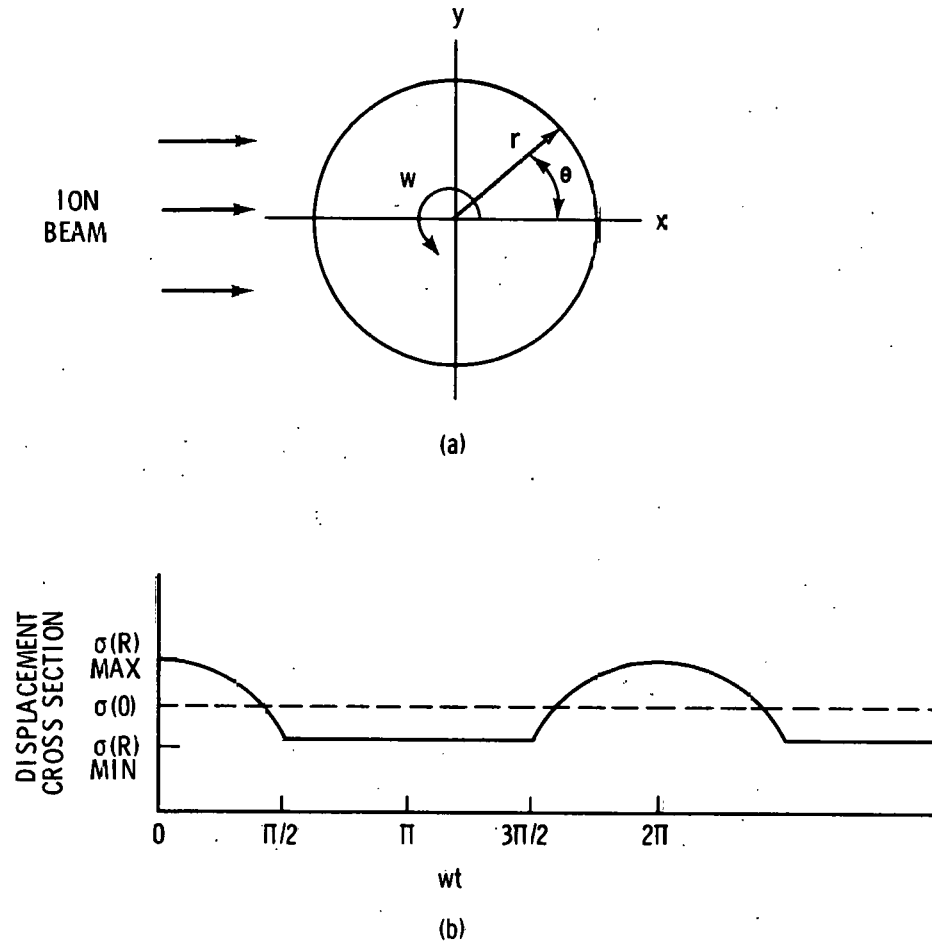
FIGURE 14. Displacement Cross Sections at r>0 a⁻ a Cylinder Rotating in an Ion Beam

(a)   Schematic of Ion Beam and Cylinder

(b)   Time Variation of the Cross Sec⁻ion: Solid Line Represents the Peripheral Point and Dashed Line Represents a Point on the Axis of the Cylinder

Integration of case 2 yields:

$$(dpa)_r^{(2)} = F \frac{2}{\omega} \int_0^{\pi/2} A \exp(2r \cos \Theta) \, d\Theta + F \, A\pi/\omega$$

$$= F \, A\frac{\pi}{\omega} [I_0 (2r) + 1]$$

where $I_0(2r)$ is the modified Bessel function of order zero.

We now define the dpa inhomogeneity as the fractional deviation of dpa at a peripheral point relative to the dpa at the center of the wire. This deviation is shown for both cases in figures 15 and 16. We have chosen values for a and b which are representative of the dpa profiles for 16 MeV deuterons on Ni discussed previously. For this linear representative case 2.5 mils corresponds to 5 percent. A zero point occurs at a radius of about 2.3 mils for case 2.

Note that the dpa at the small radius inhomogeneity is negative for both cases. That is to say, the dpa on the axis is greater than that on the periphery. The change in the sign of the inhomogeneity of case 2 is due to the large change in displacement cross-section with penetration. This change becomes so large that it eventually gives dominance to the peripheral dpa relative to dpa production at the center. In such a case the peripheral point can be at the highest dpa position only a relatively short time and still accumulate more dpa than the center.

It can be concluded that inhomogeneity, as defined here, vanishes at some radius for the case where the displacement cross-section varies exponentially with penetration distance. The displacement cross-section profiles shown in figures 11 and 12 indicate such a behavior might be expected for deuterons and protons on Ni and Nb if the bombarding energies are about 10 MeV and wire diameters are ~0.125 mm (5 mils). It must be kept in mind that this analysis for case 2 assumes an exponentially increasing displacement cross-section. The true shape is not known. Because of straggling, uncertainties in range calculations become large at low energies, the shape of the cross-section profiles near the end of the range cannot be estimated with confidence. Until this is possible it is best to design experiments so that damage created can be estimated from the linear portion of the cross-section profiles.

49
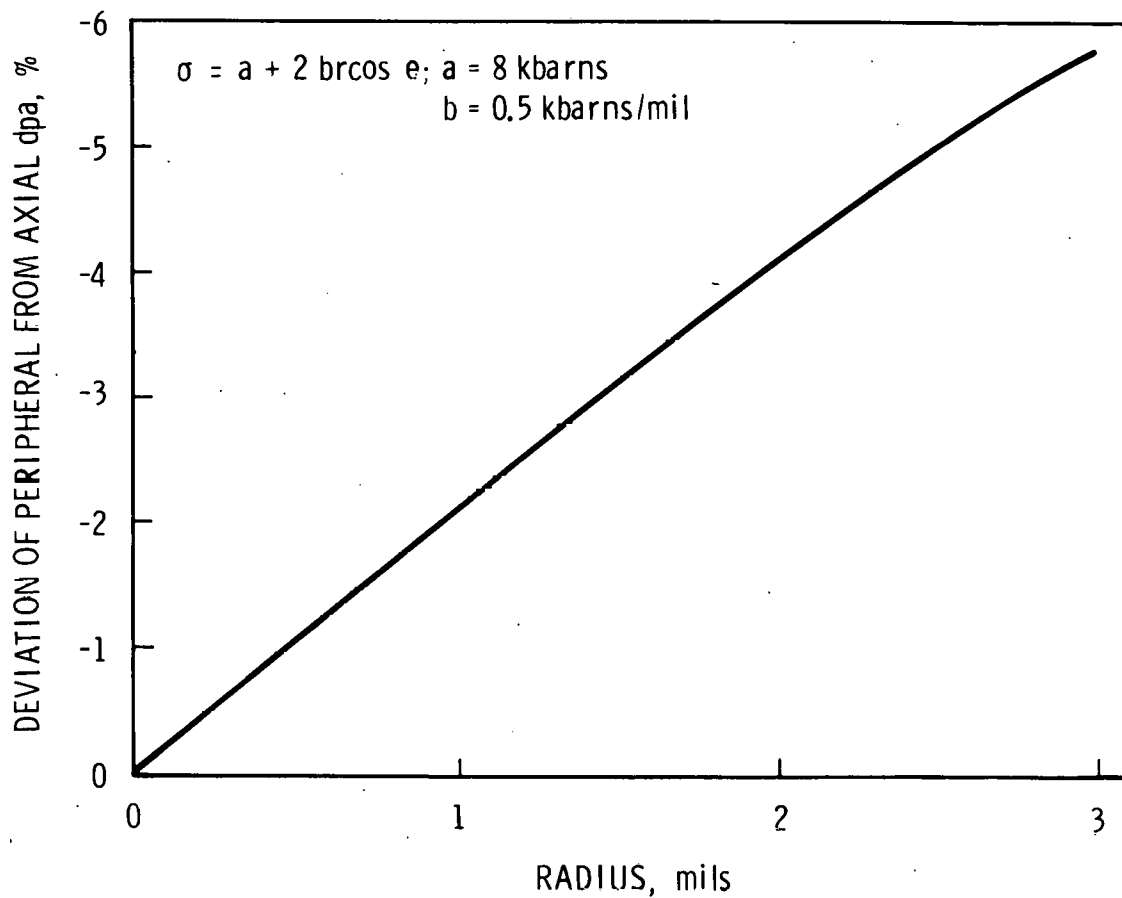
FIGURE 15. Comparison Between DPA at Center and Periphery
of a Rotating Wire in a 16 MeV Deuteron Beam
Assuming a Linear Displacement Cross Section
Profile
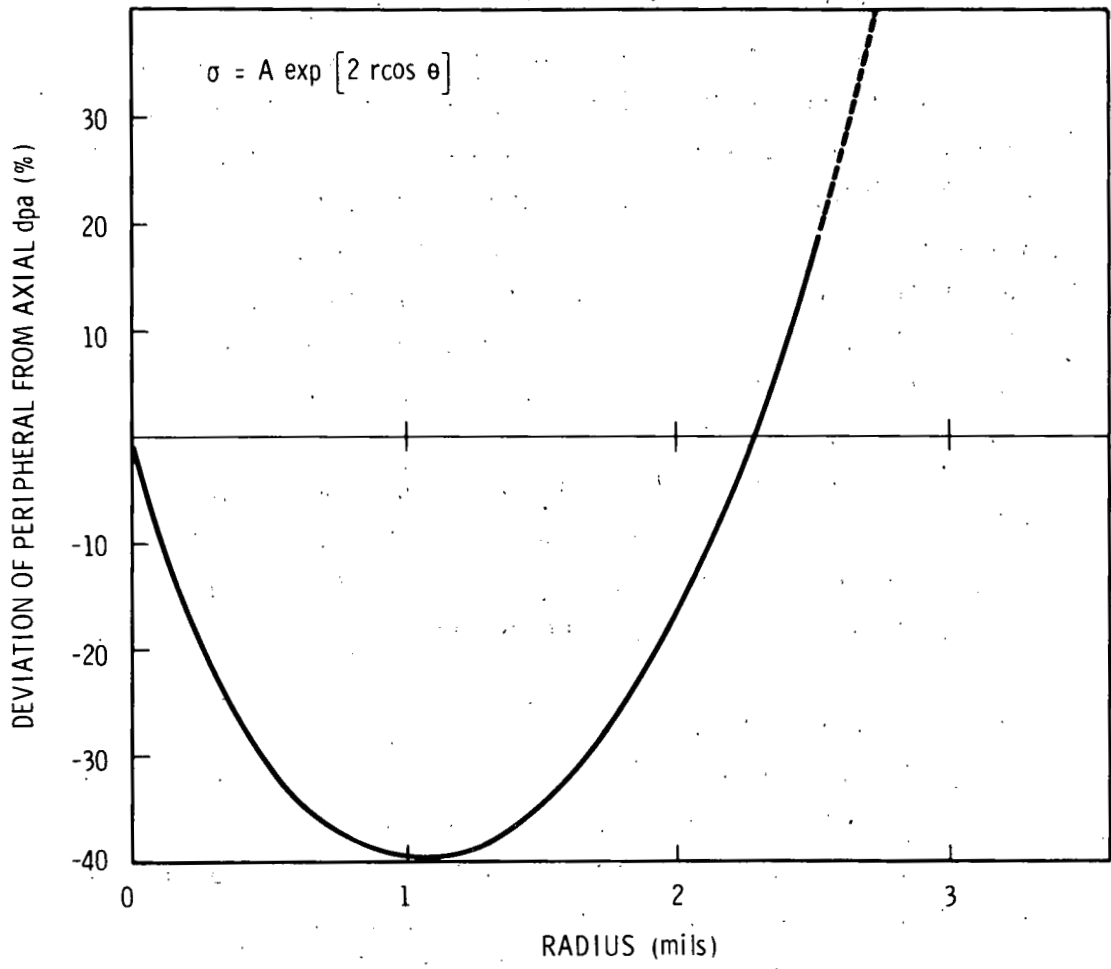
FIGURE 16. Comparison Between DPA at Center and Periphery
of a Rotating Wire in an Ion Beam Assuming an
Exponential Displacement Cross Section Profile

51

γ. Sample Heating and Cooling Considerations

A substantial portion of the ion beam energy may be converted to the molar internal energy in samples intercepting the beam. The fraction of beam energy which goes into thermally exciting the sample depends on the sample thickness and can be estimated from the energy profiles (figures 8, 9 and 10) and displacement cross-sections (figures 6 and 7). For example, from figure 9, it is seen that for 16 MeV deuterons about 23 percent of the energy of the impinging ion energy is absorbed by a 0.125 mm (5 mil) nickel target, while the same target absorbs 60 percent of the energy of a 10 MeV deuteron beam. The portion of this energy which is used to create displacements is relatively small as indicated by the average value for the cross-section $\bar{\sigma}$, estimated from figures 9 and 6 and the small values used for threshold energies (E_d). That is to say, to create displacements the average ion expends $\bar{\sigma}n\ell E_d/E_0$ of its original energy, which for 16 MeV deuterons on a 0.125 mm Ni target is about 0.02 percent. In this expression n is the number of atoms per cm^3, ℓ is the target thickness and E_0 is the ion kinetic energy; the threshold energy E_d is chosen to be 40 eV. Therefore, if only the near linear part of the displacement cross-section profile is sampled, by far the largest portion of the kinetic energy absorbed goes toward increasing the molar internal energy of the target. This is, of course, not necessarily the case if the target thickness is increased so that "end of range" displacement cross-sections are included. The displacement cross-sections in this range could increase orders of magnitude above that of the linear portion of the profiles. A much larger fraction of the energy of the kinetic energy would then be used to create displacements.

The relatively large efficiency of conversion from kinetic to molar internal energy imposes limits on the rate of production of dpa or damage energy. That is to say, steady state conditions consistent with a given set of experimental boundary conditions may

not be possible when ion currents exceed some limiting value. These
limits can be estimated easily for given sample cooling conditions
and sample geometries. This has been done in the following manner
for circular wires cooled by a helium gas stream.

Suppose energy density flow into a wire of radius (a) is Q.
This is the energy density created by an impinging ion beam at current
density J. We assume uniform deposition throughout the wire. As
we have seen, this is not the case, but uniformity is approached
by a rotating wire which samples only the relatively linear portion
of the dpa profile. The rate of energy production in the wire is
given by γJE, where E is the ion energy and γ is the fraction
absorbed. For steady state and neglecting radiation exchange with
the gas we have:

$$\pi h(T_1 - T_g) + \frac{\pi a}{\ell^2} k(\Delta T)_e + \frac{\pi a}{2\ell} \sigma\varepsilon(T_1^4 - T_2^4) = \gamma JE$$

where T is temperature, ℓ is wire length and k, h, σ and ε are thermal
conductivity of wire, convective heat transfer coefficient, Stefan-
Boltzman constant and emissivity respectively. Subscripts g, e, 1
and 2 indicate temperatures of gas, wire end, wire surface and shroud
or vacuum chamber respectively.

For wire temperatures less than the order of $1000^{\circ}C$ and wire
radii in the range appropriate for uniform "damage" from ions,
radiation and end loss effects are small relative to convective losses
by helium gas. This is made obvious by writing $h = \frac{K_n k_g}{2a}$, where
K_n is the Nusselt number and k_g is thermal conductivity of the gas.
Since K_n will be greater than 0.6, and k_g is greater than 10^{-1}
Watt meter/meter^2 $^{\circ}K$ the first term in the above equation dominates
as long as the wire dimensions are practicable for this work. There-
fore, second and third terms on the left hand side of the above
equation are neglected and the equation becomes;

$$\frac{\pi K_n k_g}{2a} \quad (T_1 - T_g) = \gamma JE$$

Elimination of T_1 between the above equation and the solution to the steady state heat flow equation (cylindrical coordinates with temperature T_a constant along the axis and symmetric about the axis) gives the limiting current density value:

$$J = \frac{4\pi k k_g K_n (T_a - T_g)}{Ea(K_n k_g + 8K)}$$

or:

$$J = \frac{4\pi k k_g C(R_e)^n (T_a - T_g)}{\gamma Ea [C(R_e)^n k_g + 8k]}$$

where K_n has been replaced by $C(R_e)^n$ (Holman, J. P.[61], Hilpert, R.[62]), γ corrects E to the value absorbed by the sample, R_e is the Reynold's number and C and n are values from the experimental data of Hilpert and tabulated by Holman, and T_a is temperature on the wire axis. The equation is easily changed to give limiting dpa rate values by multiplying by $\bar{\sigma}/1.6 \times 10^{-19}$.

The dpa rate limits were calculated for Ni and Nb using the above equation for J and experimental values of C and n as tabulated by Holman. Some of the low temperature ($\sim100^\circ$C) low gas speed (~1 m/sec) calculations necessitated the use of R_e values slightly smaller than the minimum values for which C and n are tabulated. In such cases the C, n values used were those related to the smallest R_e tabulation, i.e., 0.4. Resulting isotherms and constant gas flow rate curves are shown in figures 17-26, respectively. It is seen that increasing the wire radius decreases the possible dpa rate while increasing cooling gas speed increases the limiting dpa rate. For deuterons 0.125 and 0.25 mm radii Ni wires will have the same limiting dpa rate if operating temperature is 370°C and gas speeds are 10 and 100 m/sec, respectively. At 500°C this doubling of the radius decreases the limiting dpa rate by about 65 percent. Maximum deuteron initiated dpa rate in Ni at 500°C will occur for 13 MeV deuterons (in order to operate along the linear portion of the dpa profile) and will vary from 8.1×10^{-7} to 4.8×10^{-6} dpa/sec, depending on He gas flow. This variation is depicted as the dotted line of figure 18.
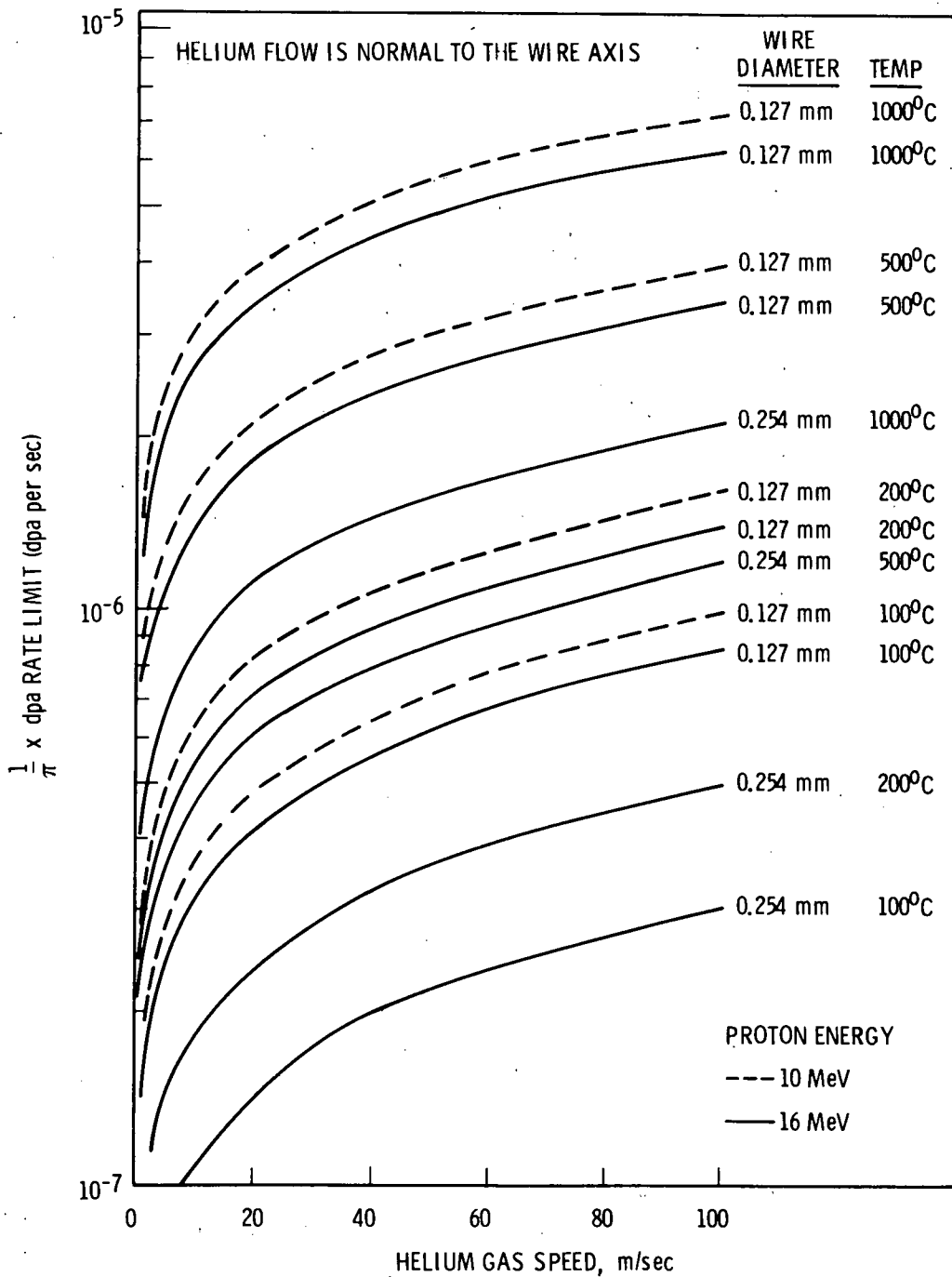
FIGURE 17. Calculated DPA Rate Limit Isotherms for Incident
Protons on Helium Cooled Ni Wire

55
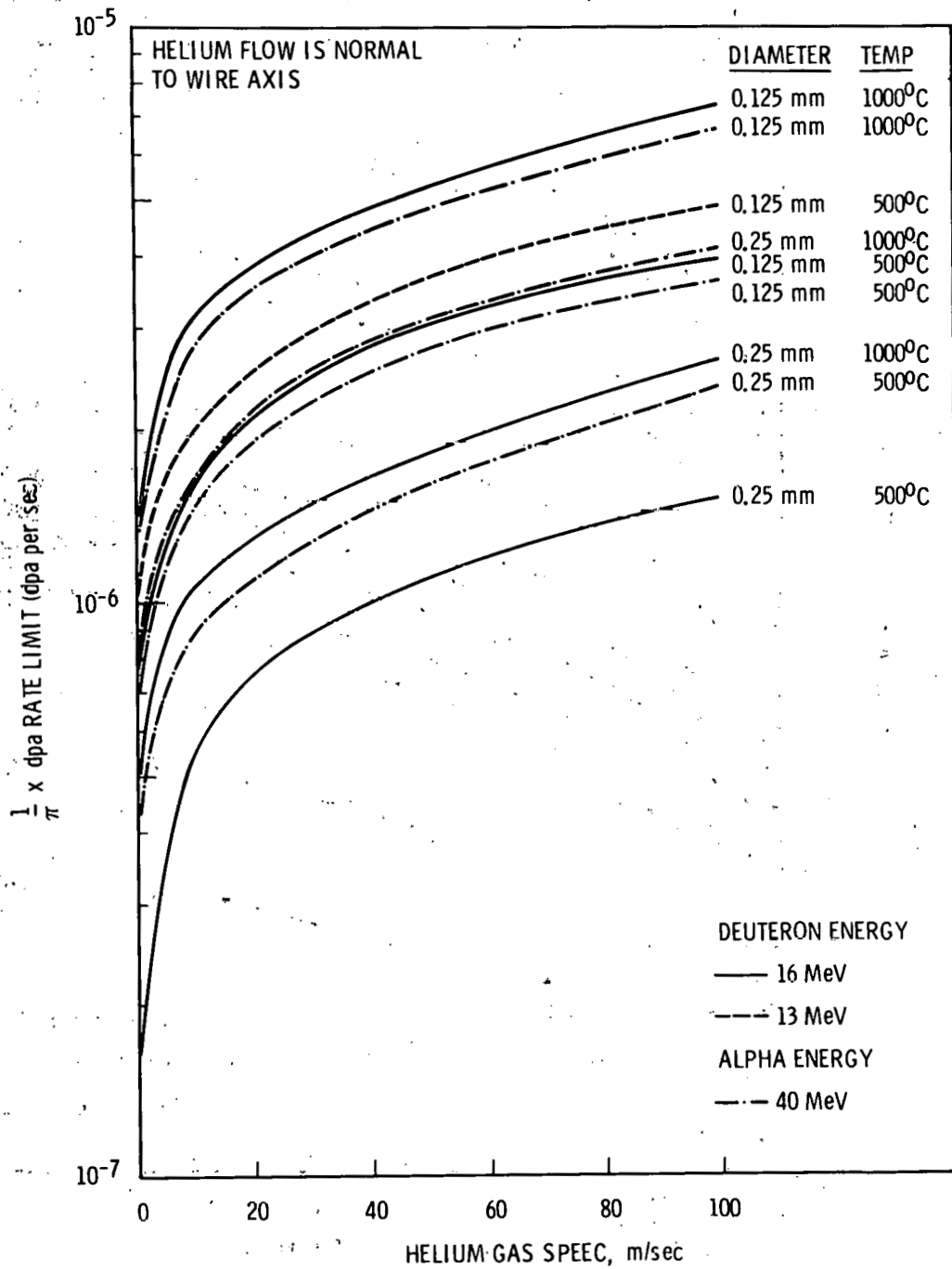
FIGURE 18. Calculated DPA Rate Limit Isotherms for d and α on Ni Wire

FIGURE 19. Calculated Maximum DPA Rates in He Cooled Ni Wires
Subjected to 10 MeV and 16 MeV Protons
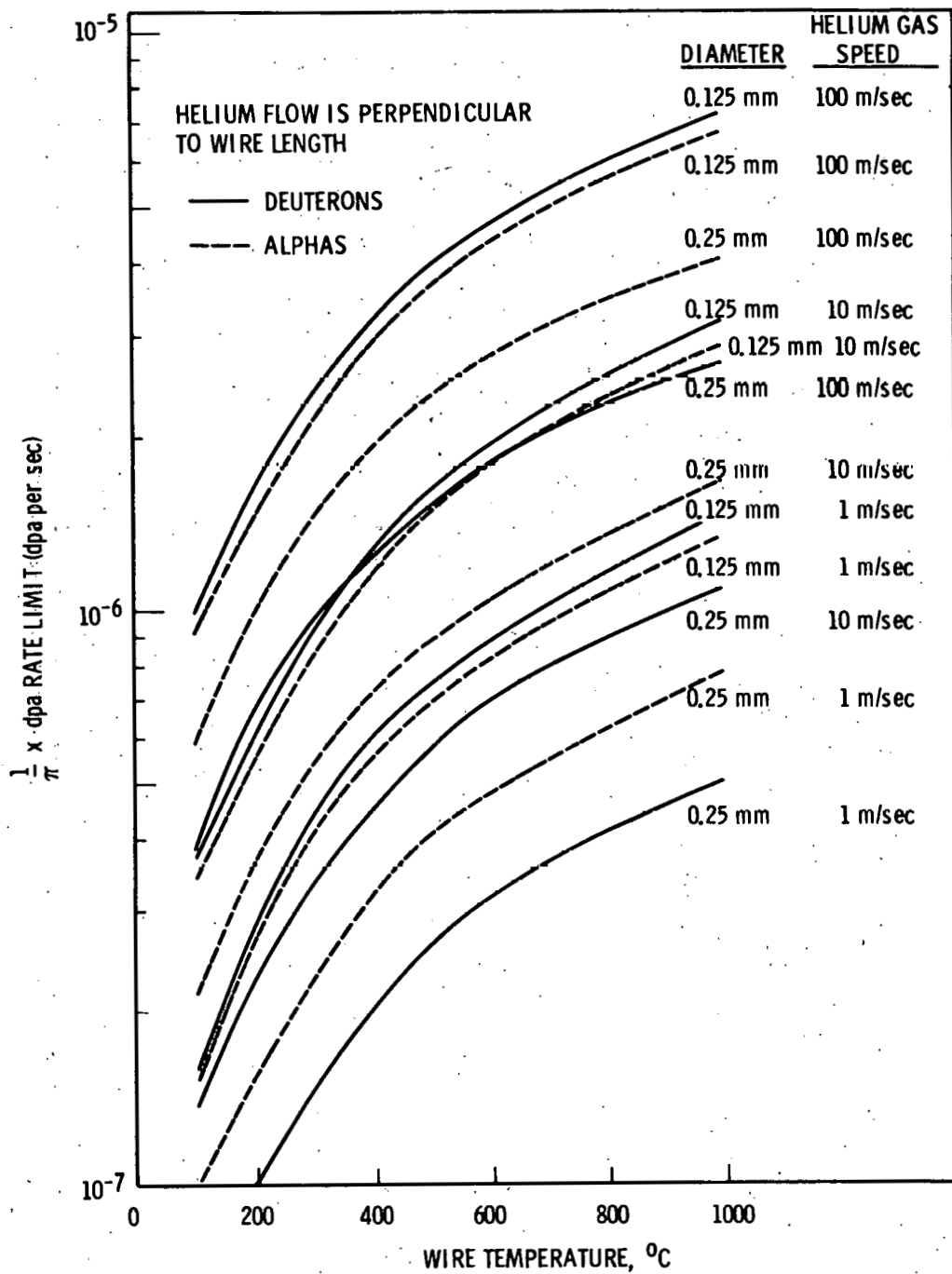
FIGURE 20. Calculated Maximum DPA Rates in He Cooled Ni Wires Subjected to 16 MeV deuterons and 40 MeV Alphas

58
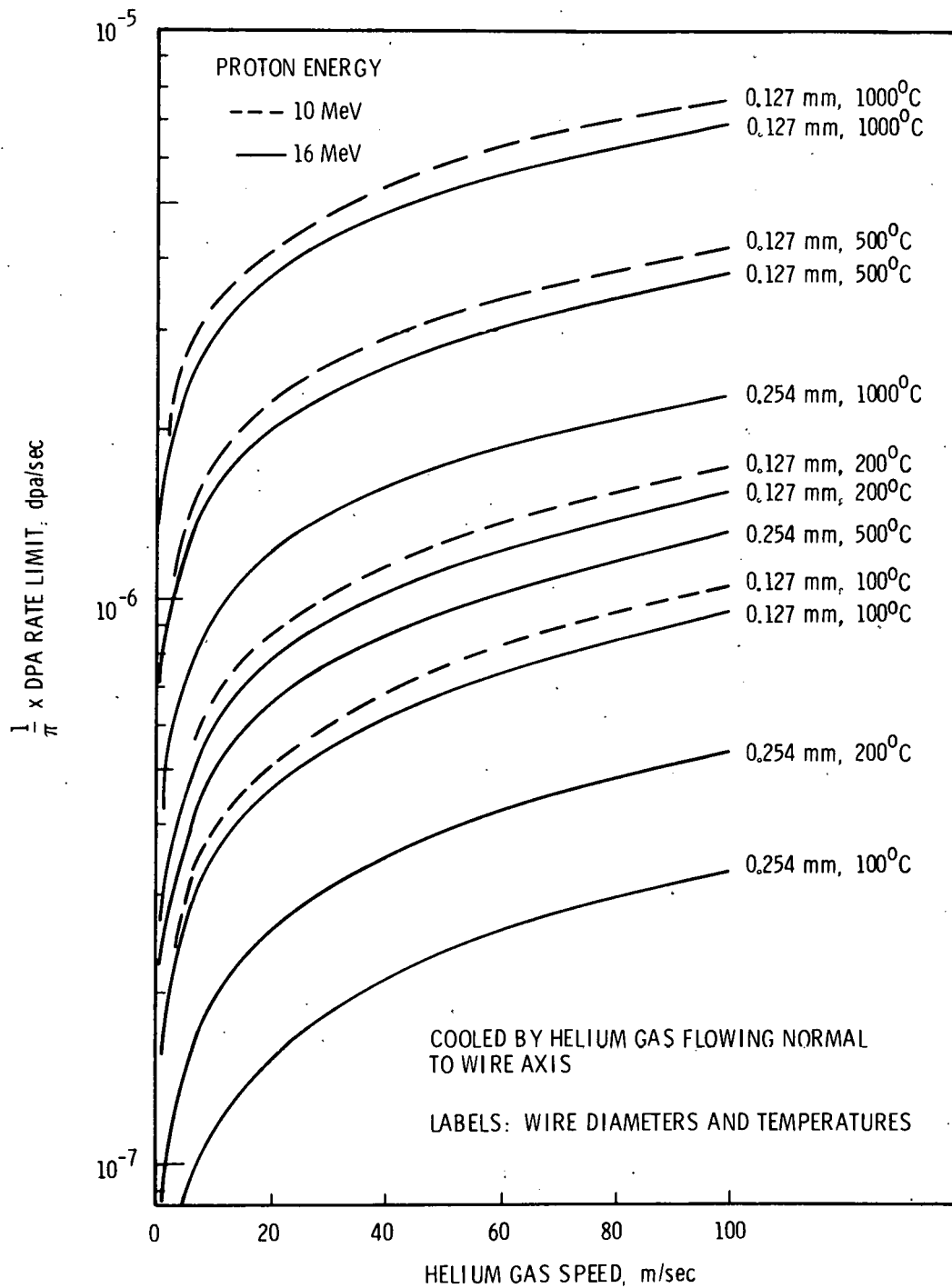
FIGURE 21. Calculated DPA Rate Limit Isotherms for Incident Proton Beam on Nb Wires
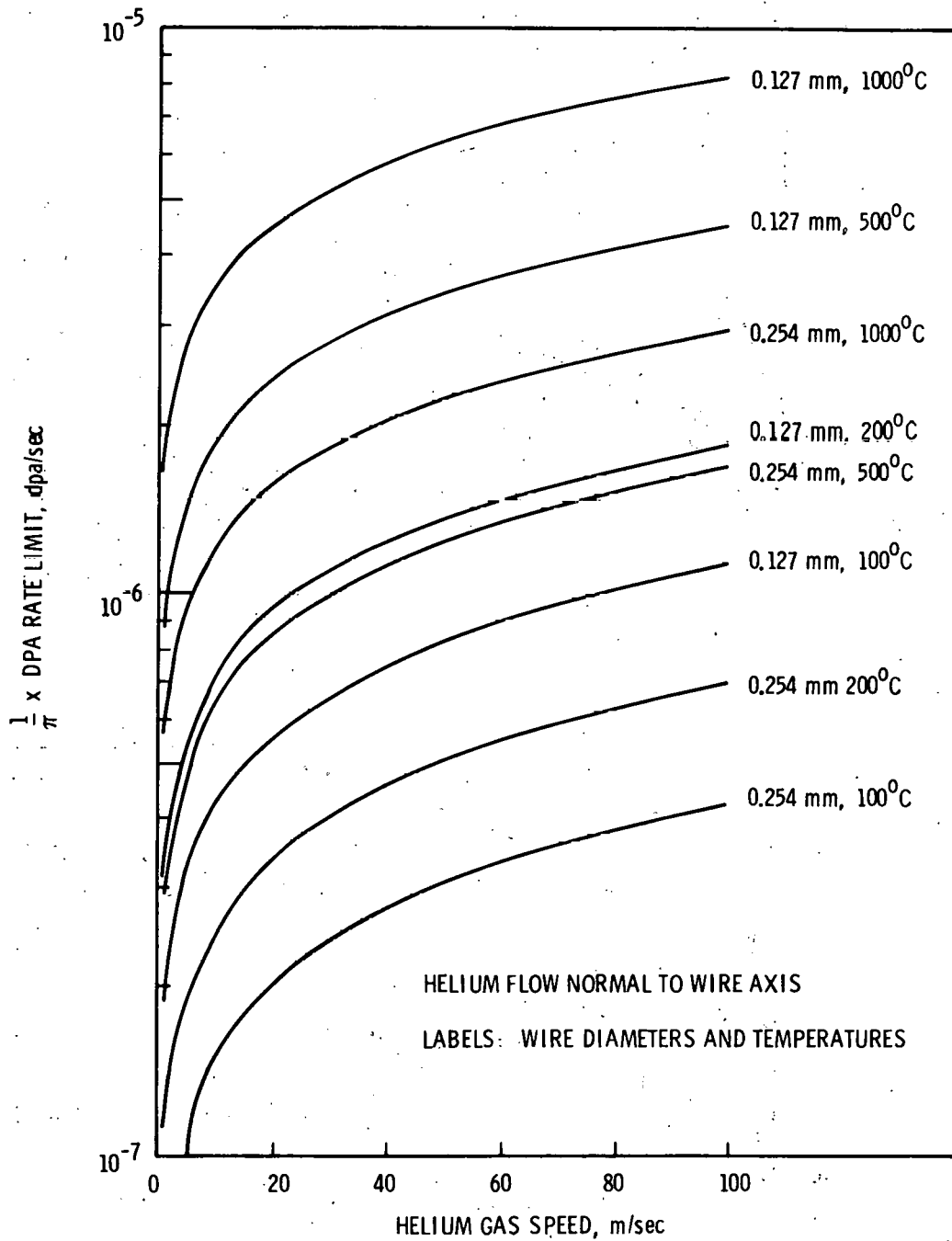
FIGURE 22. Calculated DPA Rate Limit Isotherms for Incident 16 MeV deuteron Beam on Nb Wires

60
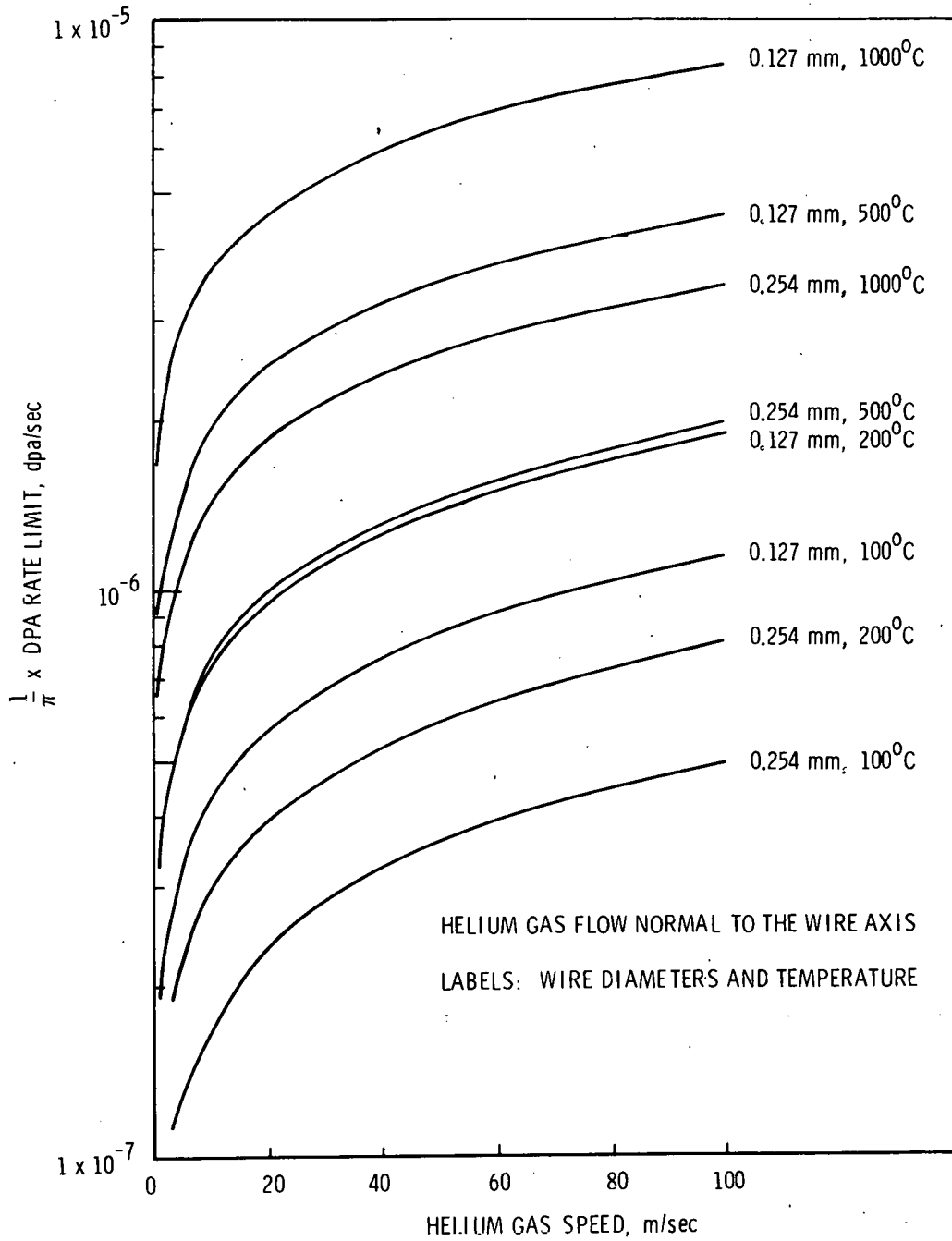
FIGURE 23. Calculated DPA Rate Limit Isotherms for Incident
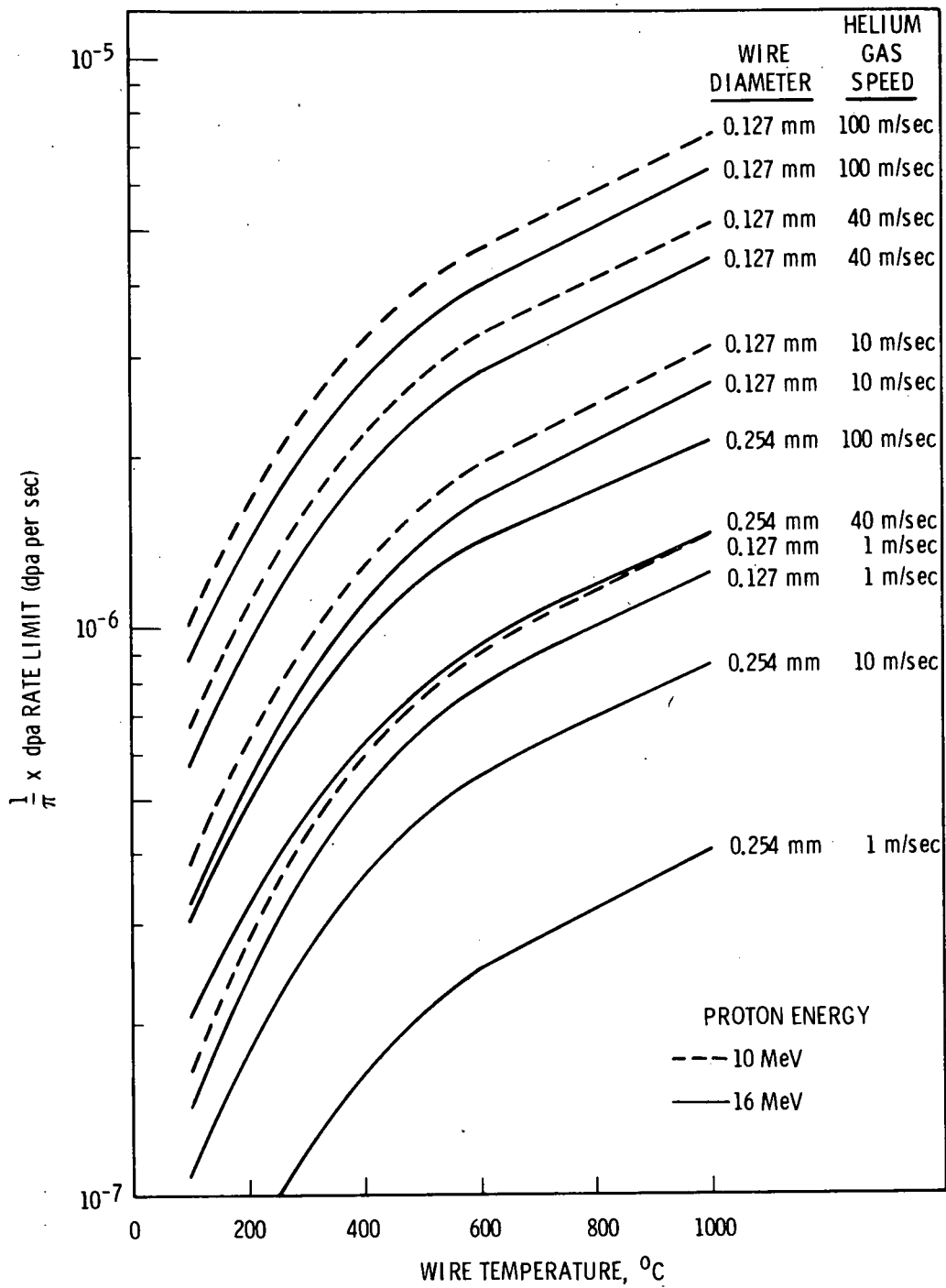40 MeV Alpha Beam on Nb Wires

61
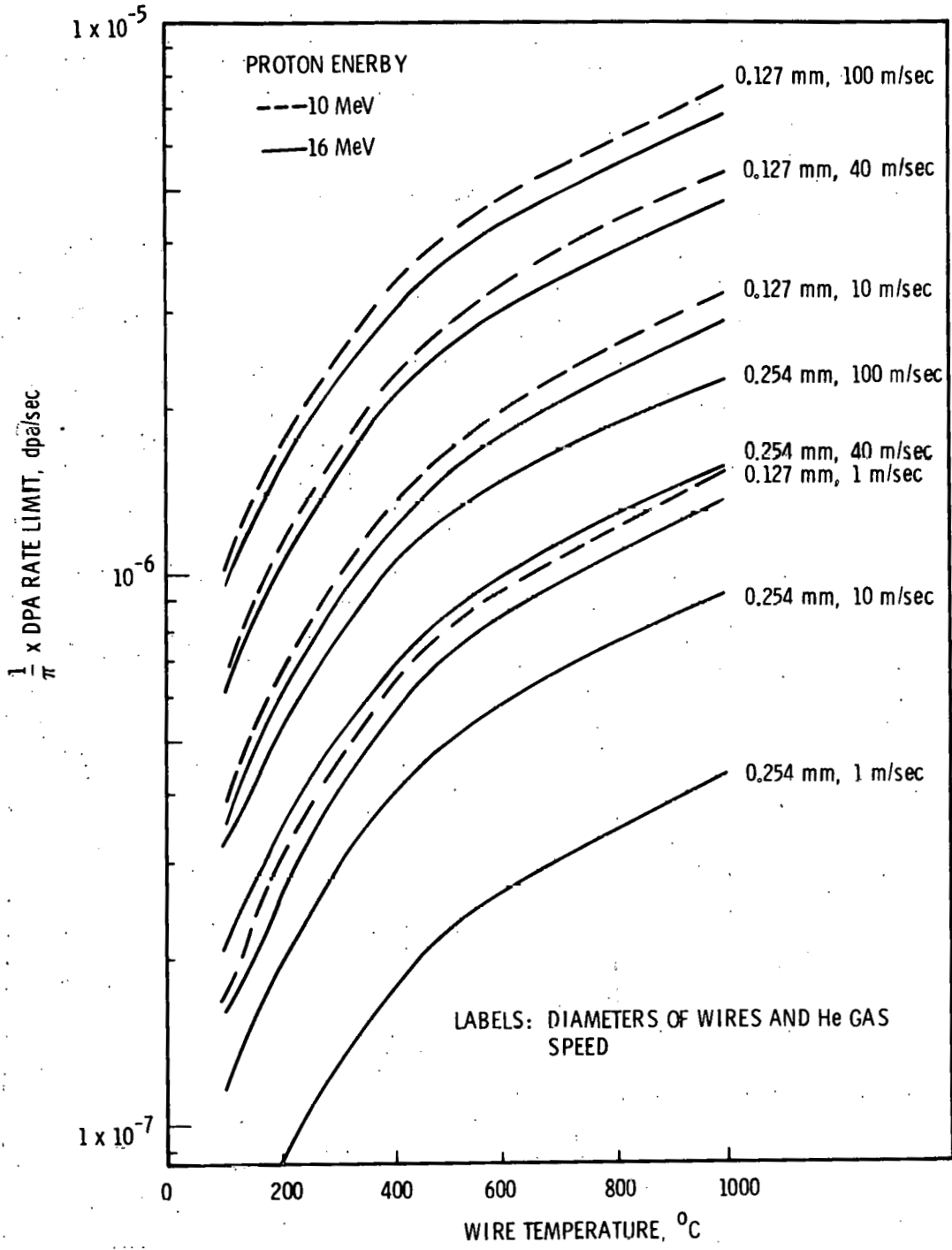
FIGURE 24. Calculated Maximum DPA Rates in He-Cooled Nb Wires Subjected to 10 MeV and 16 MeV Protons

62
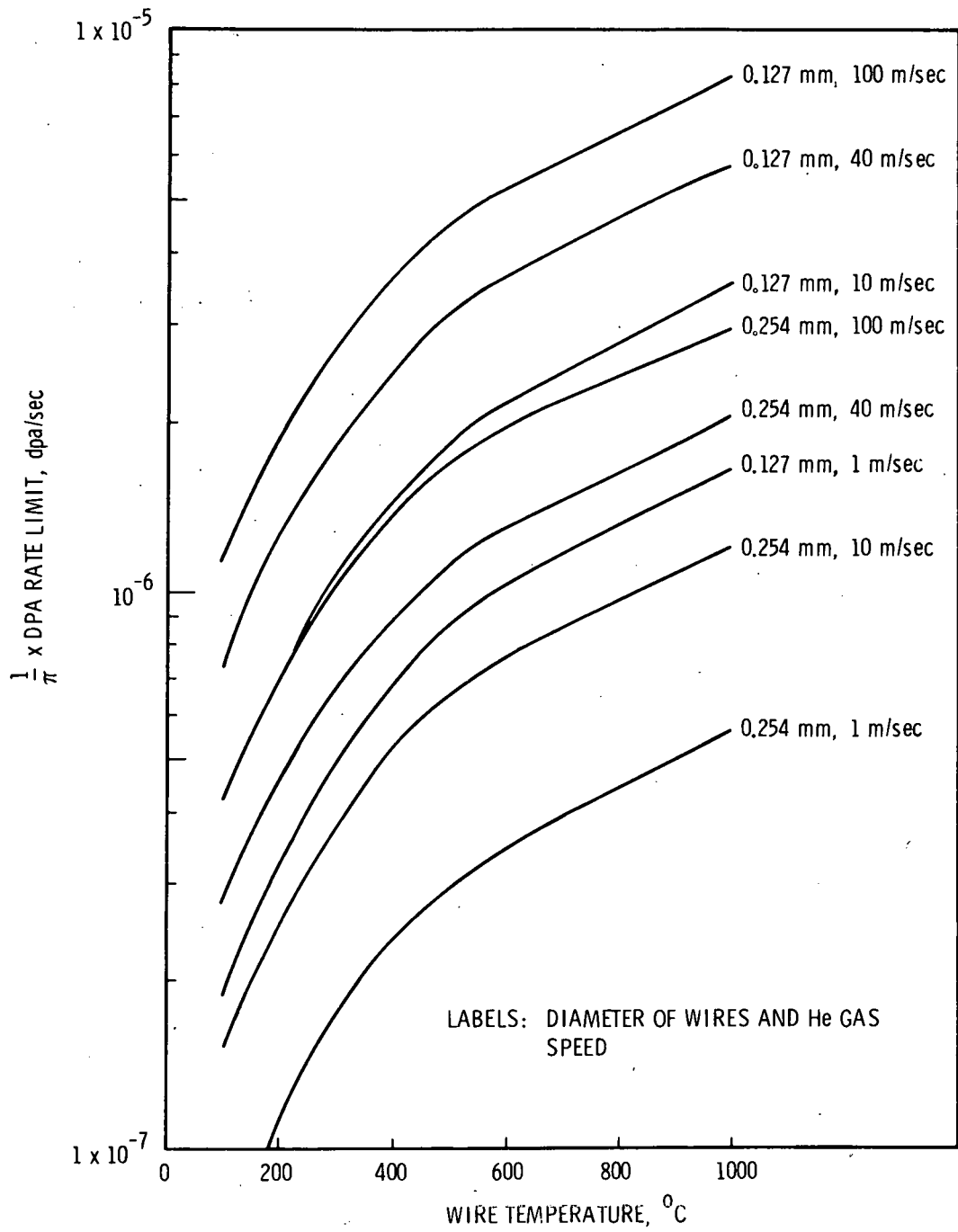
FIGURE 25. Calculated Maximum DPA Rates in He-Cooled Nb Wires
Subjected to 16 MeV Deutrerons
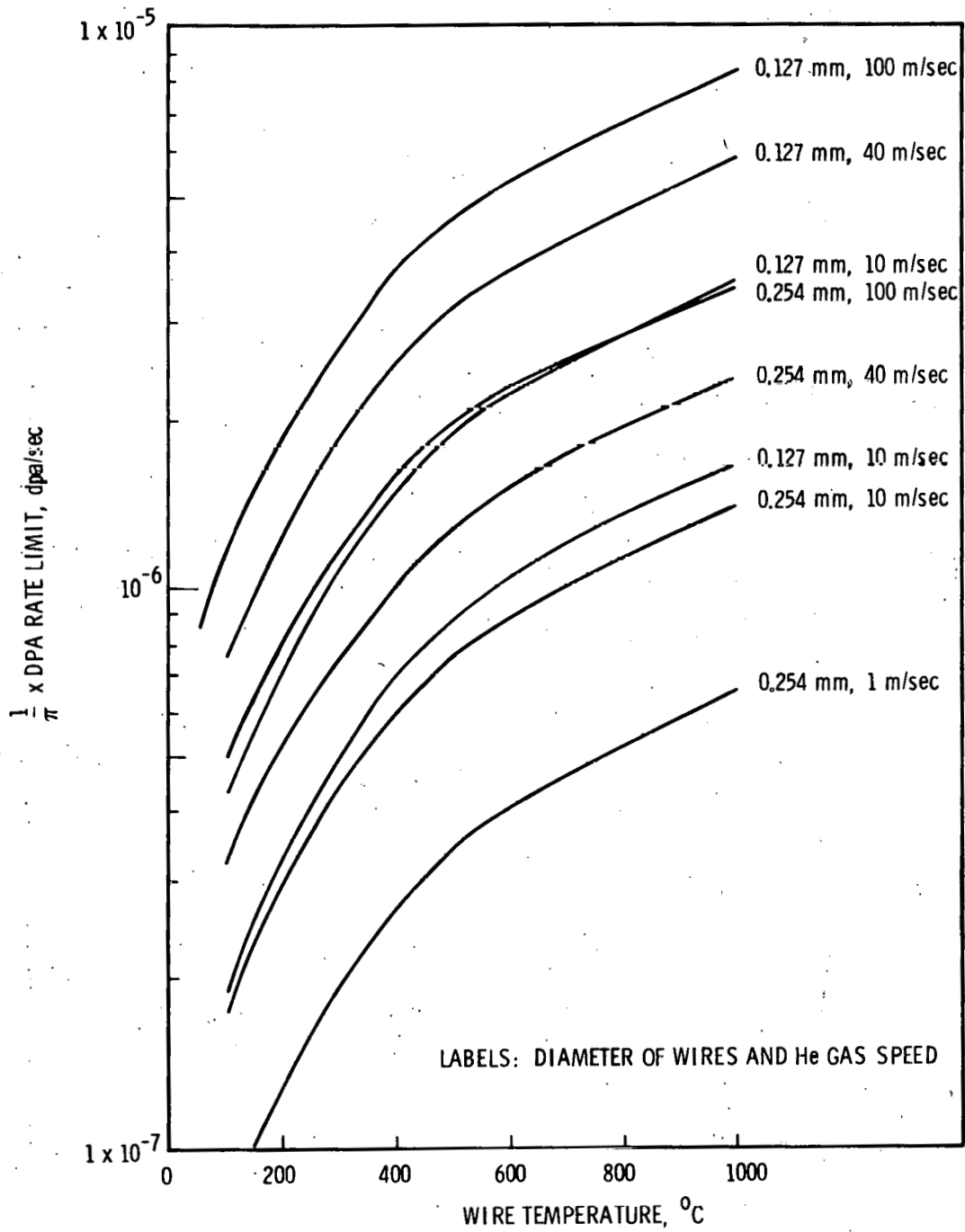
FIGURE 26. Calculated Maximum DPA Rates in He-Cooled Nb Wires
         Subjected to 40 MeV Alphas

64

For 40 MeV alphas, 0.125 mm radius wires are limited to dpa rates several percent below that produced by deuterons for the same temperatures and gas speed. On the other hand, if this radius is doubled the limiting dpa rates are several percent greater than those calculated for deuterons on the same size wire with similar cooling. Such an inversion in the magnitude of the differences between deuteron and alpha induced dpa limits is brought about by a relatively large increase in the average displacement cross-section when the 0.125 mm wire radius is doubled. For deuterons this increase is about 32 percent; for alphas it is 54 percent. Maximum dpa rate occurs for the smaller radius wire; at 500°C this is about 4.8×10^{-6} dpa/sec.

Suppose that, instead of a wire, a foil of thickness L is broadside to an ion beam and that helium gas coolant flows parallel to the foil surfaces. In this case an analysis similar to that made for wires can be used to calculate limiting dpa rates. The difference is in the flow patterns over foils versus wires. Assuming a turbulent flow and using the results of Hopf[63] and Colburn[64] for a heat transfer coefficient, as suggested by Jacob and Hawkins,[65] the expression for the limiting current density can be expressed as

$$ J = \frac{0.072 \; k\rho C_p \; U(T_a - T_g)}{2\gamma E \; [0.072 \; \rho C_p \; UL + 8k(R_e)^{1/5}(P_r)^{2/3}]} $$

where ρ is the mass density of the gas, C_p is the specific heat, P_r is the Prandtl number, and U is the gas speed.

The above expression for the limiting ion current density on a foil should not be expected to give any better than order of magnitude accuracy. Extent of turbulence and the variation of $(T_a - T_g)$ as the gas moves along the foil surface will significantly influence the result. Nevertheless the calculation is useful for comparison with estimates made for gas cooled wires. The resulting limiting dpa value isotherms are shown in figure 27. The value for T_g was assumed to be constant and equal to the average between that of the foil and the temperature of the gas at a large distance from the foil. Values of k and k_g used were those at the temperatures of the foil and the viscous film (at the foil surface), respectively. The Prandtl number
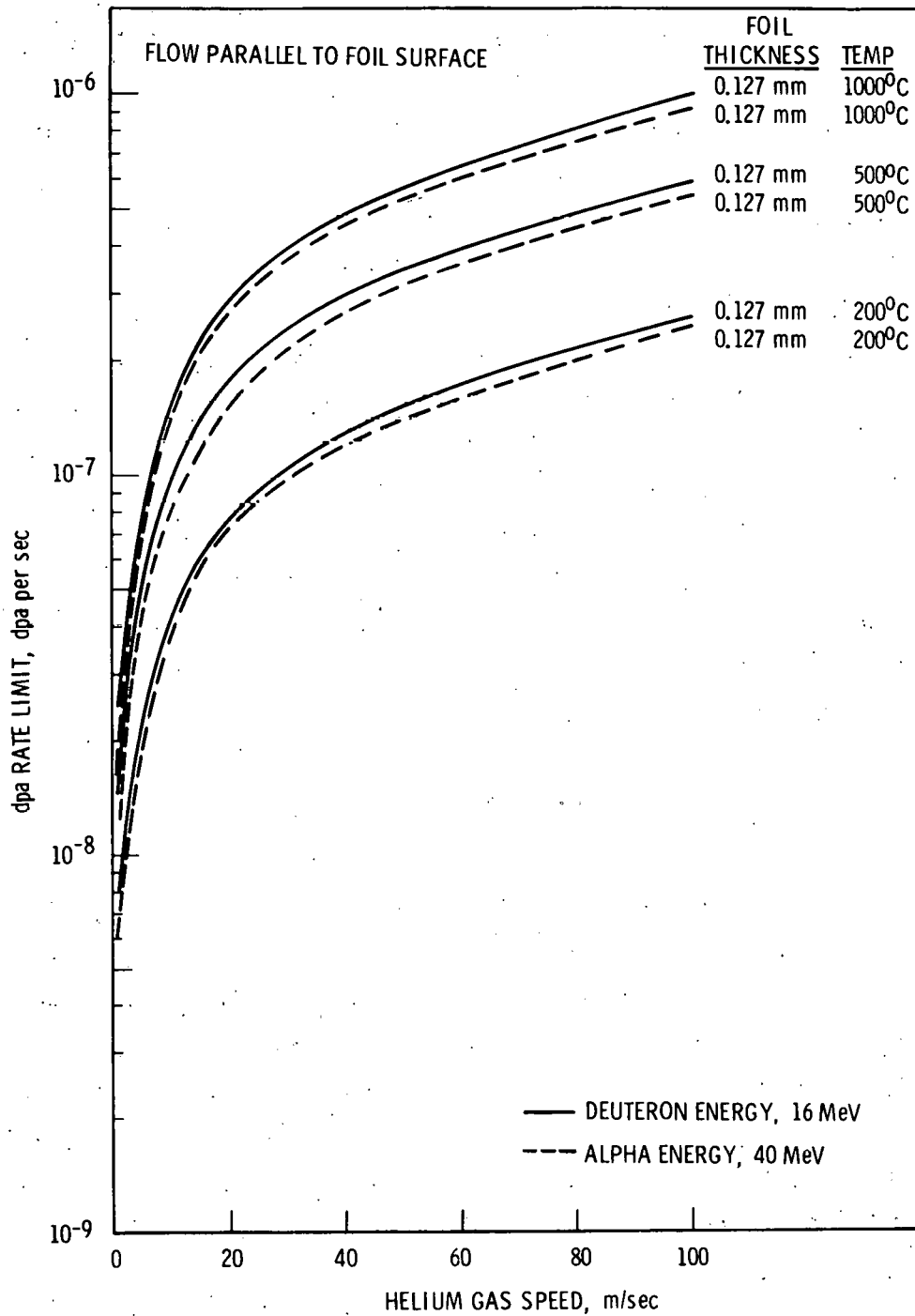
FIGURE 27. Calculated DPA Rate Limit Isotherms for d and α on Ni Foils

was determined by using viscosity values calculated from the kinematic viscosities given by Boelter, et al.[66] The results show dpa limits for 0.127 mm thick foils are about one order of magnitude smaller than the limits determined for 0.127 mm diameter wires. Comparison of coolant isokinetic curves of the foil (figure 28) with those of larger wire diameters (0.25 mm) shows the foil cooled with 100 m/sec turbulent helium gas has dpa limits similar to those of a 0.25 mm diameter wire cooled by 10 m/sec helium gas.

The above calculation for foils neglected the radiation and end effects. This is a valid approximation for small foils having areas of a few square centimeters in the temperature and He gas speed ranges investigated.

It is concluded from the above simple analyses, for the dimensions, ion energies and gas flow ranges examined, that differences in flow characteristics over wires and foils are likely to produce order of magnitude differences between dpa rate limits in Ni wire and foil, and that Ni wires of radius (a) are better suited than Ni foils of thickness L = 2a in being able to sustain a higher dpa rate at a given temperature. It is emphasized that this is the case only if the targets in question do not sample the highly non-linear portion of the displacement cross-section profile. Higher ion energies will allow use of thicker targets but rate of thermal energy extraction is decreased which decreases the maximum possible dpa rate.
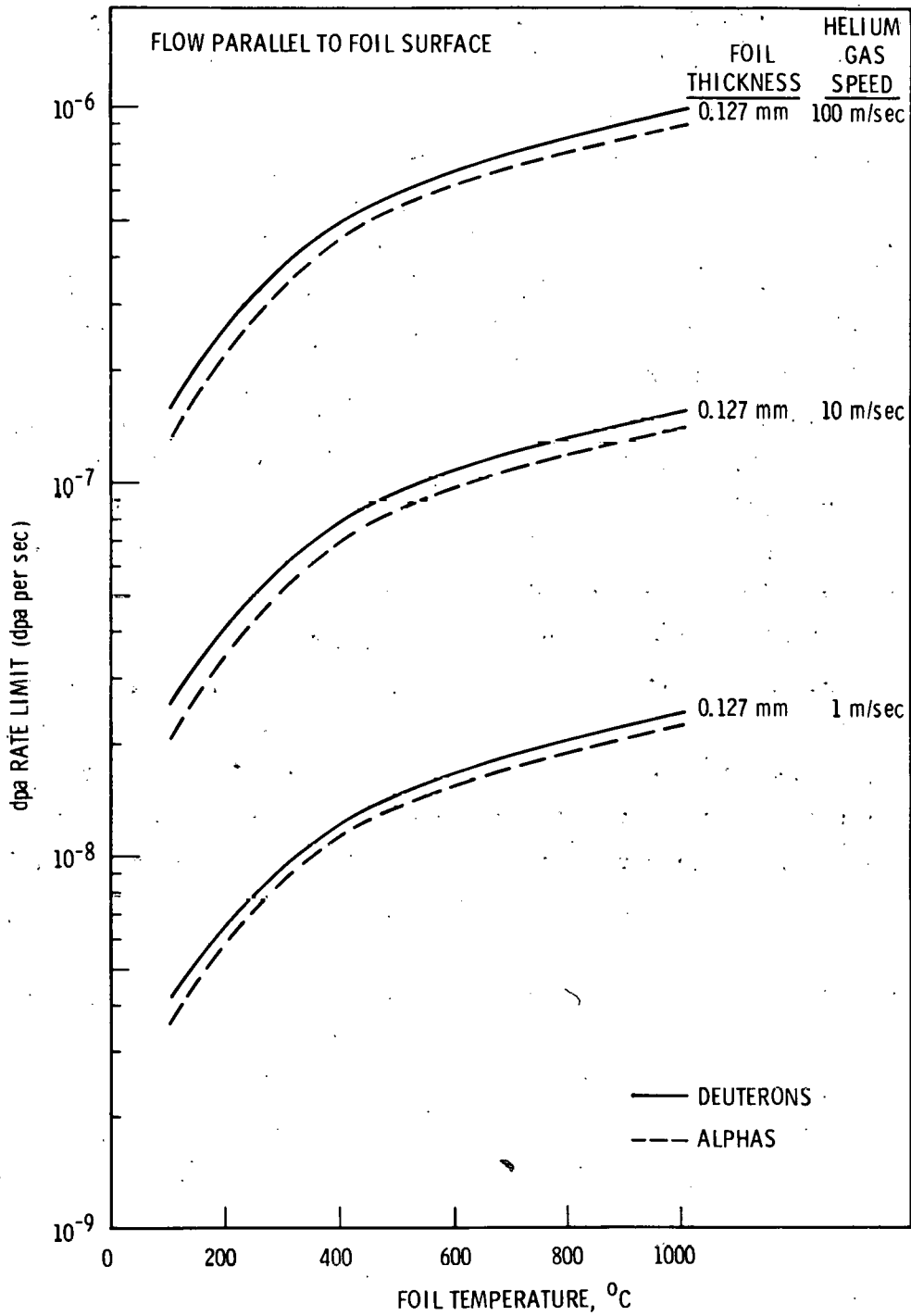
FIGURE 28. Calculated DPA Rate Limits for He Cooled Foils
Subjected to 16 MeV Deuterons and 40 MeV Alphas

VI. Specimen Size and Surface Effects on Mechanical Properties

The boundary between a solid metal and its environment is a physical discontinuity which can have pronounced effects on the mechanical properties of that metal. Alterations to the physical or chemical state of this boundary as in the case of the Roscoe effect, i.e. a surface oxide or coating, or of the Rehbinder effect, i.e. a surface active liquid have an increasingly pronounced effect on the properties of metals as the surface area/volume ratio increases. The Roscoe and Rehbinder effects can be classified as extrinsic while intrinsic effects arise from near surface dislocation dynamics and surface energy considerations which contribute to surface drag forces.

Size dependent mechanical properties can be attributed to three factors: 1) surfaces, 2) grip effects, and 3) crystal dimensions which are related to dislocation mean free paths and thickness/grain size effects. It is the purpose of this section to review each of these contributions to mechanical property behavior with application made to the surface and specimen geometry considerations for ion irradiation of metals for mechanical property studies.

Specimen size limits are set primarily by the penetration depth of the bombarding ion since complete penetration of the test sample is desireable. With high z ions, sample dimensions of a few μm in the beam direction are required while this dimension may be 100 to 200 μm with low z ions. Removal of the beam energy deposited within the sample in the form of heat could limit the sample thickness more than the penetration depth depending on beam energy and current. A lower limit on sample dimensions may be imposed by the need to relate the ion beam irradiated data to bulk behavior and also by handling considerations.

A. Surface Effects on Crystal Plasticity

1. Intrinsic Surface Effects

Dislocations near a hypothetically clean surface are influenced by two forces of sufficient magnitude to warrant

69

discussion. These forces are classified as surface energy and image forces. The surface energy force is derived from the surface step which results when a dislocation has a component of its Burgers vector perpendicular to the surface. A stationary dislocation very near the surface may experience an attractive or repulsive force depending on the step energy relative to the dislocation strain energy. An attractive force results from the decrease in the strain energy of the system as a dislocation approaches a free surface while the work of creating new surface acts to repel a dislocation.

The thermodynamic system composed of the solid and its environment undergoes a change in the Helmholtz free energy ΔG when a new surface is introduced in the solid. This energy change results from the mechanical work $\Delta w = \gamma \Delta A$, where γ is the specific surface work and ΔA is the area of the new surface, and the chemical work which is the sum $\sum_i \mu_i \Delta N_i$, where μ_i is the chemical potential of the i th adsorbed species and N_i is the quantity of material transferred to this new surface.

The specific surface work then equals:

$$\gamma = \frac{\Delta G}{\Delta A} - \sum_i \mu_i C_i \tag{1}$$

where $\frac{\Delta G}{\Delta A}$ is the specific surface free energy and C_i is surface concentration of the ith adsorbant. The surface work is reduced by chemical potential. An example is the reaction of air with all metals except gold to form a surface oxide.

A virtual force is exerted on a dislocation as it approaches an ideally clean surface. This attractive force results from a lowering of the free energy of the system as the strain energy associated with the dislocation is decreased by the approach to the surface. The term image force has been applied to this virtual force because the attractive force may be accounted for by an imaginary dislocation which is a mirror image of the real dislocation.

Consider a screw dislocation, s, in a solid near a free surface, as shown in Fig. 29. The stress at the plane x = 0 from the screw dislocation located at -x is:

$$\sigma_{xz} = \frac{\mu b y}{2\pi x^2 + y^2} \qquad (2)$$

This shear stress acts in the Z direction on a plane perpendicular to the x direction with a force applied in the x direction to a screw dislocation lying in the z direction. The shear stress $\sigma_{yz} = -\frac{\mu b}{2\pi} \frac{x}{x^2 + y^2}$ must vanish at the plane x = 0 because a free surface cannot support tangential shear stresses. The imaginary dislocation s' is necessary to satisfy the boundary conditions. A stress at the plane x = 0 from the screw dislocation s' is:

$$\sigma_{xz} = \frac{-\mu b y}{2\pi x^2 + y^2} \qquad (3)$$

The above solution for the stress field of a dislocation nearing a free surface is a special case where the elastic constants of the two materials are equal. In general the elastic properties of the two materials will differ. A dislocation approaching a material of greater elastic moduli will be repulsed by the increase in the strain energy of the system as its strain field enters this material. An attractive force results from the decrease in the strain energy of the system for a material with smaller elastic moduli. Further comment on the effect of surface coatings and reaction products is deferred to the section on extrinsic surface effects.

A drag force is also exerted on a moving dislocation by the presence of a free surface. This drag force results from the surface step area produced by a moving dislocation which intersects a surface and has a compenent of its Burgers vector
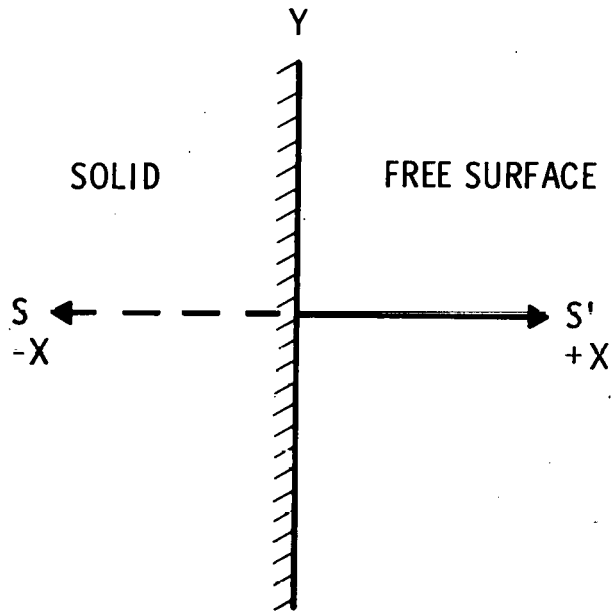
Figure 29. Schematic of a Screw Dislocation Near a Free Surface With Its Image Dislocation. The Z Direction is Normal to the Plane of the Paper.

perpendicular to the surface. The shear stress necessary to move a dislocation against this drag force is a function of the specific surface work, γ, and the dislocation line length, L. The form of this relation is as follows:

$$\tau = \frac{2\gamma}{L} \tag{4}$$

For large crystals, L is large and therefore the drag force is negligible; while a dislocation in a crystal 2000A thick would be pinned by a stress of roughly 10^9 dynes/cm^2. The drag force from surface energy considerations can only be reduced by surface reactions which reduce γ, such as oxide formation; however, the total drag force may be increased by the formation of an oxide when the image force is also considered.

The formation of a high dislocation density near the surfaces of metals deformed a few percent has been explained by the favorable energetics for dislocation multiplication near a free surface. Fisher[67] postulated that a Frank-Read source near a free surface can be thought of as pinned to a point outside the crystal at one end and within the crystal at the other end of the semi-circular dislocation loop. The exterior point is a mirror image of the interior point with the effective dislocation length equal to twice its actual length. The critical stress for generating half loops at the surface is then $\tau_s^* = \frac{Gb}{(L_s + L_I)}$ where $L_s + L_I = 2L$. Fisher's approach assumes that the distribution of interior pinning point spacings L are equal to the distribution of their spacing from the surface, L_s. This may be an incorrect assumption for materials which have a chemical concentration profile near the surface. This profile need only exist over a distance equal to the internal pinning separation, L. Values of L equal to 1000 - 2000 Å are not uncommon.

A multiple cross-glide mechanism for dislocation multiplication at free surfaces of crystalline materials has been proposed by Johnson and Gilman[68] A schematic, illustrating

73

three phases of this mechanism, is shown in Fig. 30, where a screw dislocation, AB, with Burgers vector, b, lies on a glide plane, ABCD, inclined to the surface at an angle θ. The dislocation can shorten its length and therefore its energy by moving off its primary glide plane, as indicated in Fig. 30-b. The creation of a surface step opposes this motion. Dislocation multiplication results from the cross-gliding operation because two primary slip planes are now active, i.e. Koehler source, as demonstrated in Fig. 30-c. The dislocation now contains a sessile edge component or a jog which imposes a drag force on the dislocation. As the two glissile or mobile segments of the screw dislocation move they will trail a dislocation dipole which cannot easily escape to the free surface. The presence of a high concentration of edge dislocation dipoles near the free surfaces of partially fatigued aluminum has been reported by Grosskreutz and Benson.[69]

The cross-glide mechanism is particularly sensitive to the surface energy because the shear stresses around the screw dislocation are relaxed at the free surface so the dislocation line has only the core energy. The magnitude of the core energy is comparable to the surface energy, so that surface energy changes are expected to influence the cross-glide mechanism.

The presence of a high concentration of dislocations near the free surface following cyclic deformation has been observed by transmission electron microscopy, but has also been demonstrated by Feng and Kramer,[70] the effect on the yield strength of removing, by electropolishing, 100 μm from the surface. A back stress, σ_s, is assigned to this high dislocation density layer, or "debris layer", which is equal to Δσ. The Δσ is the difference in the stress to which the sample was strained prior to unloading and electropolishing and the yield strength on reloading, as illustrated in Fig. 31. The yield strength upon reloading is equal to that for virgin material. A dislocation near this surface layer experiences a net stress of $\sigma_{net} = \sigma_a - \sigma_i - \sigma_s$ where σ_a is the applied stress and σ_i is an internal resistive stress. For bcc iron, deformed at -20°C, the surface stress is about 60% of the net plastic stress up to strains of 0.20.
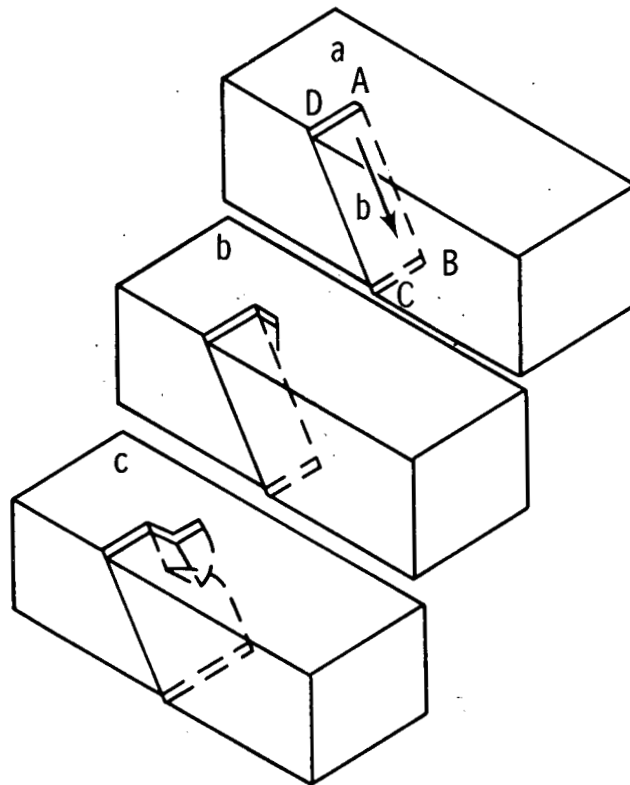
Figure 30. Cross-Glide Mechanism For Dislocation Multi-
plication Near a Free Surface (After Johnston
and Gilman[68])
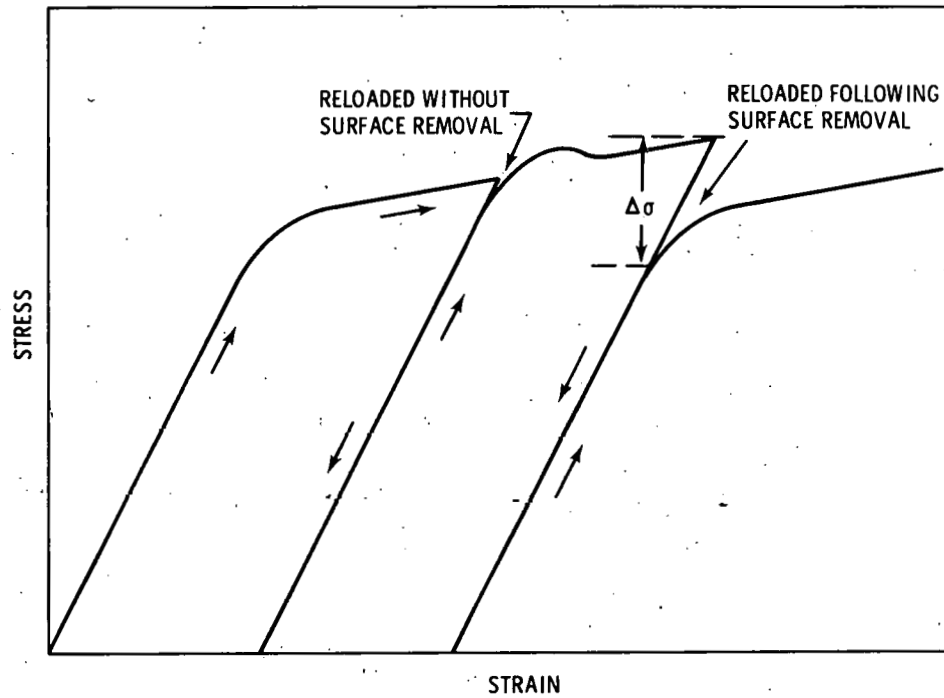
Figure 31. Schematic Illustration of the Effect on the Tensile Properties of Removing the Surface Layer

Recovery of this surface layer has been observed in 4 hours at $25^\circ C$ for aluminum[71] and 2 hours at $150^\circ C$ for gold. The removal of the surface layer continuously during tensile deformation lowered the ductile to brittle transition temperature of molybdenum approximately $15^\circ C$.[72]

When metal single crystals were deformed in an electrolytic polishing bath to continuously remove the surface layer, the extent of Stage I and II increased and the work hardening decreased.[73] The extent of Stage I slip in aluminum single crystals was doubled for a removal rate of 2.1×10^{-5} cm/s while the Stage I work hardening rate was more than halved. The extent of Stage II slip was increased by a factor of 1.5 while the Stage II work hardening rate was reduced by a factor of 4. The strain rate of the test was 10^{-5} s^{-1}. The apparent activation energy and volume for plastic deformation was also affected, with the activation energy being decreased by a factor of 4 and the activation volume by a factor of 5, at a removal rate of 2.1×10^{-5} cm/s.

In summary, the mechanical properties of both fcc and bcc metals are affected by the removal of the surface layer. Similar behavior in two phase, age-hardened alloys was not observed by Feng and Kramer,[70] although other surface effects such as surface energy and image forces are expected to have an influence. Some controversy exists as to the existence of a surface "debris layer". Swann[74] examined the dislocation distribution near the surface of deformed copper and concluded the near surface dislocation distribution did not differ significantly from the bulk. However, Kramer and Haehner[75] noted that the large plastic strains (15%) at which the copper crystals were studied by Swann accounted for this observation. The surface "debris layer" forms at low strains (< 5%) with bulk dislocation motion and multiplication following.

2. Extrinsic Surface Effects

The tensile stress-strain behavior of metals with surface films and surface active liquids is illustrated[76] in Fig. 32. The surface film effect was first observed by Roscoe[77] in 1934 when he found that an oxide film of less than 20 atoms thick on a bulk cadmium sample was sufficient to raise the yield stress 50% while a 100% increase occurred for an oxide film 1200 atoms thick. Later work by Cottrell and Gibbons[78] confirmed these results on cadmium while Harper and Cottrell[79] obtained similar results on zinc, and Takamura[80] found a similar result for aluminum. A very clever experiment was performed by M. R. Pickus and E. R. Parker[81] where they performed a creep test on zinc crystals in a copper electroplating solution. The strain rate was reversibly altered by plating and de-plating a 1.25 cm dia. zinc crystal with copper. The creep rate in the copper plated condition was nearly a factor of ten less than the unplated at $200^{o}C$.

Rehbinder[82] and Rehbinder and Wenstrom[83] were the first to observe that the creep rate of lead, tin and copper sheets was greater if small amounts of surface-active agents (cetyl alcohol, n-valeric, n-heptoic, stearic, oleic, palmitic and cerotic acids) were added to the paraffin oil bath in which the samples were immersed. Controversy concerning the surface active agents and mechanisms involved in the Rehbinder effect still exists; however, further comment on this surface effect will not be made because of its lack of relevance to the probable surface conditions which will be encountered in ion beam irradiation experiments.

Oxide or carbide film growth on small samples during ion beam irradiation is a likely reaction which must be considered because surface effects are magnified at small sample sizes. A surface coating can affect near surface dislocation mobility through the image force imposed by the elastic modulii difference between coating and substrate. In simplest terms, a dislocation senses the presence of a high modulus coating because the strain energy of the system is increased as the strain field of the dislocation enters the coating.
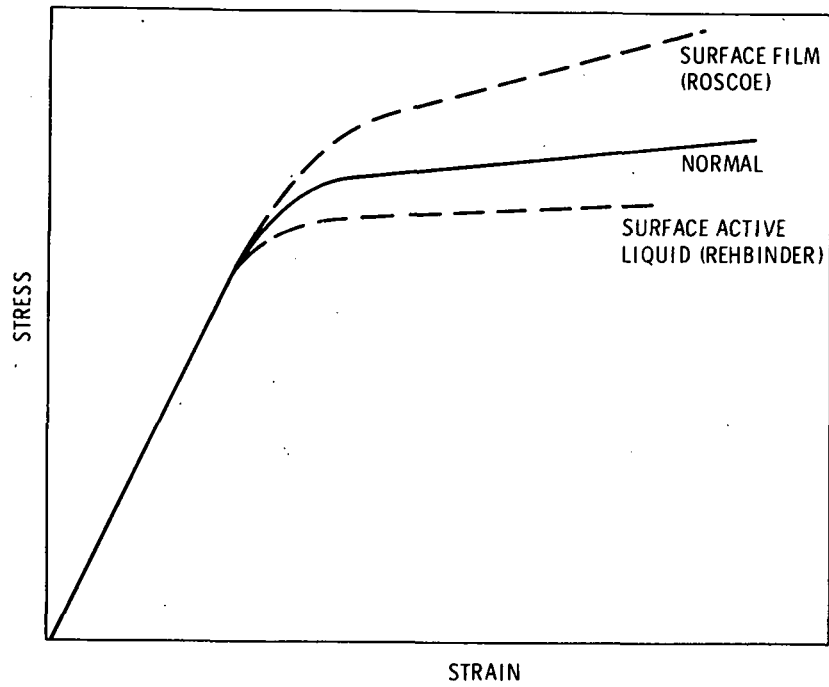
Figure 32.   Schematic Illustration of Two Extrinsic Surface
             Effects on the Tensile Properties of Metals
             (After J. J. Gilman[76])

A detailed analysis has been performed for screw dislocations by Head[84] where he showed that a film whose shear modulus is greater than the substrate will exert a long range attraction and a short range repulsion. For an edge dislocation which lies parallel to the surface on a glide plane perpendicular to the surface, Conners[85] obtained the following expressions:

$$F = \frac{bD}{2(h + t)} \left(1 - \beta^2 \{K_1 + \frac{h}{h+t} K_2\}\right) \qquad (5)$$

where
- b - burgers vector
- h = coating thickness
- t = dislocation distance below the surface
- $D = \frac{Gb}{2\pi(1-\nu)}$
- G = shear modulus of substrate
- $\beta = \frac{E_c}{E_s + E_c}$
- E_c = Young's modulus of coating
- E_s = Young's modulus of substrate
- $K_1 = (1-\nu)\left(\frac{1}{1-2\nu} + \frac{1}{2-\nu}\right)$
- $K_2 = \frac{1-\nu}{4}\left(\frac{2+4\nu}{1-2\nu} - \frac{1}{2-\nu}\right)$
- ν = Poissons ratio which is assumed equal in the coating and substrate.

Grosskreutz[86] used this relationship to show that an edge dislocation is attracted to the surface when $\beta<0.5$, trapped at some distance beneath the surface for $0.5\leq\beta\leq0.646$ and repulsed for $\beta>0.646$. A trapped or repulsed dislocation would move toward the surface with an increase of the applied shear stress. As the dislocation approaches to within a few angstroms of the oxide-substrate interface with an increasing shear stress, a slip step may form by fracture of the oxide or shear between the oxide and substrate. The work to produce this slip step is in addition to the work done against the image force and may be called an oxide film strength effect. An earlier comment about an oxide film aiding the formation of a slip step

by lowering the surface energy is applicable only if the oxide is sufficiently thin or weak such that the work required to fracture the oxide is very small. The presence of adsorbed atoms satisfies this criteria.

3. Environmental Effects

Since the nature of the free surface and chemistry of the near surface are controlled by the environment, they should be discussed as an intrinsic or extrinsic surface effect; however, a considerable amount of data exists for tests performed in various environments where the surface was not thoroughly analyzed. Therefore, a few comments about the mechanical properties of metals tested in vacuum and gas atmospheres is appropriate.

The fatigue life as a function of the environment has been the most thoroughly investigated mechanical property where a continuous increase in the fatigue life of copper, as measured by the number of cycles to failure, N_f, was found by Wadsworth[87] for decreasing atmospheric pressures. The fatigue life increased from 5×10^5 cycles at 760 torr to 10^7 cycles at 10^{-5} torr. A discontinuous change in the fatigue life of lead was found by Snowden[88] where no change occurred from a pressure of 10^3 to 10^{-1} torr but an increase from 4×10^5 cycles to 2×10^7 cycles occurred for a cyclic strain of 0.00075 over the pressure range of 10^{-1} to 10^{-2} torr. The fatigue life remained constant at 2×10^7 cycles to a pressure of 10^{-6} torr. The environmental effects on fatigue life are also dependent on the stress and strain amplitude and cyclic frequency.

Environmental dependence of fatigue life is thought to control the crack propagation rate by the presence or absence of reactive gas species at the crack tip. The mechanisms occuring at the crack tip have not been investigated in any detail; however, the reactive gas concept is reasonably consistent with the results from various material-environment

combinations. These include the lack of an environmental effect on the fatigue life of gold and the increased fatigue life of various metals in inert atmospheres.

Environmental effects on creep and stress-to-rupture have also been found. Shahanian and Achter[89] found the creep rate of nickel to be highest in a nitrogen atmosphere and lowest in vacuum while the creep rate in air and a helium-2% oxygen mixture were intermediate. Their results are shown in Fig. 33. The authors proposed that nitrogen facilitated crack propagation by reacting with grain boundary impurities.

A difference in the minimum creep rate of a Ni-6%W alloys when tested in a vacuum of 10^{-5} torr and argon atmospheres was found to be grain size dependent by Johnson, et. al.[90] as shown in Fig. 34. The grain size at which an environment effect was found corresponded to 8 grains across the thinnest direction of the gauge section. Grain boundary cavitation was more pronounced in samples with grain sizes larger than 0.15 mm and tested in argon than those tested in vacuum. The commerical purity argon was found to contain P_{O_2} = 7.6 x 10^{-4} torr, $P_{N_2} \simeq$ 15 x 10^{-4} torr and $P_{H_2O} \leq 7.6$ x 10^{-4} torr while the vacuum of 10^{-5} torr had P_{O_2} = 1.9 x 10^{-6} torr, $P_{N_2} \simeq$ 7.6 x 10^{-6} torr, P_{H_2O} <7.6 x 10^{-8} torr. The nitrogen and oxygen concentrations in the argon may be causing a similar reaction to that proposed by Shahanian and Achter[89] however, Johnson, et. a[90] did not feel their results supported a conclusion about the mechanisms involved.

Environment sensitive mechanical properties which depend on a chemical reaction between a gas species in the environment and the sample would be time dependent and therefore not be significant in a high strain rate test such as a tensile test. However, the work hardening rate of polycrystalline high purity aluminum wire (0.051 cm) was altered when tested in a vacuum of 8 x 10^{-7} torr as compared to 760 torr. The results of this study are shown in Fig. 35. The increased work hardening rate with ion etching may have resulted from
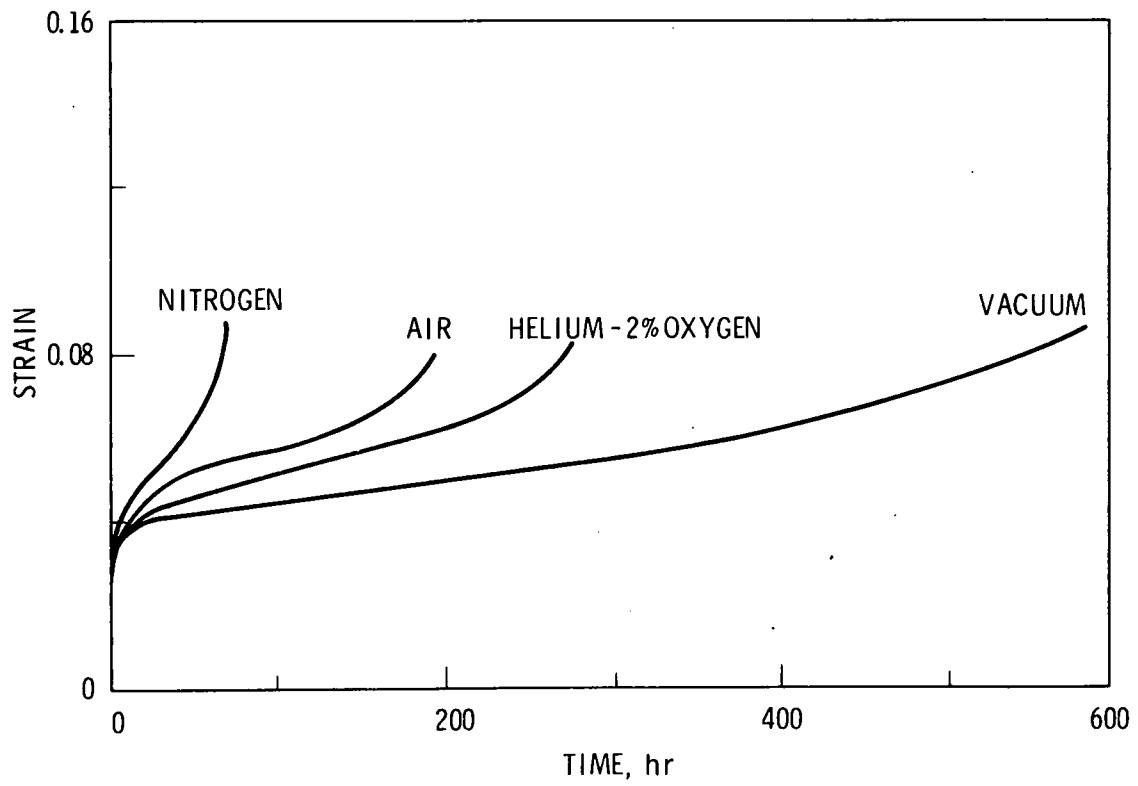
Figure 33.   Creep of Nickel (99.8%) In Various Environments
at 482°C and a Stress of 210 MPa (30,000 psi)
(After Shahanian and Achter[89])
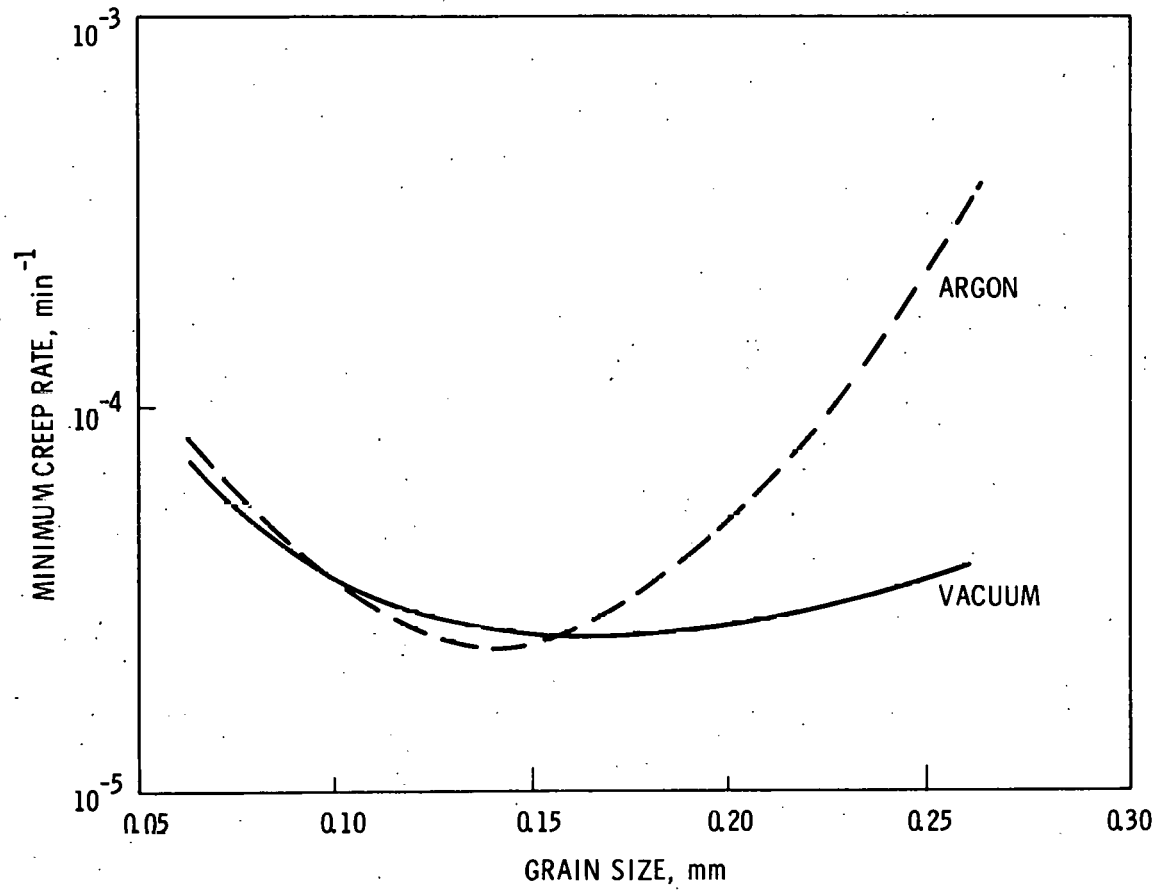
Figure 34. Creep Rate Versus Grain Size and Environment
            For Ni-6%W at 900°C and 35 MPa (5000 psi)
            (After Johnson et.al.[90])
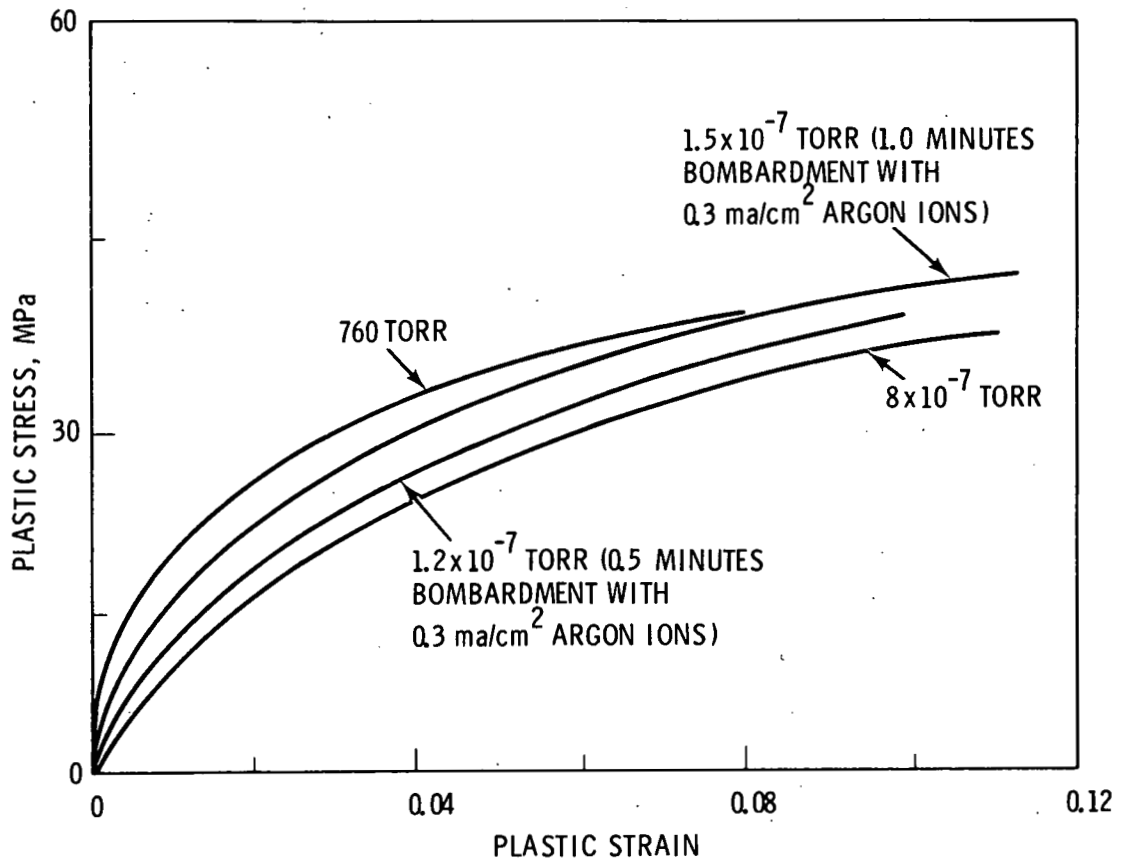
Figure 35. Stress-Strain Behavior of Polycrystalline High
Purity Aluminum Wire (.008 cm) in Various
Atmospheres. (After Kramer and Podlaseck[91])

the near surface damage caused by irradiation with argon ions or their entrapment near the surface.

The lowered work hardening rate observed by Kramer and Podlaseck[91] may not be attributable to an oxide film strengthening or image force effect if the aluminum oxide flim properties measured by Grosskreutz[86] in vacuum are similar to the in-situ oxide on the aluminum wire. The results obtained by Grosskreutz for the tensile strength and Young's modulus of aluminum oxide in air and vacuum are shown in Figs. 36 and 37. Removal of absorbed water vapor from the oxide under vacuum conditions was the proposed mechanism for the modulus increase.

4. Surface Considerations in Ion Bombardment for Mechanical Property Studies

The small test samples required for ion irradiation studies must not only simulate unirradiated bulk behavior, but also irradiated bulk behavior. This means that surface, grain boundary and volume reactions which may occur during irradiation must not dominate the mechanical behavior of these samples. Surface contamination can occur from a number of sources such as: 1) sample preparation; 2) sample impurities; 3) irradiation environment; 4) impurities carried with the ion beam, and 5) test environment (post tests).

The annealing vacuum, cleaning procedures and handling methods are the prime sources of surface contamination during sample preparation. Contamination from these sources can be minimized but not totally eliminated. A surface cleaning operation conducted within the irradiation or test chambers prior to testing may overcome this source of contamination; however, this extra effort can only be justified if contamination from other sources is small. In-situ surface cleaning may be accomplished by an elevated temperature bake-out and/or by ion sputtering. Surface active impurities within the sample can be a source of surface contamination. An example is sulfur
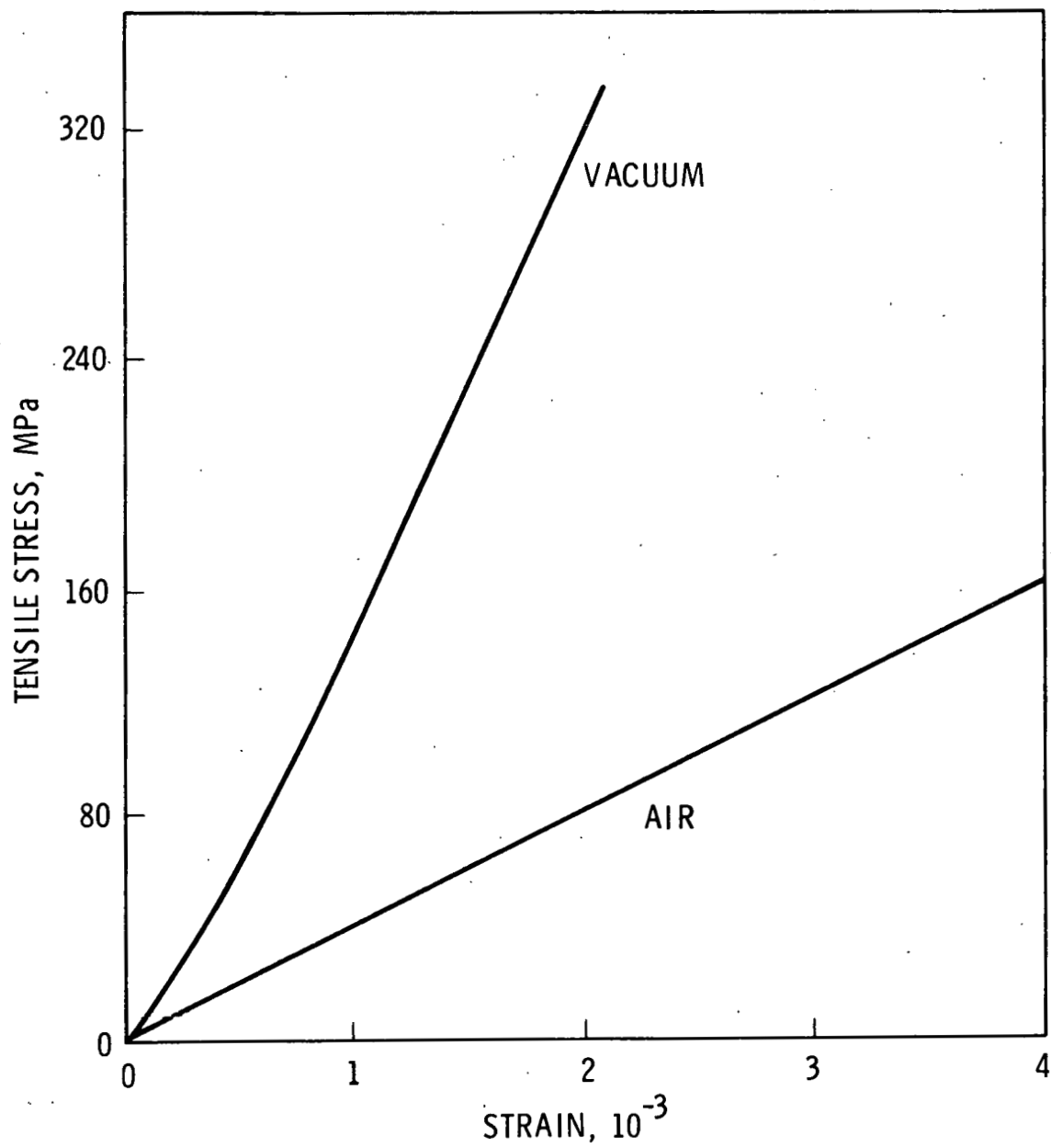
Figure 36.   Typical Stress Versus Strain Relationship For
3000 Å Thick Anodic Films in Air and Vacuum
(10^{-6} Torr) (After Grosskreutz[86])
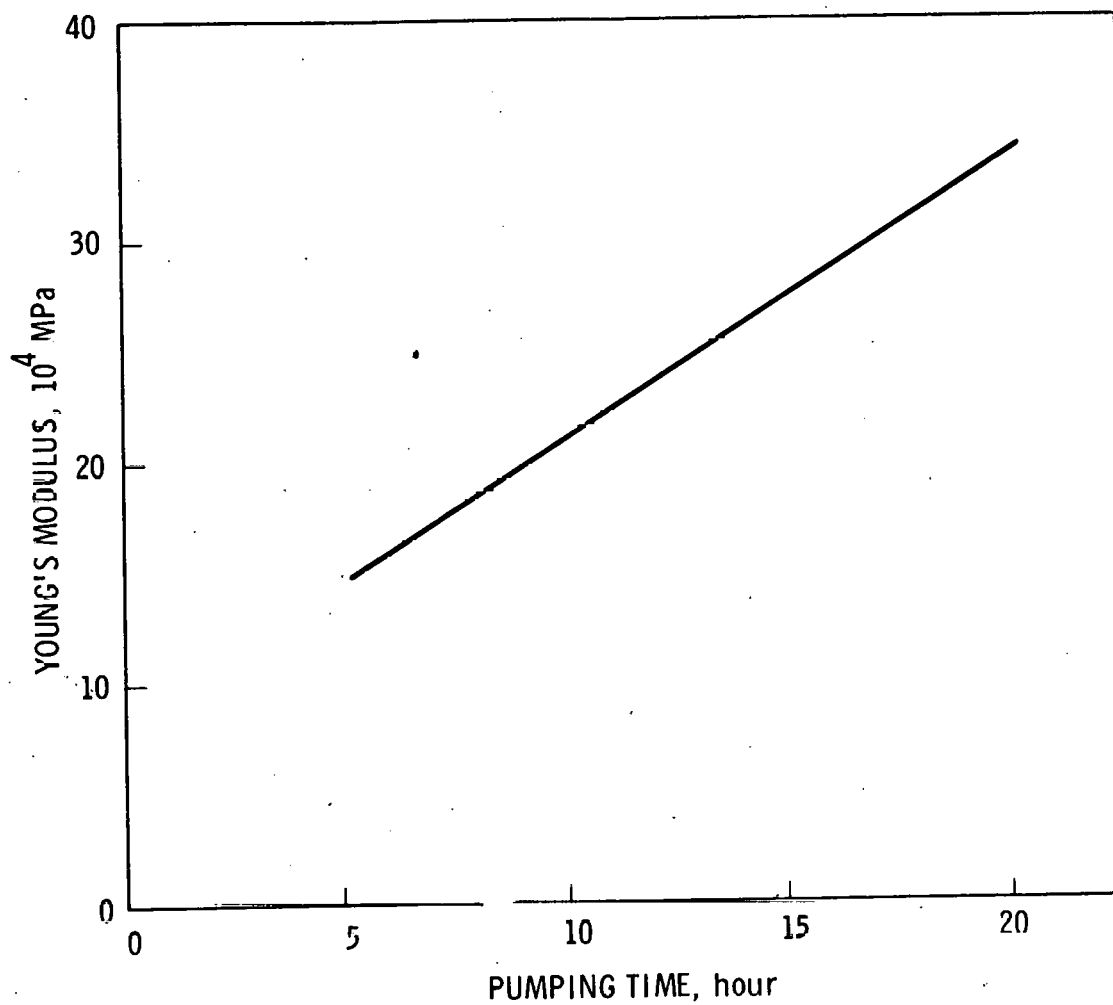
Figure 37. Young's Modulus Versus Pumping Time For Anodic Films (After Grosskreutz[86])

in nickel. Contamination can result from impurity gases remaining in the vacuum chamber after pump down, and impurities in the helium cooling gas while the ion beam can be the source of hydrocarbons which are desorbed from the beam line walls. The latter contamination can be eliminated by using a thin window to separate the irradiation chamber from the beam.

The effect of these contaminants will be to alter the surface energy, form oxide, nitride or carbide films and possibly alter the sample chemistry. Grain boundary diffusion and precipitation is also very likely and could easily dominate the mechanical behavior more than surface contamination.

Ideally, an atomically clean surface should be maintained throughout the irradiation experiment. Such a surface would facilitate comparisons between the mechanical properties of a material irradiated in more than one apparatus and by more than one damaging species. However, such a surface is atypical of engineering materials and the measured properties may be unsuitable for engineering application. In reality, some level of surface contamination must be tolerated; however, it is hoped that this level can be maintained sufficiently low that the surface does not dominate the sample properties.

Changes in the surface energy and chemistry can affect the strength of a material by a number of mechanisms. The strengthening effects of four possible surface dependent mechanisms have been calculated from existing models with the resulting values listed in Table IX. While the calculated strengthening effects may not be accurate in an absolute sense, they are useful for comparison. The results of these calculations indicate that image forces on near surface dislocations will be the most significant surface effect.

The contribution of the surface energy to the strength of a sample can be made with the following equation:

$$W_o = \pi r \left(\gamma_s - \gamma_{gb} \frac{r}{d} \right) \tag{6}$$

89

TABLE IX

Summary of Some Surface Strengthening Effects cn Small Samples

Strengthening Effect	Mechanism	Morphology		Shear Strength Contribution, MPa*	Comments
Surface Energy	Surface tension opposes tensile load in creep	Sample diameter ~125 μm		0.034	Value calculated from W_o of 41.5 mg at 1370°C. Assume $\gamma_s - \gamma_{gb} \neq f(T)$.
Surface Pinning	Energy to create surface step pins dislocation	Sample thicknesses 10 μm 100 μm		0.48 0.048	$\delta_{NI} \approx 3000$ ergs/cm^2 at 600°C.
Surface Film	Image force	Film 0.01 μm 0.10 μm	Sample 100 μm 100 μm	1.38 0.138	$\dfrac{E_c}{E_s} = 5$
Surface Film	Tensile failure	Film 0.01 μm 0.10 μm	Sample 100 m 100 m	.007 .07	Al_2O_3 oxide film used for calculations because of available data.

* 1 MPa = 145 $\dfrac{lb}{in^2}$

where W_0 is the zero creep load, r is the radius of the sample, γ_s is the surface tension, γ_{gb} is the grain boundary surface tension and d is the average grain length. Experimentally, W is determined with a creep test where loads less than W result in a negative strain and loads greater than W result in a positive strain. The value for the surface energy contribution at $550^{\circ}C$ listed in Table IX was obtained from the zero creep load for 0.0127 cm diameter nickel at $1370^{\circ}C$ of 41.5 mg obtained by Roth[92] with the assumption that the difference in γ_s and γ_{gb} is independent of temperature.

The surface pinning contribution was calculated using equation 4 with L as the sample thickness. The image force on near surface dislocations caused by an oxide film were determined with equation 5 and assuming the elastic modulus of the film is five times greater than for the metal. Since the image forces influence only the near surface dislocations, an assumption regarding their density was required. For simplicity, the total near surface dislocation length was taken to be the sample circumference times the number of slip planes per gauge length. A slip plane spacing of 1 μm was assumed. The sample stress required to move a near surface dislocation to the metal-oxide interface is the product of the image force per length obtained from equation 5 and the total dislocation length divided by the sample area, expressed as follows:

$$T = \frac{F}{A} \frac{2\pi r l}{h}$$

where F is the image force per length of dislocation line, A is the sample area, r is the sample radius, l is the gauge length and h is the slip plane spacing.

B. Sample Gripping Effects on Mechanical Properties

Stresses can be imposed on a tensile test sample by the grips because of clamping procedures, stress concentrations at sharp dimensional changes or in single crystals because of bending moments. The first two sources of grip stresses can be minimized by proper grip design and gauge section in the sample. The third source is generally not a problem for bulk polycrystalline materials with random grain orientations but the small test samples required for ion beam irradiation will have a small number of grains per cross-section and may have a crystallographic texture. The grip stresses imposed on these samples may be similar to those imposed on single crystals, and therefore consideration of this effect is needed.

A recent study of the grip stresses imposed on single crystals has been conducted by MacCrone,[93] who suggests the following three factors which are involved in maintaining the alignment of a single crystal during plastic deformation:

1. Crystallographic rotation of the tensile axis;
2. Bending moments at each grip, and
3. A relative sideways displacement of the grips.

No grip stresses are imposed by factor number one, while two and three do impose grip stresses. A schematic of these operations is shown in Fig. 38. Fleischer and Chalmers[94] have shown that the bending stresses greatly exceed the stress caused by the offset. This bending moment is a positive maximum at the upper end of the sample, zero at the center, and a negative maximum at the lower end of the sample. The magnitude of the bending moment and therefore the grip stress is a function of the amount of grip offset without restraint. This offset is a maximum for single crystal deformation when a single slip plane is operative and can be compensated by slip on a secondary system. The ratio of the grip stress, σ_g, to the applied stress, σ_a, is a measure of the relative importance of the grip stress on the measured properties.
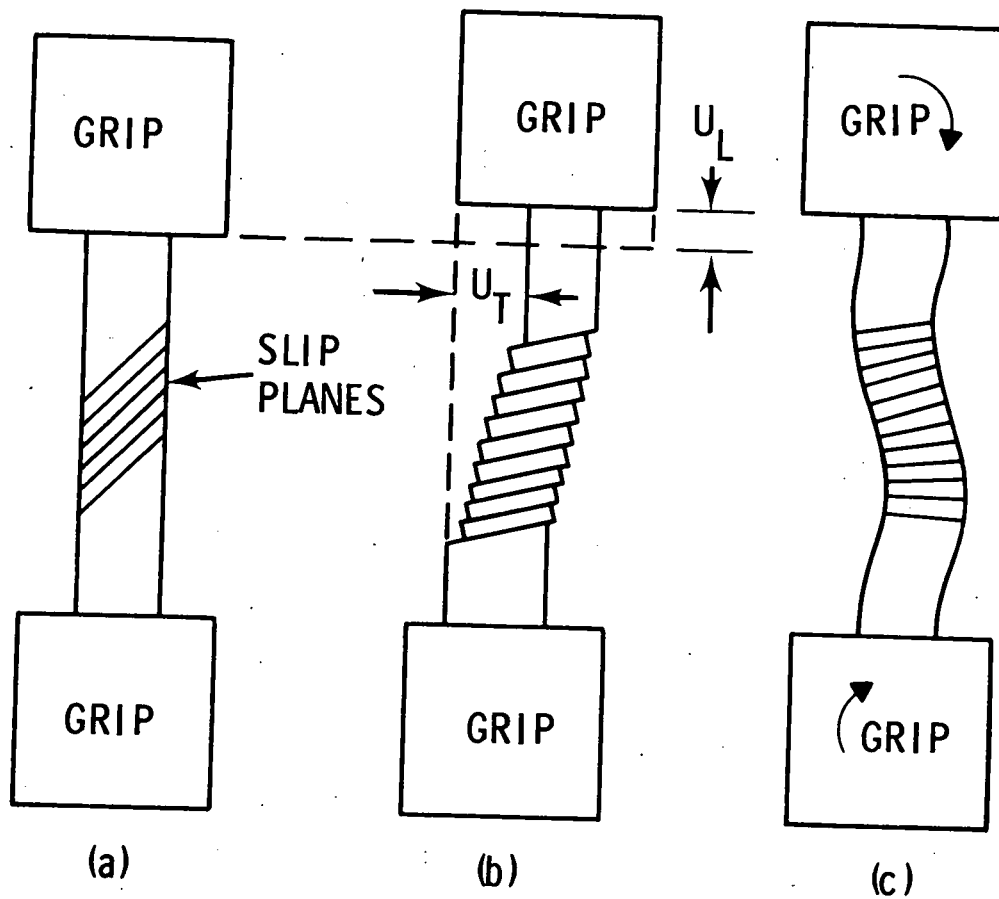
Figure 38. Schematic Representation of Plastic Deformation
of a Single Crystal a, b) With Grip Displacement
and No Grip Stresses c) With Grip Imposed Stresses
(After MacCrone[93])

Some aspects of the ion beam irradiation test specimens
which will minimize the bending moment imposed grip stresses
are: 1) the materials to be tested (Ni, Nb) will undergo
slip on more than one system because of the presence of high
angle boundaries, and the expected textures will favor multiple
slip (Ni - [111], Nb - [110]); 2) the gauge section will be
short relative to the grip spacing, placing the gauge section
near the point of zero bending moment; 3) multiple slip will
be favored in the elevated temperature tests.

C. Sample Size Effects on Mechanical Properties

The size dependent mechanical properties of metals can be
roughly divided into three categories: 1) whiskers and thin
foils where the thin dimension is less than 1 μm, 2) foils or
wires where 1 μm $\leq$ t $\leq$ d, where d is the grain diameter
3) bulk single and polycrystalline material. The strength of
whiskers is controlled primarily by their extremely low dis-
location density and the difficulty of nucleating dislocations
while the strength of thin foils thinned from the bulk is con-
trolled by free surface drag forces. Thin foils deposited from
the vapor have high dislocation densities, 10^{10} - 10^{12} lines/cm^2,
but their motion is impeded by their mutual interaction and
surface drag forces.

Foils and wires in the mid-thickness range where 1 μm < t < d
are strongly affected by intrinsic surface effects if grip effects
are overcome; however, a considerable quantity of published data
on size effects probably reflects extrinsic surface effects from
poor to improper surface preparation and grip effects.

Size effects in bulk materials persist to greater thick-
nesses in single crystals than polycrystalline materials be-
cause of the interferring effect that grain boundaries have on
the interaction between free surfaces and internal grains. A
size effect in copper single crystals as large as 0.64 cm di-
ameter was observed by Garstone, et. al.[95]

The previous comments about size effects pertain primarily to tensile and creep properties of metals. Size and surface effects on fracture and fatigue properties of metals generally extend to larger sizes than they do for tensile and creep. An example of this is the surface defect dependence of high cycle fatigue properties.

1. Tensile Properties

The high damage rates (10^{-3} - 10^{-2}dpa/s) attainable with heavy ion irradiation have made it possible to study the micro-structural changes of metals at damage levels of 100 to 200 dpa with relatively short irradiations. Heavy ion irradiation of materials for mechanical property studies is also a desire-able goal; however, the small penetration depth of heavy ions would require the use of samples less than 1 µm thick for 7.5 MeV Ta or 5 MeV Ni and less than 5 µm thick for 20 MeV C or 1.3 MeV H. The sub-micron thick samples necessary for this type of study can be categorized as whiskers, films thinned from the bulk or thin films deposited from vapor phase.

The fracture stress of iron and copper whiskers has been studied as a function of diameter by Brenner[96] and found to be very diameter dependent with considerable scatter in the results, as shown in Fig. 39. Brenner determined that the average strength of the iron and copper was a function of $\frac{1}{d_{ave}}$, where d_{ave} is the average of five whiskers of approximately equal diameters. This diameter dependence indicated that the strength was controlled by surface defects or surface pinning of dislocations. A $\frac{1}{d^2}$ dependence would be expected from the operation of a dislocation source; however, the operation of a dislocation source may have been necessary in the stress-strain sequence. Copper and iron whiskers have been studied more recently by Yoshida, et.al.[97, 98] Their results also showed a strong dependence of strength on diameter; however, they observed an upper yield strength with considerable

95
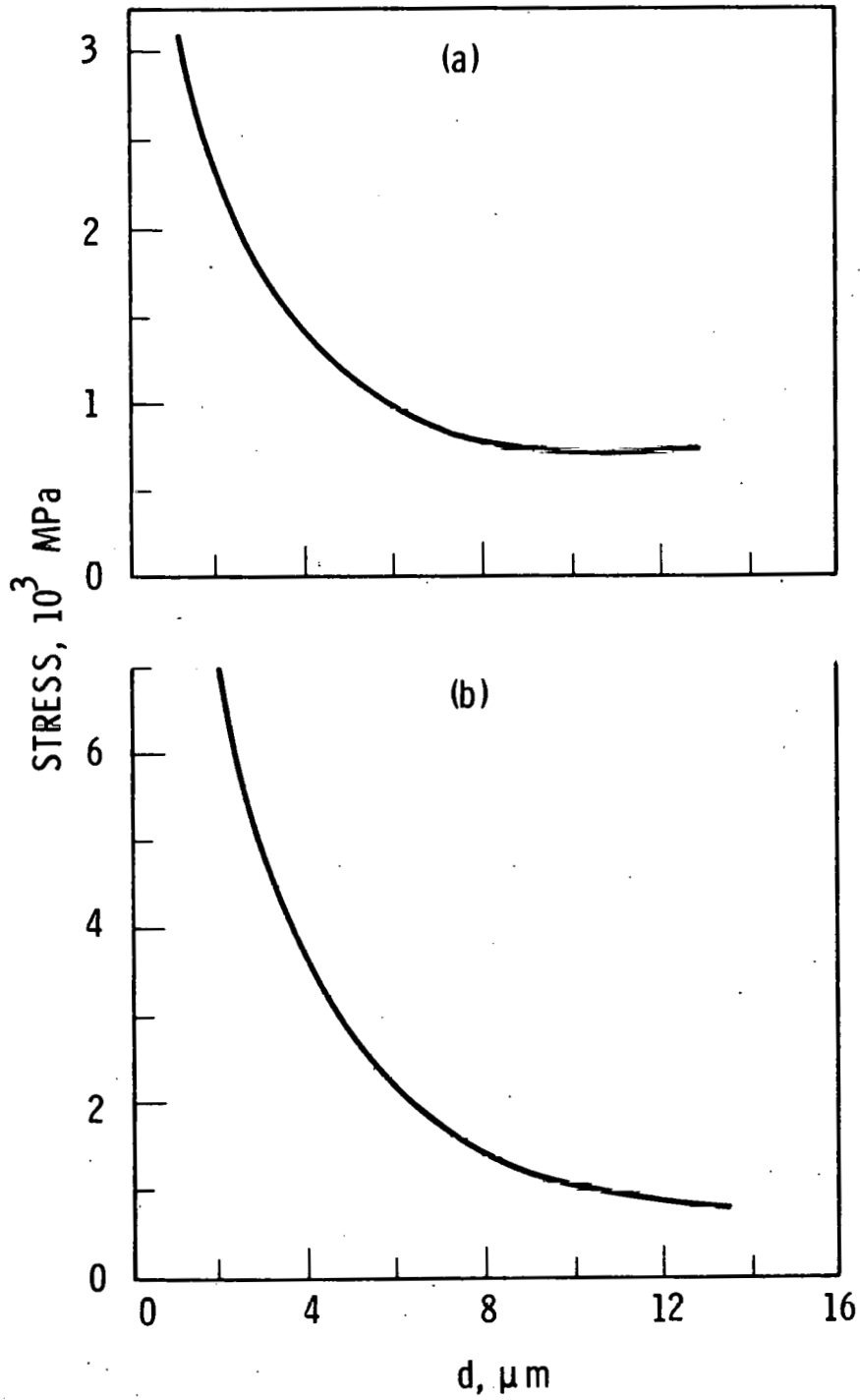
Figure 39. Tensile Strength Versus Diameter of a) Copper and b) Iron Whiskers After S. S. Brenner[96]

plastic flow occurring after yielding and at a much lower stress. They attributed the yield point to the sudden increase of mobile dislocations associated with the nucleation and propagation of Luders bands.

Metal foils thinned from the bulk are used in electron beam irradiation studies where in-situ microstructural studies can be performed; however, their use for heavy ion irradiations for mechanical property studies is not practical because of preparation and handling difficulties. Deposited films, either electron beam evaporated, sputtered or electrodeposited, would be somewhat easier to prepare; however, the properties of vapor deposited films differ from annealed bulk material. The tensile strength of vapor-deposited nickel was found[99] to be approximately thickness independent above 3000 $\overset{o}{A}$, as shown in Figure 40 with a tensile strength of 180,000 lb/in^2. Annealing these foils will lower their strength to a value closer to bulk nickel; however, the strength of annealed foils should exceed that of bulk nickel by an amount roughly equal to the surface pinning stress. For a 3000 $\overset{o}{A}$ thick foil, the surface pinning of dislocations should contribute about 10,000 psi to the yield strength of bulk nickel which is approximately 10,000 psi.

In summary, the use of high z ions to simulate neutron damage for mechanical property studies would require whiskers or foils. Annealed vapor deposited foils would be the most suitable for this experiment, if the property-thickness relationship does not change with annealing. Surface contamination during preparation, annealing or irradiation would present greater experimental difficulties than preparation, handling, or testing. In fact, thin foils are so surface sensitive that contamination may obscure the property changes caused by irradiation.

The penetration depths of low z ions, such as H^+, D^+ or He^+, at 10 - 20 MeV are such that sample thicknesses much greater than 1 μm can be fully penetrated. In fact, sample thicknesses
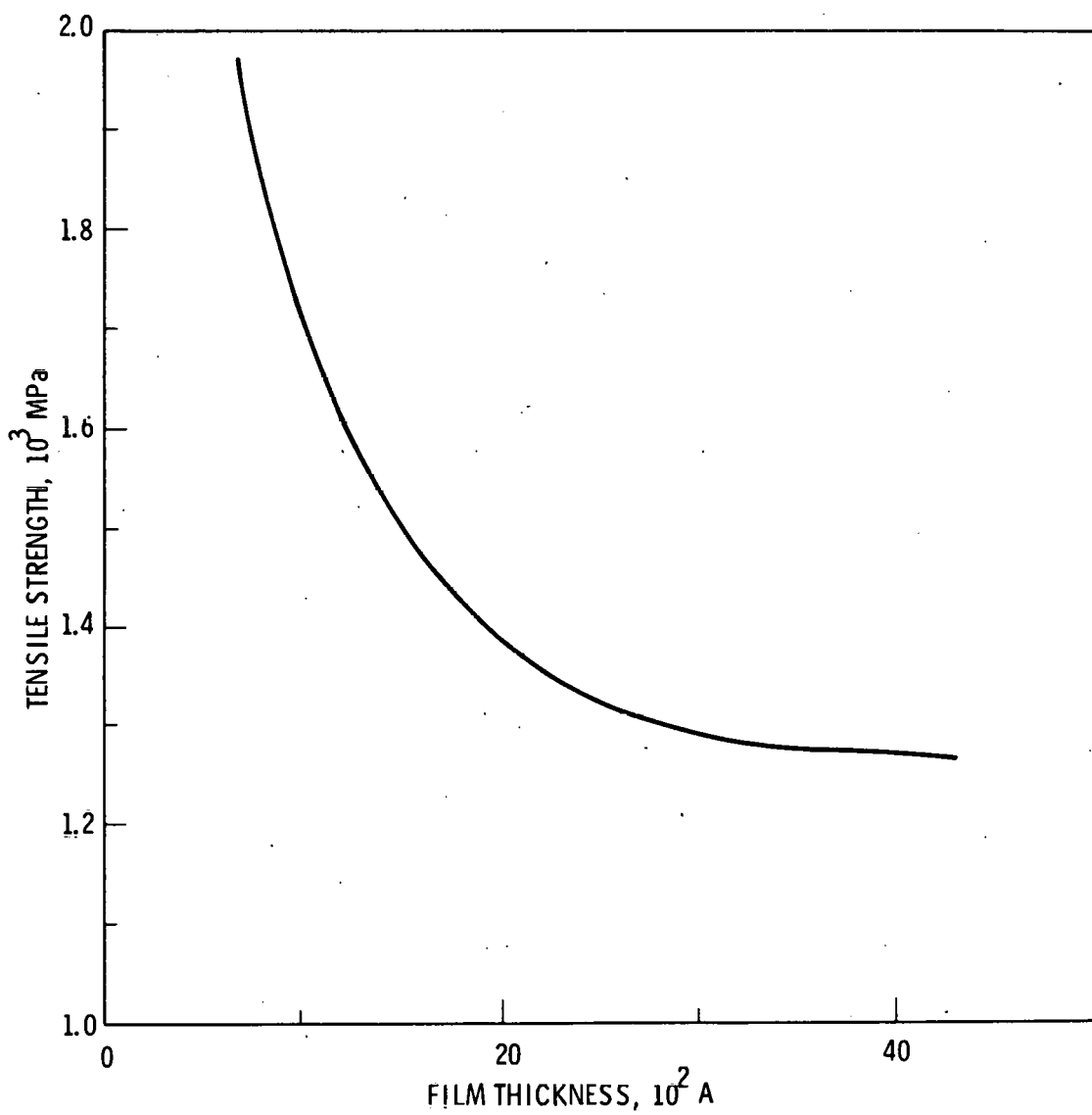
Figure 40.   Tensile Strength of Vapor Deposited Nickel Versus Thickness (After D'Antonio et.al.[99])

of up to 375 μm are possible. The tensile properties of metals within this size range have not been studied extensively, although some scattered data exists. The room temperature tensile properties of copper foils in the size range of 2 μm to 53 μm studied by Lawley and Schuster[100] are shown in Fig. 41. For foil thicknesses less than 26 μm, the following relationship between yield strength and thickness was observed:

$$\sigma_y = \sigma_0 + kt^{-1/2} \tag{7}$$

where σ_0 is a lattice friction stress, k is a constant and t is the foil thickness. This relationship is identical in form to that derived by Hall-Petch[101] for the propagation of a luders band at the lower yield stress in a polycrystalline metal, except the thickness has been substituted for the grain size. The authors[100] proposed that a surface film, probably an oxide layer, exists which acts as a barrier to dislocation egress at the free surface, in an analogous manner that a grain boundary inhibits slip band propagation in polycrystals. The surface layer supports a stress equal to $kt^{-1/2}$ above the lattice friction stress σ_0. The values of k and σ_0 are similar in magnitude to the values obtained from the Hall-Petch relationship. The decreasing yield strength with decreasing thickness for the coarse grained foils was attributed to weakening caused by grain boundary thermal etching; in fact, the coarse grained foils are not considered representative because of this problem. No systematic dependence of the ultimate tensile strength with thickness was observed. The ductility decreased with decreasing foil thickness for all grain sizes with plastic deformation occurring randomly throughout the gauge section. Qualitatively, the authors attributed the decrease in work hardening rate to an increased probability that dislocation loops reached the foil surface before encountering obstacles.

Figure 41. Tensile Properties of Fine Grained (~10μm) Copper Foils Versus Thickness (After Lawley and Schuster[100])

Figure 41 (cont'd)

101

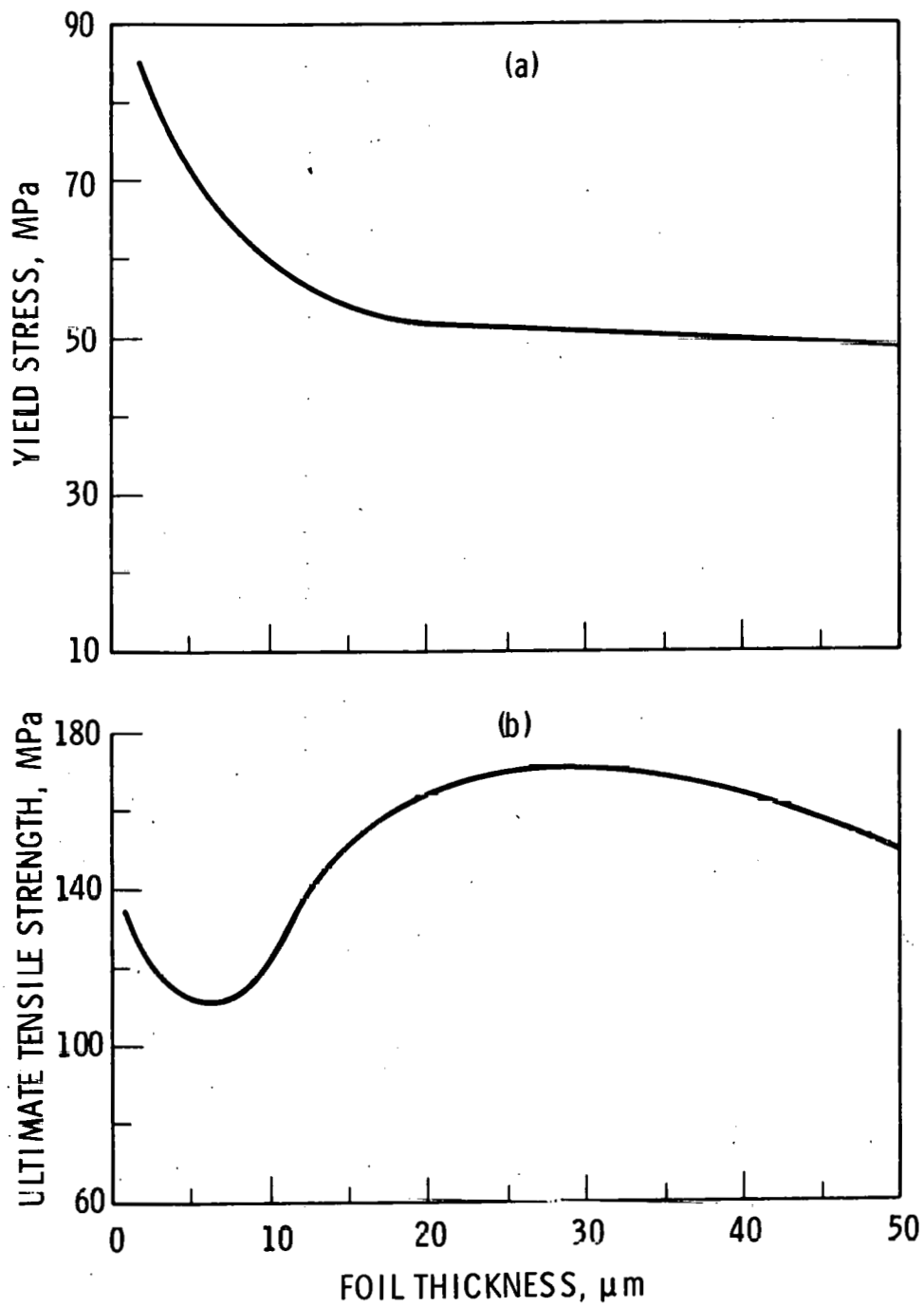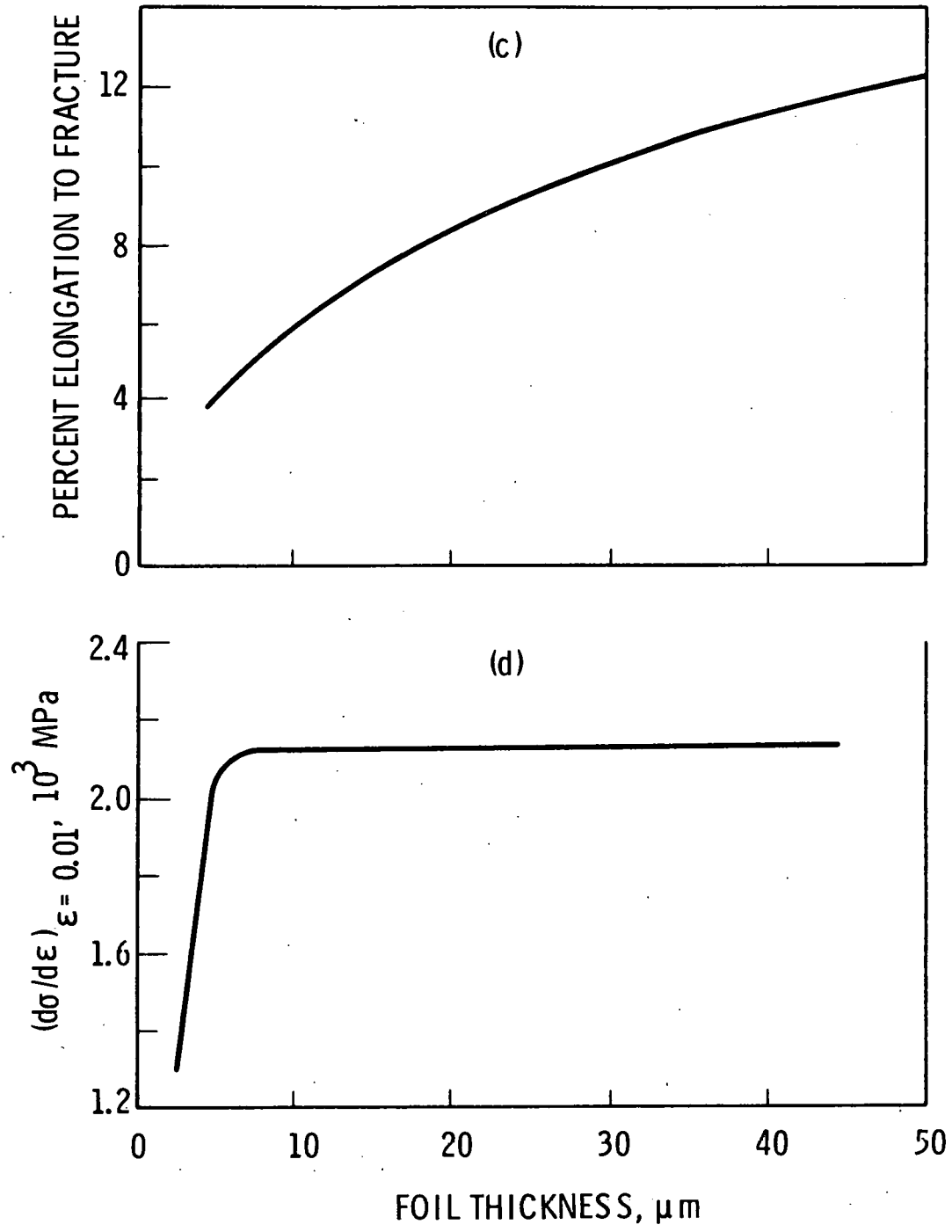A Hall-Petch type of relationship between the yield strength and foil thickness was also observed by Aleksanyan, et.al,[102] for electrolytic copper films in the thickness range 5 μm to 70 μm. A relationship between thickness and ductility very similar to that observed by Lawley and Schuster was found.

Aluminum and aluminum alloy foils prepared by rolling and annealing in the thickness range 10 μm to 100 μm were examined by Kadamer, et. al.[103] Unfortunately, the grain size varied with thickness which makes interpretation of their data ambiguous. Also, a 5 μm thick oxide was present on their samples which further complicates their results. However, their ductility results were similar to those obtained for copper foils[100, 102] which leads to the possible explanation that a surface oxide contributed to the low ductility of copper and aluminum foils at thicknesses of about 10 μm. Only high purity aluminum samples had a strength to thickness dependence similar to copper.

A comparison of size effects in single crystal copper and cube textured copper foils has been made by Sumino and Yamamoto.[104] The authors found the yield strength of 50.8 μm to 96.7 μm single crystals and 6.6 μm to 96.7 μm cube textured foils to be independent of thickness. Also, the stress-strain curves exhibited three stages of slip except for cube textured foils less than 10 μm thickness which exhibited only stage I slip with high work hardening rates. The cube textured foils behave as pseudo-single crystals because the degree of grain mis-orientation is quite low due to the crystallographic texture. Some earlier results on the size dependence of single crystal plasticity presented by Suzuki, et. al,[105] showed a marked increase in the range of easy glide with decreasing crystal dimensions while the yield strength was independent of size over the size range 60 μm to 1000 μm. The yield strength results of Sumino and Yamamoto[104] disagree with those of Lawley and Schuster[100] while Suzuki, et. al[105] tested crystals of larger dimensions. Garstone, et. al,[106] confirmed the size dependence of easy glide

in copper single crystals observed by Suzuki, et. al,[105] in the size range 5000 μm to 10,000 μm. Suzuki, et. al,[105] proposed a size dependent mechanism for easy glide based on the exhaustion of Frank-Read type dislocation sources which is a function of crystal dimensions. The following expression for stage I shear strain was given:

$$S = ns \exp(-Pr) \qquad (8)$$

where S is the total shear strain, n is the number of Frank-Read type sources in the annealed state, s is the shear strain per source, P is the number of obstacles a dislocation will meet as it sweeps out an area equal to the total sample cross-section of radius r.

2. Creep Properties

Creep deformation studies of foils or wires have been conducted primarily for the purpose of studying low stress, elevated temperature (~0.9 Tm) creep mechanisms, such as Nabarro-Herring or Coble creep. Foils or wires with a single grain through the thickness or diameter are used in these experiments so that the displacement of one grain relative to its neighbors can be measured. While lower temperatures and higher stresses would be used in any ion irradiation creep studies, one of these mechanisms may be operative because of the sample size/ grain size ratio. For aluminum, Mohamed and Langdon[107] have shown that Nabarro-Herring creep is dominant at stresses up to 1000 psi and 10^{-4} cm grain diameter at 0.9 Tm while Coble creep is dominant for grain sizes less than 10^{-4} cm. At 0.5 Tm, Coble creep is dominant for grain sizes less than 10^{-2} cm, while Nabarro-Herring creep is not operative. Grain sizes in the range 10^{-2} to 10^{-3} cm and temperatures around 0.5 T_m are quite likely for ion irradiation test samples and therefore a brief discussion of these mechanisms is needed.

Coble creep occurs by the stress-directed diffusion of vacancies along grain boundaries, with the following theoretical equation[108] for the strain rate:

$$\dot{\epsilon} = \frac{150}{\pi} \frac{\Omega\sigma\delta D_{gb}}{d^3 kT} \qquad (9)$$

where δ is the effective boundary width for enhanced diffusion, Ω is the atomic volume, σ is the stress, D_{gb} is the grain boundary diffusion coefficient, d is the grain diameter, and kT have their usual meaning. Nabarro-Herring creep occurs by the stress-directed diffusion of vacancies through the lattice, with the following theoretical equation[109,110] for the strain rate:

$$\dot{\epsilon} = \frac{B\Omega\sigma D_\ell}{d^2 kT} \qquad (10)$$

where D_ℓ is the lattice self-diffusion coefficient. Nabarro-Herring creep has been shown by Burton[112] to be a function of sample thickness where the strain rate is proportional to $\frac{1}{(td)}$. A similar solution was derived by Gibbs[113] when volume diffusion dominates and a $\frac{1}{dt^2}$ dependence at lower temperature when grain boundary diffusion dominates, as in Coble creep. Vacancies are emitted from grain boundaries normal to the applied load and absorbed at boundaries parallel to the applied load. For the case of a single grain through the thickness, the free surface is the sink and the diffusion distance is a function of the thickness. A similar dependence exists when grain boundary diffusion is dominant. For samples with 2 or 3 grains through the thickness, the Nabarro-Herring & Coble creep rates will be values between the bulk, as expressed by equations 9, 10, and for thin foils with the thickness dependence.

The relationship between grain size, stress and creep mode can be graphically presented on a deformation mechanism map such as those calculated by Mohamed and Langdon[107] for aluminum. A similar map for nickel was plotted and is shown in Fig. 42. The boundaries separating the labelled regions are values of $\frac{d}{b}$
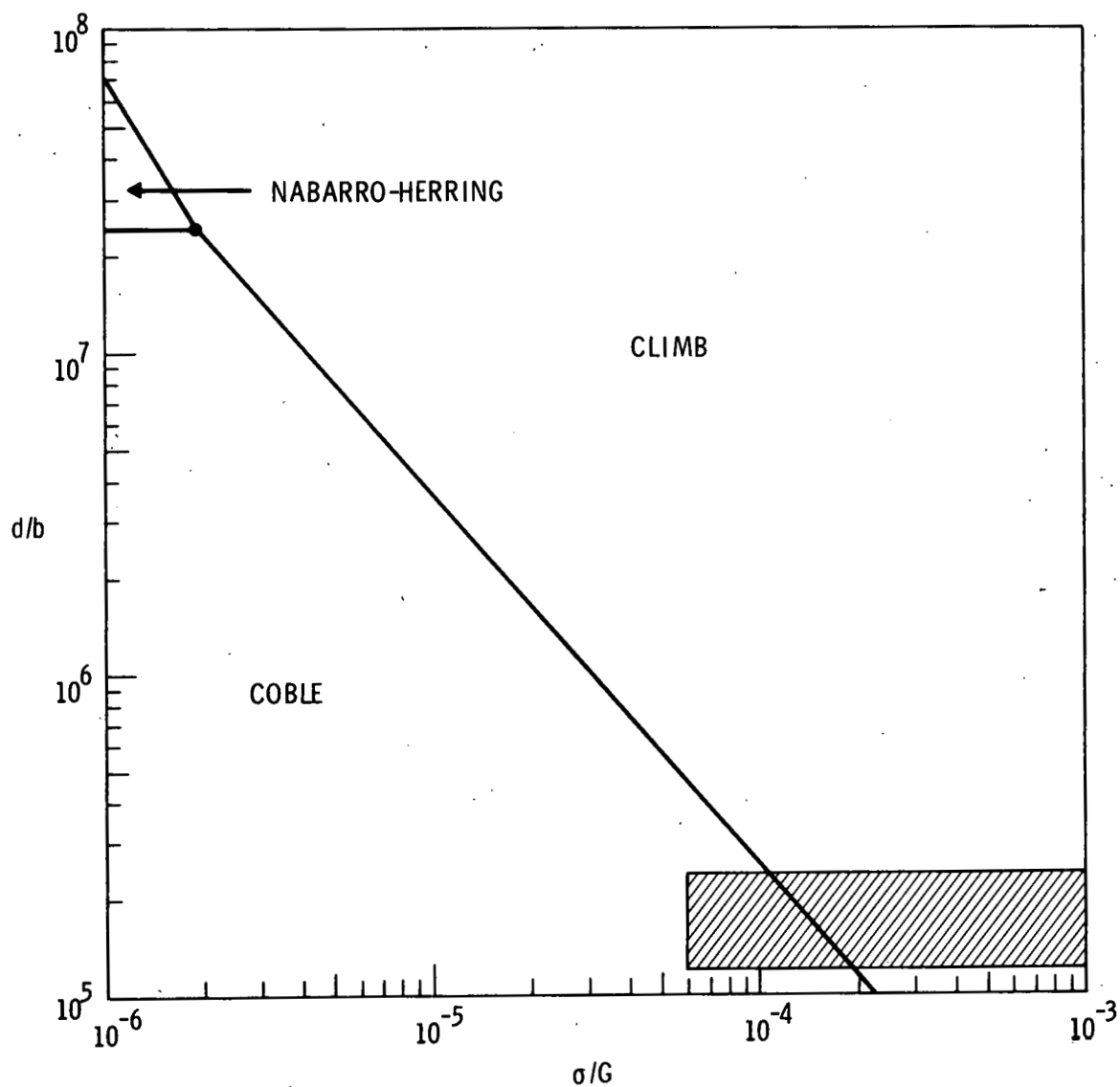
Figure 42. Deformation Mechanism Map for Bulk Nickel at
550°C Following Construction Method Used By
Mohamed and Langdon[107] (See Appendix)

and $\frac{\sigma}{G}$ which result in equal creep rates for the two mechanisms. Deformation mechanism maps which relate $\frac{t}{b}$ to $\frac{\sigma}{G}$ have also been determined using the methods of Mohamed and Langdon[107] and the creep rate equations derived by Gibbs. The construction method is outlined in the appendix and the map for nickel is shown in Figure 43. The shaded regions in Figs. 42-43 are the ranges of grain size, sample thickness, and stress values expected for the ion irradiation experiments.

The small samples required for ion irradiation experiments will have a minimum of 3 grains across the diameter and will probably have a creep behavior intermediate between bulk samples and thin samples where there is only 1 grain across the diameter. It is significant that the major creep mechanism, ignoring irradiation effects, will be by a climb process whether bulk or thin behavior dominates. The exception to this is for low stresses ($\sim$1000 lb/in^2) and small grain sizes ($\sim$60μm) where a large contribution to the total creep strain may come from Coble type creep mechanism.

A deformation mechanism map for nickel showing the boundaries for irradiation, climb, Coble & Nabarro-Herring creep mechanism would be desireable. The uncertainty surrounding irradiation creep mechanisms and models and the time required, to construct such a map discouraged such an effort at this time. However, a relaxation-time map for 304L stainless steel as a function of stress, temperature and relaxation time constructed by Gittus[113] is shown in Fig. 44. For 304L stainless steel, Gittus determined that irradiation creep is dominant below 0.48 Tm for $\frac{\sigma}{\mu}$ less than 10^{-4}. Bulk behavior was assumed for the construction of this map so that a shift in the boundary between irradiation and Coble creep is expected if thin sample behavior is dominant. Using the following Coble Creep equation for thin sample behavior:

$$\dot{\varepsilon} = \frac{66.8 \ D_{gb} \ Gb}{kT} \left(\frac{b}{d}\right)\left(\frac{b}{t}\right)^2\left(\frac{\sigma}{G}\right) \tag{11}$$
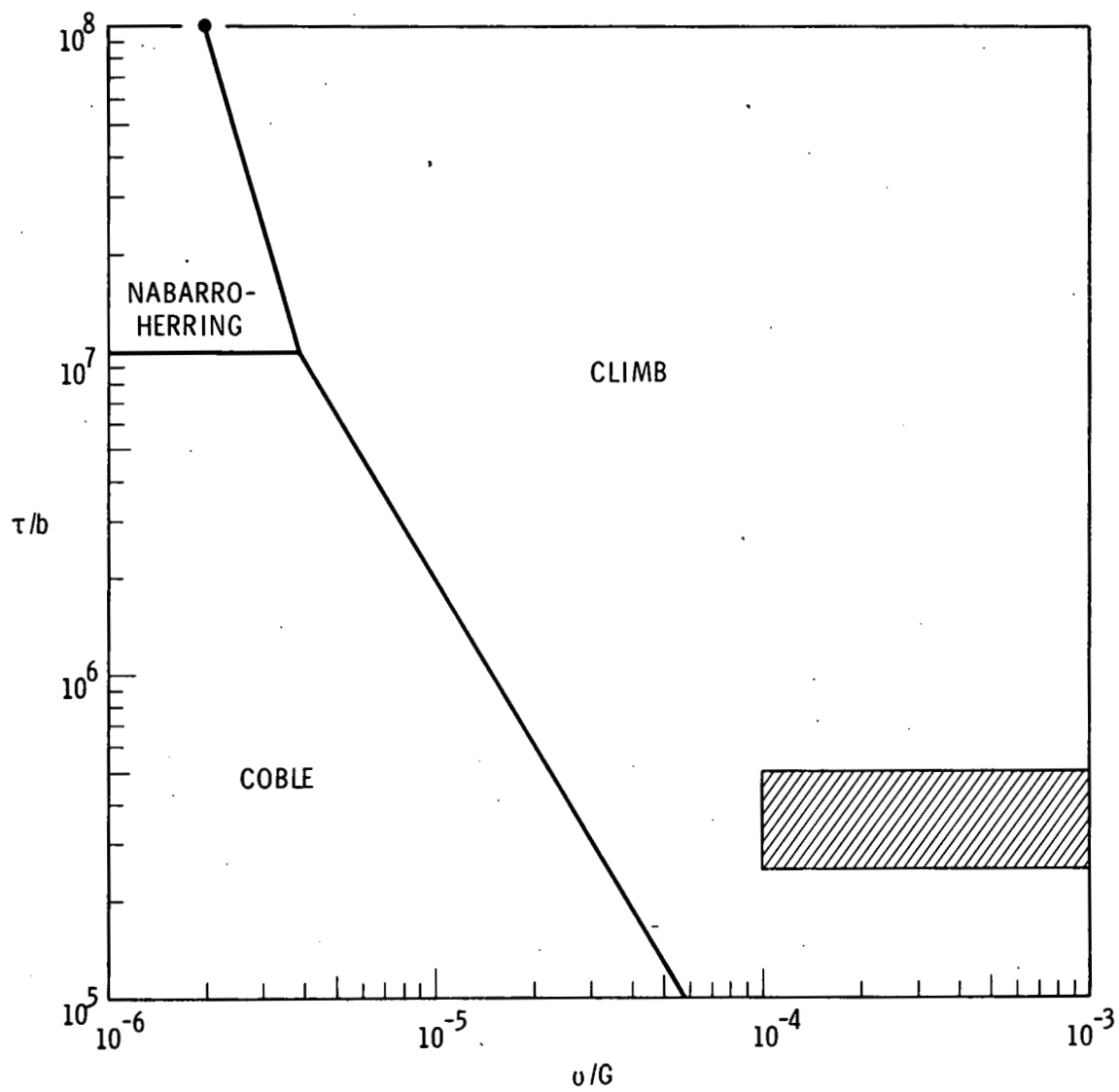
Figure 43. Deformation Mechanism Map for Thin Nickel Samples
at 550°C Following Construction Method by Mohamed
and Langdon[107] With Creep Equations After Gibbs[112]
(See Appendix)

107

where d is the grain size in the longitudinal direction, the shift in the boundary between irradiation creep and Coble creep was calculated as a function of thickness. A value of $Dgb = 1.65 \times 10^{-8}$ cm^2/s was calculated from the given conditions and assuming bulk behavior. Taking the thickness equal to the grain size of 60 μm, equation 11, predicts a relaxation time equal to the bulk value of 3×10^6 s. The boundary between irradiation creep and Coble creep is shifted to 0.43 Tm at a relaxation time of 5×10^6 s for a thickness of 64 μm and a grain size in the longitudinal direction of 60 μm. For a wire test sample of 120 μm and a grain size in the longitudinal direction of 60 μm, the creep mechanism boundaries should be displaced from those shown in Fig. 44.

Matlock and Nix[114] have developed a creep equation for thin sample deformation with the sample gauge section divided into regions where one grain traverses the thickness and the grains are one-half the thickness. In region 1 it is assumed that grain matrix deformation and grain boundary sliding mechanisms are independent processes while in region 2 grain boundary sliding is dependent on accommodation in adjacent grains. The following equation for the strain rate of thin samples was derived:

$$\dot{\varepsilon}_T = \dot{\varepsilon}_g + \frac{L_1}{L}\dot{\varepsilon}_{gbs} + \frac{2L_2 k_2 \eta_2}{Lk_1 \eta_1} \frac{\dot{\varepsilon}_{gbs}\dot{\varepsilon}_g}{\dot{\varepsilon}_{gbs} + \dot{\varepsilon}_g} \tag{12}$$

where $\dot{\varepsilon}_T$ is the total strain rate, $\dot{\varepsilon}_g$ is the strain rate due to matrix deformation, $\dot{\varepsilon}_{gbs}$ is the grain boundary sliding rate, L_1 is the length of region 1, L_2 is the length of region 2, L is the total length, k is a geometric factor relating the grain boundary orientation to the tensile axis, and η is the number of grain boundaries per unit length along the tensile axis. While this model does not directly relate strain rate to the thickness it does help to bridge the gap between the Coble creep expression for thin samples, where t = d, the deformation mechanism map derived from this, Fig. 43, and bulk creep behavior.

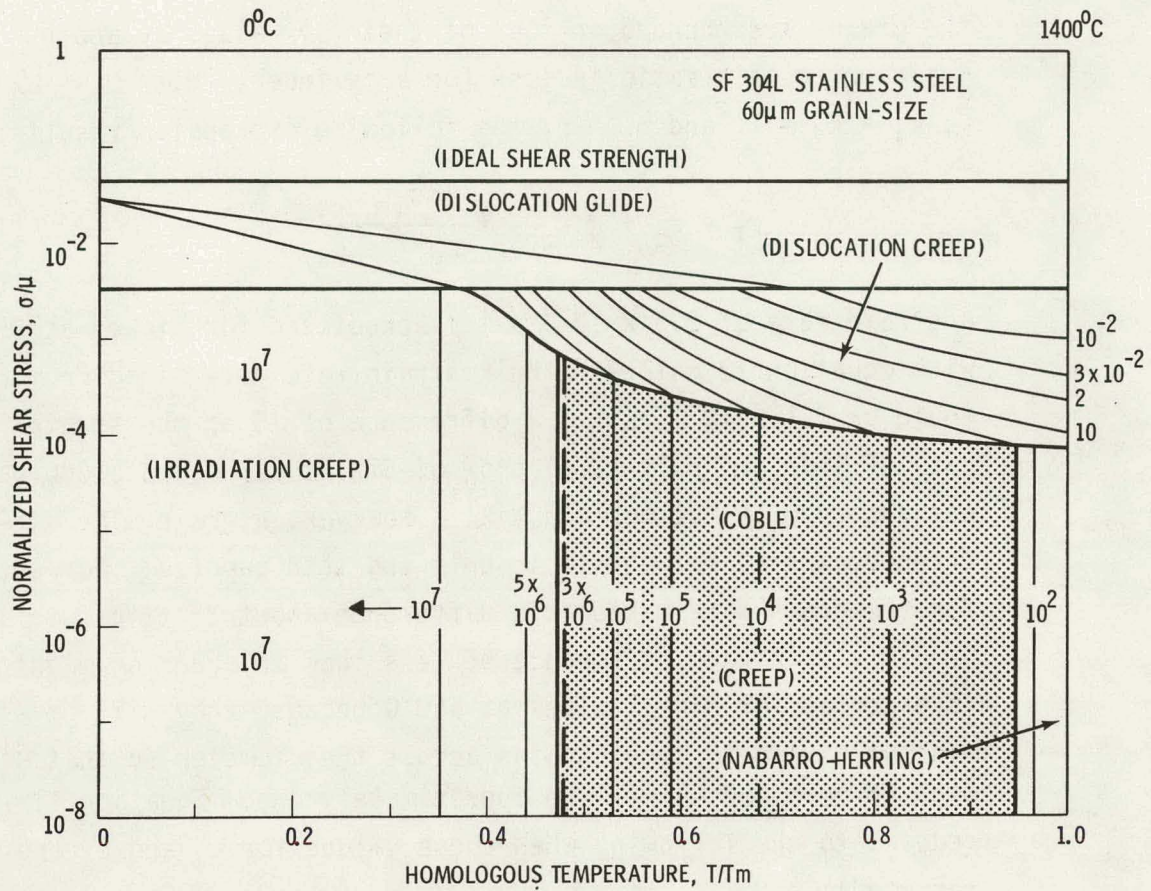Figure 44.   Relaxation-time for SF 304L stainless steel with a grain-size of 60μm in a neutron-flux. Bold lines are field boundaries. The dashed bold line is a field boundary calculated from the theory given in the present paper. Thin lines are contours of constant relaxation time (marked on each in seconds). (From J. H. Gittus[114])

However, modifications to equation 11 would be necessary before it would apply to cylindrical samples because in a sheet sample, for which the equation was derived, the majority of the grains are bounded on four of their six sides by another grain while this ratio is less for a cylinder. With $L_1 = L_2 = \frac{L}{2}$, $k_1 = k_2 = 1$, and $\eta_2 = \eta_1$ the following expression results:

$$\dot{\varepsilon}_T = \dot{\varepsilon}_g + \frac{1}{2}\dot{\varepsilon}_{gbs} + \frac{2\dot{\varepsilon}_g\dot{\varepsilon}_{gbs}}{\dot{\varepsilon}_g + \dot{\varepsilon}_{gbs}} \qquad (13)$$

A strain rate of 2.3×10^{-9} s^{-1} is predicted for nickel at $550^{\circ}C$ with equation 12 while the bulk strain rate determined from $\dot{\varepsilon}_g^0$ would be 2.1×10^{-10} s^{-1}. A difference of 15 in the strain rate of thin and bulk samples of Ni-6%W at $627^{\circ}C$ and 5,000 psi was observed by Matlock and Nix;[115] however, a grain size difference existed between their bulk and thin samples. Correction for the grain size makes this difference about 25 times.

A strain rate difference of less than an order of magnitude is expected for nickel wires at $550^{\circ}C$ because they will have a minimum of two to three grains across the diameter so that $\frac{L_1}{L}$ will be zero and $\frac{L_2}{L}$ will be approximately one. Equation 11 reduces to the following when these values for L_1 and L_2 are inserted:

$$\dot{\varepsilon}_T = \dot{\varepsilon}_g + \frac{2\dot{\varepsilon}_{gbs}\dot{\varepsilon}_g}{\dot{\varepsilon}_{gbs} + \dot{\varepsilon}_g} \qquad (14)$$

A total strain rate for nickel wires at $550^{\circ}C$ and 5000 lb/in^2 equal to 9.3×10^{-10} s^{-1} is predicted by equation 13, which is only four times greater than that predicted for bulk nickel.

References

1. R. Booth, H. H. Barschall, and E. Goldberg, IEEE Transactions on Nuclear Science, Vol. NS-20, No. 3, p. 472, 1973.

2. H. H. Barschall, private communication. See also Phys. Med. Biol. 18, 64, 1973.

3. P. J. Persiani, ANL/CTR/73-02, also D. Steiner, private communication.

4. M. C. Cline and C. R. Emigh, Proc. 1st ANS Topical Meeting on the Technology of Controlled Nuclear Fusion, San Diego, Calif, p. 313, 1974, Vol. 1.

5. Two component torus - Joint Conceptual Design Study, Plasma Physics Laboratory, Princeton, New Jersey, and Westinghouse Electric Corporation, Pittsburgh, Pennsylvania, June 1974.

6. ORMAK F/BX A Tokamak Fusion Test Reactor, Eds., P.M. Haubenrich and M. Roberts, ORNL-TM-4634, June 1974.

7. T. H. Batzer et al., UCRL-51617, August 1974.

8. R. J. Burke, T. A. Coultas, and M. Petrick, p. 350 in Proc. First Topical Meeting Tech. of Controlled Nuclear Fusion, CONF-740402-P1, Vol, 1, 1974.

9. R. W. Conn and D. L. Jassby, UWFDM-119, 1975.

10. P. N. Haubenreich, D. G. McAlees, M. Roberts, Trans. Am. Nucl. Soc., 21, p. 41, 1975.

11. P. H. Sager, M. Jonzen, D. Kearney, R. Thomas, W. Toffolo, T. Woods, Trans. Am. Nuclear Soc. 21, p. 25, 1975.

12. W. Stacey, K. Evanc, J. N. Brooks, Trans. Am. Nucl. Soc. 21, p. 32, 1975.

13. A. P. Fraas, ORNL-TM-3096, May 1973.

14. B. Badger et al., Wisconsin Tokamak Reactor Design, UWMAK-I, UWFDM-68, Nov. 1973.

15. R. W. Conn, G. L. Kulcinski, M. Abdou, R. W. Boom, G. A. Emmert, Y. Eyssa, M. Hilal, J. Kesner, W. Lue, C. W. Maynard, A. Mense, J. Scharer, T. Sung, I. Sviatoslavsky, D. Sze, W. Vogelsang, L. Wittenberg, T. Yang, W. Young, Paper IAEA/CN/33/G1-2 given at Fifth IAEA Conference on Plasma Physics and Controlled Nuclear Fusion Research, Tokyo, Nov. 1974. (See also UWFDM-114).

16. Unpublished data on UWMAK-II, University of Wisconsin Design Team.

17. A Fusion Power Plant, R. G. Mills ed., MATT-1050, Princeton Plasma Physics Laboratory, Aug. 1974.

18. J. T. D. Mitchell and R. Hancox, CLM-P319 Aug. 1972.

19. J. T. D. Mitchell, et al., CLM-R121 June 1972.

20. K. Sako et al., JAERI-M-5502, Dec. 1973.

21. K. Sako et al., Paper IAEA-CN/33/G1-5 in ref. 15.

22. J. R. Powell et al., BNL-18439, Nov. 1973.

23. J. R. Powell et al., BNL-18236, June 1973.

24. E. Bertolini et al., Paper IAEA-CN/33/G1-1 in Ref. 15.

25. B. Kadomsev, private communication.

26. J. Williams et al., p. 70 in reference 8.

27. L. A. Booth (compiler) LA-4858-ms, Vol. I., February 1972.

28. J. Hovingh et al., p. 96 in ref. 8.

29. F. H. Bohn, H. Conrads, J. Darvas, and S. Forster, p. 107 in Fifth Symp. Eng. Prob. of Fusion Research, Princeton, Nov. 1973, and other unpublished results S. Forster.

30. M. J. Lubin and A. P. Fraas, Scientific American, 224, No. 6 June 1971.

31. R. W. Werner et al., UCRL-74054-2, April 1974.

32. W. C. Walkenhauer, B. R. Leonard Jr., A. M. Sutey, and R. W. Moir, p. 238 in ref. 8.

33. An Engineering Design Study of a Reference Theta Pinch Reactor (RTPR), LA-5335 ANL-8019, March 1974.

34. S. G. Varnado, V. L. Dugan, R. D. Klett, R. H. Richards, and S. G. Vandevender, SAND-74-0160, October 1974.

35. Private communication with O. K. Harling.

36. P. L. Hendrick, A. L. Bement and O. K. Harling, Nuc. Instrum. and Methods, 124, 389-393 (1973).

37. S. N. Buckley, AERE-R-5944, Vol. 2, p. 547, 1968.

38. J. J. Holmes and L. O. Petersen, Phil. Mag., 16, 845, 1967.

39. S. D. Harkness, F. L. Yagee and F. V. Nolfi, Jr., ANL-7883, Argonne National Laboratory, 1972.

40. D. L. Bodde, S. M. Thesis (Massachusetts Institute of Technology) 1971.

41. Private communication: R. Vandervoort, Lawrence Livermore Laboratory.

42. A. D. Marwick, J. Nuc. Mat., 56, 355-358, 1975.

43. R. S. Nelson, D. J. Mazen and J. A. Hudson, J. Nuc. Mat., 37, 1-12, 1970.

44. G. L. Kulcinski, J. J. Laidler and D. G. Doran, Rad. Effects, 7 195-202, 1971.

45. G. L. Kulcinski, in Applications of Ion Beams to Metals, Ed. by S. T. Picraux, E. P. Eer Nisse and F. L. Vook (Plenum Press, NY) pp. 613-637, 1974.

46. D. G. Doran and G. L. Kulcinski, Rad. Effects, 9, 283-284, 1971.

47. A. J. E. Foreman, AERE-R7135, 1972.

48. "Educational Programs and Facilities in Nuclear Science and Engineering," Oak Ridge Associated Universities, Sept. 1968.

49. G. L. Kulcinski, R. Lott and T. Ynag, Univ. of Wisconsin FDM, No. 42, 1973.

50. D. G. Doran, J. R. Beeler, N. D. Dudey and M. J. Flus, Hanford Eng. Dev. Lab. Report HEDL-TME 73-76, 1973.

51. D. W. Keefer, Atomics International Report AI-AEC13135, 1974.

52. M. T. Robinson, BNES Nuclear Reactor Conference at Culham Laboratory, p. 364, 1969.

53. J. Linhard, M. Scharff, and H. E. Schiott, Matemtiskfysiske Meddelesev, 13, 1, 1963.

54. M. T. Robinson, "Radiation-Induced Voids in Metals," J. W. Corbett and L. C. Ianiello, eds. National Tech. Information Service, CONF-710601, 1972.

55. C. M. Logan, J. D. Anderson and A. K. Murkherjee, J. Nucl. Mat., 48, 223, 1973.

56. D. G. Doran, Nucl. Sc. and Eng. 52, 398, 1973.

57. D. G. Doran, Nucl. Sc. and Eng. 49, 130, 1972.

58. G. L. Kulcinski, D. G. Doran, M. A. Abdou, "Comparison of Displacement and Gas Production Rates in Current Fission and Future Fusion Reactors," Proc. of Symposium of Effects of Radiation on Reactor Structural Materials, Gatlinberg, Tenn., June 1974.

59. M. T. Robinson, in "Radiation-Induced Voids in Metals," J. W. Corbett and L. C. Ianiello, eds., Nat. Tech. Inf. Series, CONF-710601, 1972.

60. C. F. Williamson, J. P. Boyot, J. Pacard, "Tables of Range and Stopping Power of Chemical Elements for Charged Particles of Energy 0.5 to 500 MeV," French Atomic Energy Commission Report CEA-R3042, July 1966.

61. J. P. Holman, Heat Transfer, McGraw-Hill Book Co., p. 170, 1963.

62. R. Hilpert, Forsch Gebicte Ingenieurw, 4, 222, 1933.

63. L. Hopf, Handbuch der Physik, 7, Chap. 2, 1927.

64. A. P. Colburn, Trans. Am. Inst. Chem. Eng., 29, 174, 1933

65. M. Jacob and G. A. Hawkins, "Elements of Heat Transfer," (John Wiley and Sons, Inc., NY) p. 270, 1957.

66. L. M. K. Boelter, V. H. Cherry, H. A. Johnson and R. C. Martinelli, "Heat Transfer Notes," McGraw-Hill Book Co., NY, Ed. VI, 1965.

67. J. C. Fisher, Trans. AIME, 194, p. 531, 1952.

68. W. G. Johnston and J. J. Gilman, J. Appl. Phy., p. 632, 1960.

69. J. C. Grosskreutz and D. K. Benson, Surfaces and Interfaces II, J. Burke, N. Reed and V. Weiss, eds., Syracuse Univ. Press, Syracuse, NY, p. 61, 1965.

70. C. Feng and I. R. Kramer, TMS-AIME, 233, p. 1467, 1965.

71. I. R. Kramer and C. L. Haehner, Acta Met., 15, p. 199, 1967.

72. I. R. Kramer, Martin Marietta Corp. Report, MCR-67-421, June 1967.

73. I. R. Kramer and L. J. Dremer, Trans. AIME, 221, p. 780, 1961.

74. P. R. Swann, Acta Met., Vol. 14, p. 900, 1966.

75. I. R. Kramer and C. L. Haehner, Acta Met., Vol. 15, p. 678, 1967.

76. J. J. Gilman, Phil. Mag., 6, p. 159, 1961.

77. R. Roscoe, Nature, 133, p. 912, 1934.

78. A. H. Cottrell and D. F. Gibbons, Nature, 162, p. 488, 1948.

79. S. Harper and A. H. Cottrell, Proc. Phys. Soc. (London), B63, p. 331, 1950.

80. J. Takamura Mem. Fac. Eng. Kyoto Univ., 18, (3), p. 255, 1956.

81. M. R. Pickus and E. R. Parker, J. of Metals, p. 792, Sept. 1951.

82. P. A. Rehbinder, Byul. Akad. Nauk Classe Sci. Mat. Nat. Ser. Chem., p. 679, 1936.

83. P. A. Rehbinder and E. K. Wenstromm, Byul. Akad. Nauk URSS Clase Sci. Mat. Nat. Sci. Physi., p. 531, 1937.

84. A. K. Head, Phil. Mag., 44, p. 92, 1953.

85. G. H. Conners, Intern. J. Engr. Sci., 5, p. 25, 1967.

86. J. C. Grosskreutz, Surface Science, 8, p. 173, 1967.

87. N. J. Wadsworth, Proc. of Symp. on Internal Stresses and Fatigue of Metals, Elsever Publ. Co., Amsterdam, p. 382, 1959.

88. K. V. Snowden, Nature, 189, p. 53, 1961.

89. P. Shahanian and M. R. Achter, Proc. of Joint Intl. Conf. on Creep, 1963.

90. W. R. Johnson, C. R. Barrett, and W. D. Nix, Met. Trans., Vol. 3, p. 695, 1972.

91. I. R. Kramer and S. E. Podlaseck, Acta Met., 11, p. 70, 1963.

92. T. A. Roth, Matl, Sci. and Engr., 18, p. 183, 1975.

93. R. K. MacCrone, J. of Appl. Phy., Vol. 38, No. 2, p. 705, 1967.

94. L. Fleischer and B. Chalmers, Trans. AIME, 212, p. 265, 1958.

95. J. Garstone, et al., Acta Met., 4, p. 485, 1956.

96. S. S. Brenner, J. of Appl. Phys., Vol. 27, No. 12, p. 1484, 1950.

97. K Yoshida, Y. Gotoh, and M. Yamamoto, J. Phy. Soc. Japan, Vol. 24, No. 5, p. 1099, 1968.

98. K. Yoshida, T. Onozuka and M. Yamamoto, J. Phy. Soc. Japan, Vol. 30, No. 1, p. 138, 1971.

99. C. D'Antonio, J. Hirschhorn, and L. Tarshio, Trans. TMS-AIME, 227, p. 1346, 1963.

100. A. Lawley and S. Schuster, Trans. TMS-AIME, 230, p. 27, 1964.

101. A. Cracknell and N. J. Petch, <u>Acta Met.</u>, Vol. 3, p. 186, 1955.

102. I. T. Aleksanyan, L. A. Tumanova, and T. D. Shermergor, <u>The Phy. of Metals and Metallog.</u>, Vol. 34, p. 220, 1972.

103. E. S. Kadamer, I. M. Kop'eu, and L. S. Toropova, <u>Metal Sci. and Heat Treatment</u>, No. 3, p. 218, 1968.

104. K. Sumino and M. Yamamoto, <u>Acta Met.</u>, Vol. 11, p. 1223, 1963.

105. H. Suzuki, S. Ikeda, and S. Takenchi, <u>J. Phy. Soc. Japan</u>, Vol. 11, No. 4, p. 382, 1956.

106. J. Garstone, R. W. K. Honeycombe, and G. Greetham, <u>Acta Met.</u>, Vol. 4, p. 485, 1956.

107. F. A. Mohamed and T. G. Langdon, <u>Met. Trans.</u>, Vol. 5, p. 2339, 1974.

108. R. L. Coble, <u>J. Appl. Phys.</u>, Vol. 34, p. 1679.

109. F. R. N. Nabarro, <u>Report of a Conference on Strength of Solids</u>, The Phy. Soc. of London, p. 75, 1948.

110. C. Herring, <u>J. Appl. Phys.</u>, Vol. 21, p. 437, 1950.

111. B. Burton, <u>Phil. Mag.</u>, 25, 3, p. 645, 1972.

112. G. B. Gibbs, <u>Phil. Mag.</u>, 13, p. 589, 1960.

113. J. H. Gittus, <u>Phil. Mag.</u>, 30, 4, p. 751, 1974.

114. D. K. Matlock and W. D. Nix, <u>Met. Trans.</u>, Vol. 5, p. 1401, 1974.

APPENDIX: DEFORMATION MECHANISM MAPS FOR NICKEL BASED ON GRAIN SIZE AND THICKNESS

I. Constitutive Equations

1. Climb or Power Creep Law

$$\dot{\varepsilon} = 2.5 \times 10^6 \, \frac{D_v Gb}{kT} \left[\frac{\sigma}{G}\right]^{4.4} \qquad \text{BULK}$$

2. Nabarro-Herring

$$\dot{\varepsilon} = \frac{28 D_v Gb}{kT} \left[\frac{b}{d}\right]^2 \left[\frac{\sigma}{G}\right] \qquad \text{BULK}$$

$$\dot{\varepsilon} = \frac{28 D_v Gb}{-kT} \left[\frac{b}{d}\right]\left[\frac{b}{t}\right]\left[\frac{\sigma}{G}\right] \qquad t \leq d$$

3. Coble

$$\dot{\varepsilon} = \frac{66.8 D_{gb} Gb}{-\;kT} \left[\frac{b}{d}\right]^3 \left[\frac{\sigma}{G}\right] \qquad \text{BULK}$$

$$\dot{\varepsilon} = \frac{66.8 D_{gb} Gb}{kT} \left[\frac{b}{d}\right]\left[\frac{b}{t}\right]^2 \left[\frac{\sigma}{G}\right] \qquad t \leq d$$

II. Derivation of Map with Constitutive Equations for Bulk Samples

A. Boundary Values at Equal Strain Rates.

1. General Form

$$C \left[\frac{\sigma}{G}\right]^n \left[\frac{b}{d}\right]^P = D \left[\frac{\sigma}{G}\right]^{n'} \left[\frac{b}{d}\right]^{P'}$$

2. Coble – N-H

$$\frac{d}{b} = \left[\frac{A}{B}\right]^{\frac{1}{(p-p')}} \left[\frac{D_v}{D_{gb}}\right]^{\frac{1}{(p-p')}}$$

$$A = 28 \qquad p = 2 \qquad \frac{D_v}{D_{gb}} = 10^{-7}$$
$$B = 66.8 \qquad p' = 3$$

$$\frac{d}{b} = (.419)^{-1}(10^{-7})^{-1} = 2.39 \times 10^7$$

117

3. N-H and Climb

$$\frac{\sigma}{G} = \left(\frac{B}{A}\right)^{\frac{1}{(n-n')}} \left(\frac{d}{b}\right)^{\frac{(p-p')}{(n-n')}}$$

$A = 2.5 \times 10^6 \qquad p = 0 \qquad n = 4.4 \qquad \frac{d}{b} = 2.39 \times 10^5$

$B = 28 \qquad p' = 2 \qquad n' = 1$

$$\frac{\sigma}{G} = (11.2 \times 10^{-6})^{0.29} (2.39 \times 10^7)^{-.58}$$

$$\frac{\sigma}{G} = 1.93 \times 10^{-6}$$

4. Boundary Between Climb - N-H and Climb - Coble

$$\text{Slope} = \frac{(n'-n)}{(p'-p)}$$

a) Slope (C:N-H) = -1.7

b) Slope (C:C) = -1.1

B. Range of $\frac{d}{b}$ and $\frac{\sigma}{G}$ Values for Nickel Samples

III. Derivation of Map with Constitutive Equations for Thin Samples

A. Boundary Equations at Equal Strain Rates

1. General Form

$$C \left[\frac{\sigma}{G}\right]^n \left[\frac{b}{d}\right]^P \left[\frac{b}{t}\right]^Q = D \left[\frac{\sigma}{G}\right]^{n'} \left[\frac{b}{d}\right]^{P'} \left[\frac{b}{t}\right]^{Q'}$$

2. Coble-Nabarro-Herring

$$\frac{d}{b} = \left[\frac{D_v}{D_{gb}}\right]^{\frac{1}{(p-p')}} \left[\frac{t}{b}\right]^{\frac{(Q'-Q)}{(p-p')}}$$

$$\frac{t}{b} = \left[\frac{D_v}{D_{gb}}\right]^{\frac{1}{(Q-Q')}} \left[\frac{d}{b}\right]^{\frac{(p'-p)}{(Q-Q')}}$$

118

3. Nabarro-Herring and Climb

$$\frac{\sigma}{G} = \left(\frac{D}{C}\right)^{\frac{1}{(n-n')}} \left(\frac{d}{b}\right)^{\frac{(p-p')}{(n-n')}} \left(\frac{t}{b}\right)^{\frac{(Q-Q')}{(n-n')}}$$

4. Boundary Between Climb – N-H and Climb-Coble

a) $\frac{t}{b}$ = constant

$$\text{SLOPE} = \frac{n'-n}{p'-p}$$

b) $\frac{d}{b}$ = constant

$$\text{SLOPE} = \frac{n'-n}{Q'-Q}$$

B. Boundary Values

1. Coble-Nabarro Herring

$$\frac{D_v}{D_{gb}} = 10^{-7} \qquad \begin{array}{ll} p = 1 & Q = 1 \\ p' = 1 & Q' = 2 \end{array}$$

a) Constant $\frac{t}{b} \simeq 2.5 \times 10^5$

solution breaks down $\frac{d}{b} \to \infty$

b) Constant $\frac{d}{b}$

$$\frac{t}{b} \bullet 10^7$$

2. N-H: Climb

$$\frac{D}{C} = \frac{28}{2.5 \times 10^6} \qquad \begin{array}{lll} p = 0 & Q = 0 & n = 4.4 \\ p' = 1 & Q' = 1 & n' = 1 \end{array}$$

$$\frac{d}{b} = \frac{1}{2}\frac{t}{b} = 5 \times 10^6$$

$$\frac{\sigma}{G} = 3.9 \times 10^{-6}$$

119

3. Slopes of Boundaries

   a) Slope (Climb -N-H) = $\dfrac{1-4.4}{1}$ = -3.4

   b) Slope (Climb-Coble)= $\dfrac{1-4.4}{2}$ = -1.7

DISTRIBUTION

No. of
Copies

OFFSITE

2   ERDA Chicago Patent Group

         A. A. Churm

200   ERDA Technical Information Center

1   University of Wisconsin
      Nuclear Engineering Department
      Engineering Research Building
      Madison, Wisconsin 53706

         G. Kulcinski

1   Massachusetts Institute of Technology
      Cambridge, Massachusetts 02139

         A. Bement

2   Lawrence Livermore Laboratories
      Post Office Box 808
      Livermore, Calif. 94550

         R. Vandervoort
     J. J. Mitchell
         R. Scanlon

2   Division of Controlled Thermonuclear Research
      Materials and Radiation Effects Branch
      ERDA Headquarters
      Germantown, Maryland 20767

         K. Zwilsky
         T. Reuther

1   Oak Ridge National Laboratory
      Post Office Box X
      Oak Ridge, Tennessee 37830

         T. Reiley

ONSITE - HANFORD

1   ERDA Richland Operations Office

         B. J. Melton

1   ERDA Richland Patent Attorney

         R. M. Poteat

DISTRIBUTION

3   <u>Hanford Engineering Development Laboratory</u>

        J. Straalsund
        GL Wire
        D. Doran

47   <u>Battelle-Northwest</u>

        L. C. Schmid
        A. J. Haverfield
        D. L. Styris (20)
        O. K. Harling
        R. H. Jones (10)
        R. P. Marshall (10)
        Technical Information (3)
        Technical Publications

261